

Immune evasion through mitochondrial transfer in the tumour microenvironment

<https://doi.org/10.1038/s41586-024-08439-0>

Received: 5 January 2023

Accepted: 21 November 2024

Published online: 22 January 2025

Open access

 Check for updates

Hideki Ikeda^{1,2}, Katsuhige Kawase^{1,3}, Tatsuya Nishi^{4,5}, Tomofumi Watanabe^{4,6}, Keizo Takenaga⁷, Takashi Inozume^{1,8,9}, Takamasa Ishino^{1,4,10}, Sho Aki^{11,12}, Jason Lin¹, Shusuke Kawashima^{1,8}, Joji Nagasaki^{1,4}, Youki Ueda⁴, Shinichiro Suzuki¹³, Hideki Makinoshima¹⁴, Makiko Itami¹⁵, Yuki Nakamura¹, Yasutoshi Tatsumi^{1,16}, Yusuke Suenaga¹⁷, Takaaki Morinaga¹, Akiko Honobe-Tabuchi⁹, Takehiro Ohnuma^{9,18}, Tatsuyoshi Kawamura⁹, Yoshiyasu Umeda¹⁹, Yasuhiro Nakamura¹⁹, Yukiko Kinbara²⁰, Eiki Ichihara⁵, Hidetoshi Hayashi¹³, Jun-ichiro Ikeda²¹, Toyoyuki Hanazawa³, Shinichi Toyooka²², Hiroyuki Mano²³, Takuji Suzuki^{2,24}, Tsuyoshi Osawa^{11,12,25}, Masahito Kawazu^{1,23} & Yosuke Togashi^{1,4,5,26} 

Cancer cells in the tumour microenvironment use various mechanisms to evade the immune system, particularly T cell attack¹. For example, metabolic reprogramming in the tumour microenvironment and mitochondrial dysfunction in tumour-infiltrating lymphocytes (TILs) impair antitumour immune responses^{2–4}. However, detailed mechanisms of such processes remain unclear. Here we analyse clinical specimens and identify mitochondrial DNA (mtDNA) mutations in TILs that are shared with cancer cells. Moreover, mitochondria with mtDNA mutations from cancer cells are able to transfer to TILs. Typically, mitochondria in TILs readily undergo mitophagy through reactive oxygen species. However, mitochondria transferred from cancer cells do not undergo mitophagy, which we find is due to mitophagy-inhibitory molecules. These molecules attach to mitochondria and together are transferred to TILs, which results in homoplasmic replacement. T cells that acquire mtDNA mutations from cancer cells exhibit metabolic abnormalities and senescence, with defects in effector functions and memory formation. This in turn leads to impaired antitumour immunity both *in vitro* and *in vivo*. Accordingly, the presence of an mtDNA mutation in tumour tissue is a poor prognostic factor for immune checkpoint inhibitors in patients with melanoma or non-small-cell lung cancer. These findings reveal a previously unknown mechanism of cancer immune evasion through mitochondrial transfer and can contribute to the development of future cancer immunotherapies.

Cancer cells evade immune surveillance through various mechanisms, including the production of immunosuppressive molecules and cells that create a favourable tumour microenvironment (TME) for progression¹. Inhibitory immune-checkpoint molecules, such as cytotoxic T lymphocyte antigen-4 (CTLA-4), programmed cell death protein 1 (PD-1) and PD-1 ligand 1 and PD-1 ligand 2 (PD-L1/2), are crucial in this process. Consequently, immune-checkpoint inhibitors (ICIs), including anti-PD-1, anti-PD-L1 and anti-CTLA-4 monoclonal antibodies, have improved

patient survival in various cancer types^{5–7}. However, many patients fail to respond to treatment or achieve durable responses despite an initial response^{8,9}. Thus, identification of the various immune-evasion mechanisms that cancer cells use is essential to improve ICI efficacy.

Metabolic reprogramming in the TME is crucial for antitumour immune responses². However, the hypoxic and low-glucose environment in tumours promotes glycolysis over oxidative phosphorylation (OXPHOS). This shift affects T cell effector functions, exhaustion,

¹Division of Cell Therapy, Chiba Cancer Center Research Institute, Chiba, Japan. ²Department of Respiratory, Graduate School of Medicine, Chiba University, Chiba, Japan. ³Department of Otorhinolaryngology/Head and Neck Surgery, Chiba University Graduate School of Medicine, Chiba, Japan. ⁴Department of Tumor Microenvironment, Faculty of Medicine, Dentistry and Pharmaceutical Sciences, Okayama University, Okayama, Japan. ⁵Department of Allergy and Respiratory Medicine, Okayama University Hospital, Okayama, Japan. ⁶Department of Urology, Okayama University Graduate School of Medicine, Dentistry and Pharmaceutical Sciences, Okayama, Japan. ⁷Division of Innovative Cancer Therapeutics, Chiba Cancer Center Research Institute, Chiba, Japan. ⁸Department of Dermatology, Graduate School of Medicine, Chiba University, Chiba, Japan. ⁹Department of Dermatology, Faculty of Medicine, University of Yamanashi, Yamanashi, Japan. ¹⁰Department of Gastroenterology, Graduate School of Medicine, Chiba University, Chiba, Japan. ¹¹Division of Nutriomics and Oncology, RCAST, The University of Tokyo, Tokyo, Japan.

¹²Department of Chemistry and Biotechnology, Graduate School of Engineering, The University of Tokyo, Tokyo, Japan. ¹³Department of Medical Oncology, Kindai University Faculty of Medicine, Osaka, Japan. ¹⁴Tsuruoka Metabolomics Laboratory, National Cancer Center, Yamagata, Japan. ¹⁵Department of Surgical Pathology, Chiba Cancer Center, Chiba, Japan. ¹⁶Laboratory of Pediatric and Refractory Cancer, Chiba Cancer Center Research Institute, Chiba, Japan. ¹⁷Laboratory of Evolutionary Oncology, Chiba Cancer Center Research Institute, Chiba, Japan. ¹⁸Department of Dermatology and Plastic Surgery, Faculty of Life Sciences, Kumamoto University, Kumamoto, Japan. ¹⁹Department of Skin Oncology/Dermatology, Saitama Medical University International Medical Center, Saitama, Japan. ²⁰Department of Dermatology, Shinshu University School of Medicine, Nagano, Japan. ²¹Department of Diagnostic Pathology, Graduate School of Medicine, Chiba University, Chiba, Japan. ²²Department of General Thoracic Surgery and Endocrinological Surgery, Faculty of Medicine, Dentistry and Pharmaceutical Sciences, Okayama University, Okayama, Japan. ²³Division of Cellular Signalling, National Cancer Center Research Institute, Tokyo, Japan. ²⁴Synergy Institute for Futuristic Mucosal Vaccine Research and Development, Chiba University, Chiba, Japan.

²⁵Department of Biological Sciences, Graduate School of Science, The University of Tokyo, Tokyo, Japan. ²⁶Faculty of Medicine, Kindai University, Osaka, Japan.  e-mail: ytogashi1584@gmail.com

senescence and memory formation to benefit cancer cell survival². Mitochondria have significant roles in the metabolic reprogramming of both epithelial and immune cells, including T cells¹⁰. Mitochondrial dysfunction in TILs leads to metabolic insufficiency followed by a terminally differentiated exhaustion state in T cells^{3,4}. However, most studies have focused on mouse models, with little research on human TILs¹¹. Moreover, the mechanisms that underlie mitochondrial dysfunction in TILs remain unclear.

mtDNA encodes important proteins for energy generation and is vulnerable to mutations owing to poor repair mechanisms^{12,13}. Many mutations in mtDNA lead to impairment in OXPHOS and promote tumour growth and metastasis in various cancers^{14–18}. However, few studies have explored their impact on antitumour immunity¹⁹.

Mitochondrial transfer occurs across different cells and alters mitochondrial metabolism in recipient cells^{20,21}. In vivo, cancer cells with impaired OXPHOS owing to a lack of mtDNA acquire mitochondrial genomes from the host to restore mitochondrial respiration^{22,23}. A previous study²⁴ has shown that cancer cells obtain mitochondria through tunnelling nanotubes (TNTs) from T cells to hinder antitumour responses. Moreover, extracellular vesicles (EVs) can transport mitochondria across different cells through EV–cell fusion events^{25–27}. Although mitochondrial transfer can occur from cancer cells to T cells in the TME, the incidence and effects of this process on antitumour immunity remain unclear.

Here we analyse clinical samples of various cancer types and show that mtDNA mutations are present in TILs. Many of these mtDNA mutations are shared with the cancer cells and are obtained through mitochondrial transfer. We also investigate the functions of mtDNA-mutated T cells, including antitumour immunity mediated by PD-1 blockade. The clinical significance of these results in patients with melanoma or non-small-cell lung cancer (NSCLC) receiving ICIs is also evaluated. This study reveals a previously undescribed immune-evasion mechanism that involves mitochondrial transfer.

mtDNA mutations in TILs and cancer cells

To understand the mechanisms of mitochondrial dysfunction in TILs, we first sequenced mtDNA from TILs obtained from 12 patients with various types of cancer (cohort A; see Methods for details of patient samples and the cell lines established used for this study). The analysis showed that 5 out of the 12 patients had mtDNA mutations in their TILs (Fig. 1a, Extended Data Fig. 1a–c and Supplementary Tables 1 and 2). We confirmed that bulk TILs were predominantly composed of CD45⁺CD3⁺ T cells and that sorted T cells had the same mutations (Fig. 1b,c and Extended Data Fig. 1a). We established matched cancer cell lines from seven patients, of whom four had mtDNA-mutated TILs. Notably, three out of the four TILs shared the same mutations as the cancer cells (Fig. 1a,c and Extended Data Fig. 1b,c). We established a single T cell clone with wild-type mtDNA (TIL04#9) from bulk TIL04 cells with mutated mtDNA (3290T>C) (Extended Data Fig. 1d). Electron microscopy imaging revealed abnormal mitochondrial morphology and reduced cristae in TILs (bulk TIL04 and TILc03) and cancer cells (MELO4 and MELc03) with mtDNA mutations. By contrast, mitochondria in TILs (TIL02 and TIL04#9) and cancer cells (MELO2) with wild-type mtDNA seemed to be morphologically normal. Notably, normal morphology was predominantly observed in matched peripheral blood lymphocyte (PBL) samples (PBL02, PBL04 and PBLc03) (Fig. 1d and Extended Data Fig. 1e). To confirm that the mtDNA mutations did not occur during the culture process, we analysed formalin-fixed paraffin-embedded (FFPE) tumour tissue from patient 04. The results showed that this tissue sample had the same mutation (Fig. 1e).

Mitochondrial transfer from cancer cells

Mitochondrial transfer can occur among different cells^{20–27}; therefore, we speculated that the shared mtDNA mutations observed between

cancer cells and T cells might result from mitochondrial transfer. To avoid false positives and to accurately evaluate the transfer process, we introduced MitoDsRed, a mitochondria-specific fluorescent protein^{28,29}, into MELO2 cells (wild-type mtDNA) and MELO4 cells (mutated mtDNA) (MELO2-MitoDsRed and MELO4-MitoDsRed, respectively; Supplementary Fig. 2). When TILs were cocultured with these MitoDsRed-overexpressing cancer cells, mitochondrial transfer from cancer cells, as evaluated by DsRed expression, rarely occurred within 24 h, results consistent with those from another study²² (Extended Data Fig. 1f). However, after 24 h, mitochondrial transfer from cancer cells to T cells occurred²⁴ (Fig. 2a,b and Extended Data Fig. 1f). The mtDNA status did not affect transfer efficiency (wild-type MELO2 to TIL02 versus mutated MELO4 to TIL04#9) (Extended Data Fig. 1f). The formation of TNTs and the release of EVs can promote mitochondrial transfer^{21,24–27}; therefore, we evaluated mitochondrial transfer under various conditions (Fig. 2c and Extended Data Fig. 1g). Transfer in TILs was substantially reduced with the following treatments: cytochalasin B, a TNT inhibitor; cell-culture column inserts (3 μm and 0.4 μm), to avoid direct cell–cell contact; and/or GW4869, a compound that blocks the release of small EVs (about 200 nm)³⁰ (Fig. 2c and Extended Data Fig. 1g). Although larger EVs and naked mitochondria could pass through the 3 μm column and not the 0.4 μm column, both conditions reduced mitochondrial transfer levels to the same degree (Fig. 2c and Extended Data Fig. 1g,h). In addition, cytochalasin B reduced transfer to the same degree as the columns, but adding cytochalasin B to the insert columns did not further reduce transfer levels (Fig. 2c and Extended Data Fig. 1g,h). These results indicate that the inhibitory effect of the columns probably originates primarily from the inhibition of direct cell–cell contact through TNT formation rather than indirectly through larger EVs or naked mitochondria. Accordingly, an inhibitor of larger EVs (microEVs; >200 nm), Y-27632, reduced mitochondrial transfer but to a lesser extent than GW4869. This result indicates that microEVs are less important than small EVs, as previously reported^{25,30–32} (Fig. 2c and Extended Data Fig. 1g). Small EVs could pass through both sizes of the columns, and adding GW4869 to the insert column substantially reduced transfer levels, which indicated that both direct cell–cell contact through TNT formation and indirect cell–cell interactions through small EVs may have important roles in mitochondrial transfer (Fig. 2c and Extended Data Fig. 1g). Thus, we isolated, purified and analysed EVs smaller than 200 nm. The purified EVs contained a mitochondrial protein, cytochrome c, in addition to CD9 and TSG101, small EV proteins (Extended Data Fig. 1i), indicating that small EVs actually contain mitochondria. Taken together, these results show that tumour-infiltrating T cells acquire mtDNA mutations from cancer cells through direct and indirect mitochondrial transfer. The formation of TNTs enables direct cell–cell contact, whereas EVs enable indirect cell–cell interactions.

Mitochondrial replacement to homoplasmy

Next, we investigated whether homoplasmy occurred after mitochondrial transfer. We sorted single CD45⁺CD3⁺ T cells from TIL04#9 cells after coculture with MELO4 cells and sequenced the obtained mtDNA in each single T cell at various time points. Replacement of mitochondria to homoplasmy occurred in a subset of T cells after 15 days of coculture (Fig. 2d). We also conducted time-lapse imaging studies using TIL04#9 cells labelled with MitoTracker Green and cocultured with MELO4-MitoDsRed cells. In several TILs, MitoTracker Green levels in TILs gradually decreased, whereas DsRed signals, derived from cancer cells, gradually increased in TILs after coculture. Eventually, the MitoTracker Green signal was replaced by DsRed in the TILs, which indicated the occurrence of mitochondria replacement to homoplasmy, and this effect was subsequently maintained (Fig. 2e,f). To confirm mitochondrial transfer in vivo, we used LLC/A11 cells with an mtDNA 13997G>A mutation in *Nd6* (this cell line was established

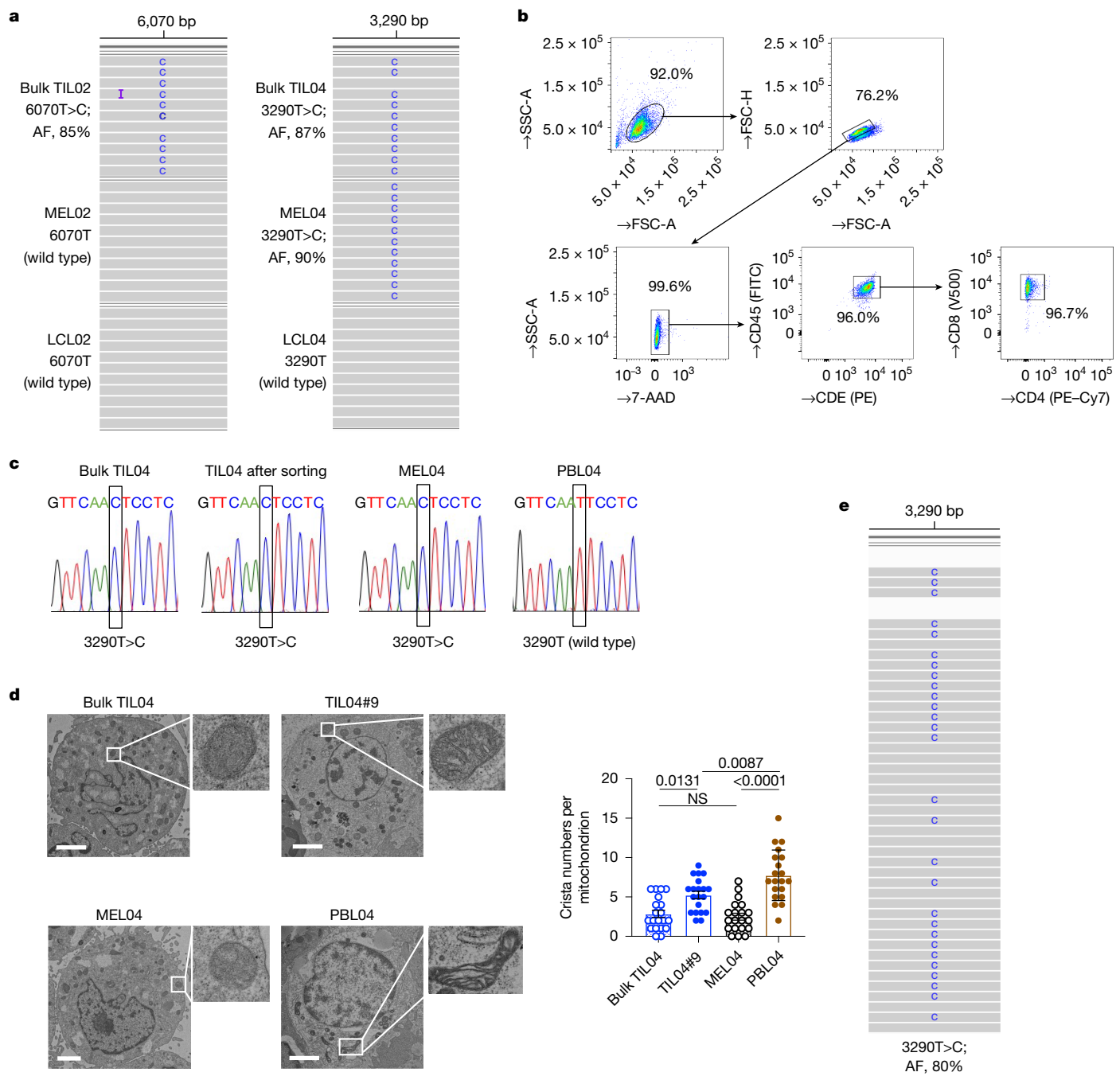


Fig. 1 | TILs and cancer cells share mtDNA-mutated mitochondria. **a**, Integrative Genomics Viewer (IGV) track data of the entire mtDNA from paired TILs and cancer cells from the same patient (02 and 04). A lymphoblastoid cell line (LCL) established from PBLs from the same patient (through Epstein–Barr virus transformation) was used as germline controls. **b**, Representative gating strategy for bulk TIL analyses. **c**, Capillary sequencing chromatograms of mtDNA from patient 04. mtDNA from sorted pure CD45⁺CD3⁺T cells from bulk TIL04 cells, MEL04 cells and PBL04 cells were sequenced. **d**, Left, representative

transmission electronic microscopy images of bulk TIL04, TIL04#9, MEL04 and PBL04 cells from patient 04. Right, the number of cristae per mitochondrion ($n=20$ per mitochondrion) were counted and quantified. Scale bars, 2 μ m. **e**, IGV track data of the entire mtDNA of FFPE tumour tissue from patient 04. For **a** and **e**, next-generation sequencing was used for analyses. P values (shown on the chart) were calculated using one-way analysis of variance (ANOVA) with Bonferroni correction (**d**). Error bars show s.e.m. AF, allele frequency; NS, not significant.

from mouse Lewis lung carcinoma)¹⁷ (Supplementary Fig. 2). As for the in vitro experiments, MitoDsRed was also introduced into these cells (LLC/A11-MitoDsRed) (Supplementary Fig. 2). After inoculating these cancer cells into C57BL/6J mice, we collected the tumours and analysed TILs on days 21 and 42 (Supplementary Fig. 3). We observed a gradual increase in the frequency of DsRed⁺ T cells in TILs, which indicated the occurrence of mitochondrial transfer from LLC/A11 cells (Fig. 2g,h). We sorted DsRed⁺ T cells from TILs at the single-cell level

on the basis of DsRed staining and sequenced the mtDNA. The results showed that the mtDNA mutation was present at the single-cell level in DsRed⁺ T cells, some of which were homoplasmic (Fig. 2i). By contrast, all DsRed⁻ T cells had wild-type mtDNA (Fig. 2i). Using this model, we sorted mitochondria-transferred DsRed⁺ T cells from TILs and cultured these in vitro. DsRed expression gradually decreased over 7 days, and the mtDNA-mutated allele in heteroplasmy was also decreased in bulk TILs (Extended Data Fig. 2a,b).

Article

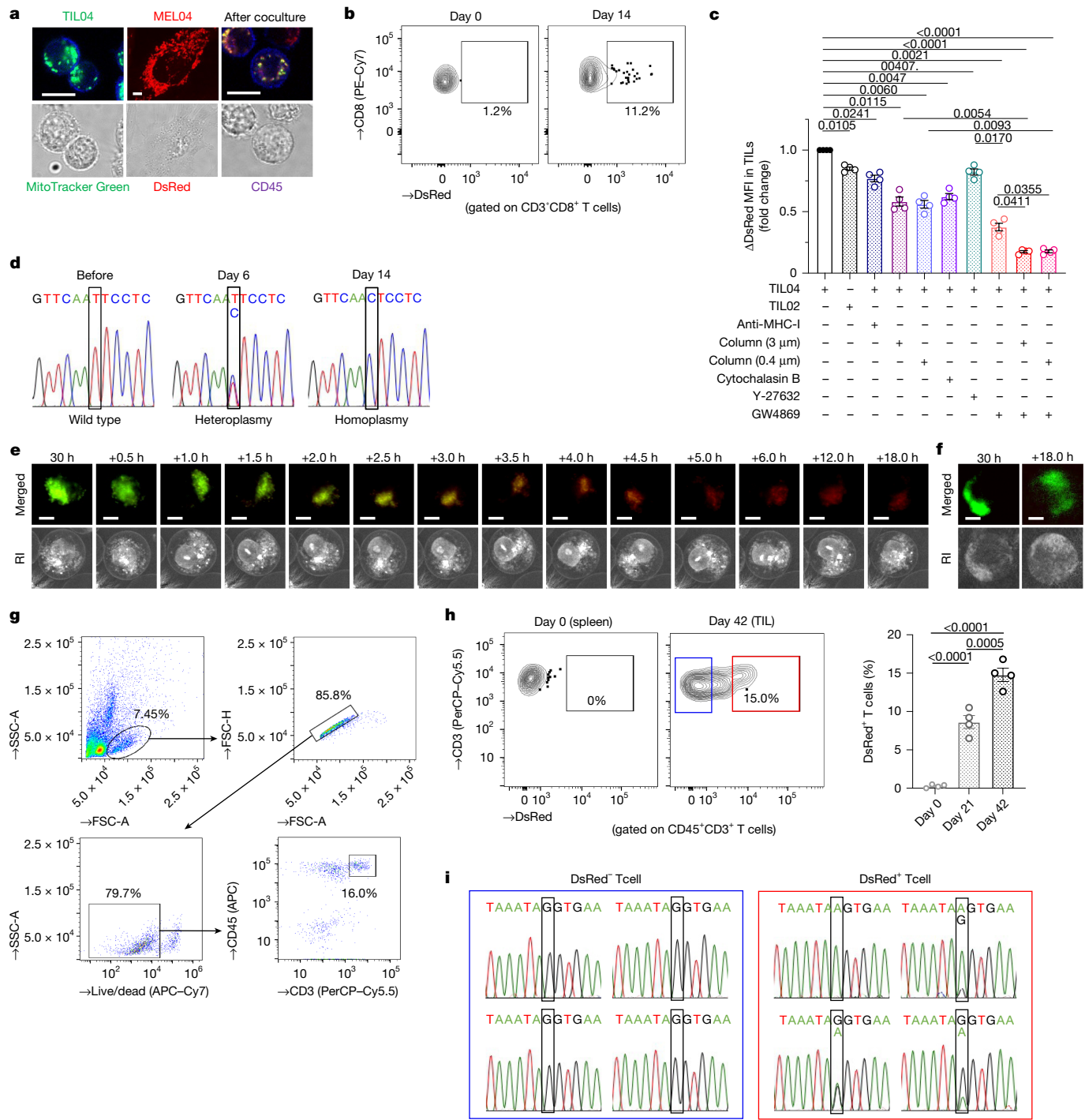


Fig. 2 | mtDNA-mutated mitochondria from cancer cells transfer to TILs and are progressively replaced to homoplasmy in TILs. **a**, Representative confocal microscopy images of mitochondrial transfer from three independent experiments. TILO4#9 cells labelled with MitoTracker Green were cocultured with MELO4-MitoDsRed cells for 2 days. Scale bars, 10 μm. **b**, Representative flow cytometry staining analysis of mitochondrial transfer from four independent experiments. TILO4#9 cells were cocultured with MELO4-MitoDsRed cells for 14 days and were subsequently analysed. **c**, Quantification of mitochondria from TILs transferred from MELO4 cells. TILs were cocultured with MELO4-MitoDsRed cells for 2 days with or without an anti-major histocompatibility class I (MHC-I) monoclonal antibody, a TNT inhibitor (cytochalasin B), insertion columns (3 or 0.4 μm), a small EV release inhibitor (GW4869) and/or a microEV inhibitor (Y-27632), and were subsequently analysed by flow cytometry. Summary of fold changes of ΔDsRed mean fluorescence intensity (MFI) (DsRed MFI of TILs with coculture – that without coculture) relative to the controls is shown ($n = 4$ per group). **d**, Capillary sequencing chromatograms of mtDNA in TILO4#9

cells cocultured with MELO4 cells. After single-cell sorting, mtDNA was sequenced. **e,f**, Time-lapse imaging. TILO4#9 cells labelled with MitoTracker Green were cocultured with MELO4-MitoDsRed cells. We captured images every 30 min using a digital holographic microscope. Representative merged fluorescence (top) and three-dimensional refractive index (RI) images (bottom) in TILs are shown from three independent experiments. Scale bars, 4 μm. **g**, Representative gating strategy for mouse TIL analyses. The tumours were digested, stained with CD45 and CD3 and were analysed. **h,i**, Frequency of DsRed⁺ T cells (**h**, left) and mtDNA sequencing in TILs (**i**) from LLC/A11-MitoDsRed tumours. In vivo experiments were performed as described in Supplementary Fig. 3. Representative flow cytometry staining (**h**, left), quantification (**h**, right, $n = 4$ per group) and capillary sequencing chromatograms for DsRed⁻ cells (**i**, left) and DsRed⁺ T cells (**i**, right) are shown. P values (shown on charts) were calculated using one-way ANOVA with Bonferroni corrections (**c,h**). Error bars show s.e.m.

We next investigated the mechanisms of homoplasmic replacement. Mitochondrial transfer from MitoDsRed-overexpressing cancer cells to T cells, assessed according to DsRed expression, gradually increased after coculture (Extended Data Fig. 1f). By contrast, the transfer of *in situ* mitochondria in T cells, stained by MitoTracker Green, decreased after coculture (Fig. 3a). To avoid false positives and to accurately evaluate mitochondrial transfer from T cells to cancer cells, we used PhaM^{excised} OT-1 mice, which express a mitochondrial-specific fluorescent protein (mito-Dendra2) with an ovalbumin (OVA)-specific T cell receptor, and OVA-overexpressing LLC/A11 cells (Supplementary Fig. 2). We confirmed the occurrence of mitochondrial transfer from T cells to cancer cells, evaluated using Dendra2 (green), as previously reported²² (Extended Data Fig. 2c). Conversely, the numbers of *in situ* mitochondria in cancer cells, evaluated using MitoTracker Green, were not reduced by coculture both in mouse and human cancer cells, a result that was in contrast to that for *in situ* mitochondria in T cells (Extended Data Fig. 2d,e). Cancer-producing reactive oxygen species (ROS) in the TME cause mitophagy in surrounding cells³³. As previously reported³⁴, ROS were detected in EVs from cancer cells when we analysed EVs by flow cytometry (Extended Data Fig. 2f). The ROS were scavenged by N-acetyl-L-cysteine (NAC) treatment under coculture conditions. NAC treatment prevented the reduction in *in situ* mitochondrial numbers in T cells, stained by MitoTracker Green, and mitochondrial replacement to homoplasmy did not occur after coculture with NAC (Fig. 3b,c). By contrast, NAC treatment did not affect mitochondrial transfer from MitoDsRed-overexpressing cancer cells to T cells (Extended Data Fig. 2g). Staining with LC3B showed that the mitophagy level in T cells was enhanced by coculture with MELO4-MitoDsRed cells but decreased by NAC treatment (Fig. 3d,e). We analysed gene expression in TILs with mutated mtDNA obtained through mitochondrial transfer (TILs were sorted from DsRed⁺TIL04#9 cells after coculture with MELO4-MitoDsRed cells). The expression levels of mitophagy-related and mitochondrial-stress-response genes (*BNIP3* and *ATF4*) were higher in the DsRed⁺ TILs than in TIL04#9 cells or DsRed⁺TIL04#9 cells (Fig. 3f). The mitophagy inhibitor baflomycin A1 prevented the reduction in *in situ* mitochondrial numbers in T cells (Fig. 3g). These findings suggest that *in situ* mitochondria in T cells are sensitive to mitophagy induced by ROS, whereas mitochondria from cancer cells are resistant. This difference in mitophagy could induce homoplasmic replacement following transfer.

We investigated in detail the mechanisms that underlie this difference in sensitivity to mitophagy. Our results showed that mitochondria transferred from cancer cells to T cells are resistant to mitophagy. Therefore, we speculated that specific cancer cell factors that are transferred together with the mitochondria may confer this resistance in T cells. To that end, we searched for mitophagy-inhibitory molecules that attach to mitochondria. Parkin-mediated ubiquitination is crucial for mitophagy, and the deubiquitinating enzymes USP30, USP33 and USP35 can inhibit parkin-mediated mitophagy and attach to mitochondria^{35–39}. According to data from The Cancer Genome Atlas, *USP30* is expressed at high levels in melanoma, and *USP30* can inhibit mitophagy^{36,37} (Extended Data Fig. 2h). Therefore, we focused on *USP30*. As expected, *USP30* expression was high in cancer cells and slightly increased in TILs with mutated mtDNA, but low in TILs and PBLs with wild-type mtDNA (Extended Data Fig. 2i). After coculture with cancer cells, *USP30* was transferred together with mitochondria from cancer cells to TILs (Fig. 3h,i). This result was confirmed through *USP30* staining experiments, which showed *USP30* colocalization with transferred mitochondria from cancer cells (Fig. 3h). A *USP30* inhibitor, CMPD-39, partially decreased mitochondrial transfer from MitoDsRed-overexpressing cancer cells to TILs, which in turn partially prevented progressive replacement to homoplasmy (Fig. 3j,k). Given the potential off-target effects of CMPD-39, we used two short interfering RNAs (siRNAs) that target *USP30* (si*USP30*-1 and si*USP30*-2) to confirm the role of this factor. Similar results were obtained with these

siRNAs as for CMPD-39 (Fig. 3j,k and Supplementary Fig. 2). Therefore, mitophagy-inhibitory molecules, such as *USP30*, confer resistance to mitophagy in mitochondria transferred from cancer cells, which may be partially related to homoplasmic replacement. That is, mitochondria transferred from cancer cells along with mitophagy-inhibitory molecules do not undergo mitophagy, whereas *in situ* mitochondria in T cells undergo mitophagy owing to cancer-derived ROS, which results in the replacement of mitochondria.

Mitochondrial dysfunction in mutated T cells

We next evaluated mitochondrial-related molecules, including ND4, ND5, ND6, ND1, CYTB, COX1 and ATP6. mtDNA-mutated MELO4 cells with a mutation in the tRNA region (3290T>C) had lower expression of these molecules than other wild-type MELO2 or MCF7 cells (Extended Data Fig. 3a and Supplementary Fig. 2). This reduction in expression was reversed by taurine treatment, as previously reported^{40,41} (Extended Data Fig. 3b). mtDNA-mutated MDA-MB-231 cells with a mutation in *ND4* (12084C>T) or *ND5* (13966A>G) also had low expression of *ND4* and *ND5*, respectively⁴² (Extended Data Fig. 3a and Supplementary Fig. 2). Consistently, we observed reduced basal respiration and increased dependency on glycolysis in mtDNA-mutated MELO4 cells and MDA-MB-231 cells, as assessed using a flux analyser (Extended Data Fig. 3d,e). Moreover, total ATP and ATP produced by OXPHOS were reduced in these mtDNA-mutated cells. Furthermore, the activities of complexes I, II and III, and IV in MELO4 cells and that of complex I in MDA-MB-231 cells were reduced (Extended Data Fig. 3f–i). These results indicate that these mutated mitochondria have impaired function.

The functions of TILs with wild-type mitochondria and TILs with mtDNA-mutated mitochondria transferred after coculture with melanoma cells, MELO2-MitoDsRed cells (wild type) or MELO4-MitoDsRed (mutated) cells were analysed on the basis of DsRed expression (DsRed⁺TIL04#9/02, wild type; DsRed⁺TIL04#9/02, wild type; DsRed⁺TIL04#9/04, wild type; and DsRed⁺TIL04#9/04 cells, mutated, respectively) (Fig. 4a and Supplementary Figs. 2 and 4). As our established TILs mainly consisted of CD8⁺ T cells, we primarily evaluated CD8⁺ T cell functions (Fig. 1b). The mtDNA-mutated TILs (DsRed⁺TIL04#9/04 cells) had significantly reduced membrane potentials (Fig. 4b). Although ROS can be produced in many cellular compartments, the majority of cellular ROS are produced in mitochondria during ATP generation through OXPHOS⁴³. mtDNA damage depletes the amount of proteins that form the mitochondrial respiratory complex. This creates a positive-feedback loop that generates ROS through changes in the reduction state of the electron transport chain owing to inhibition of complex IV or V and excessive succinate production^{44–46}. Indeed, DsRed⁺TIL04#9/04 cells, which have mutated mtDNA, exhibited a substantial increase in ROS production (Fig. 4c). Previous studies showing that mitochondria and ROS have crucial roles in cellular senescence^{47,48} prompted us to evaluate T cell senescence and memory formation. The presence of mutated mtDNA increased β-galactosidase activity and the levels of the senescence molecules p16 and p53 (Fig. 4d–f). The CD27[−]CD28[−] senescent fraction and the senescence-associated secretory phenotype, such as *IL6*, *CXCL8* and *IL1B*, of DsRed⁺TIL04#9/04 cells were also increased (Fig. 4g–j). Consistently, DsRed⁺TIL04#9/04 cells had a reduced division potential and were more apoptotic (Fig. 4k,l). The CCR7^{high}CD45RA^{low} central memory cell fraction and the long-lived KLRG1^{low} cell fraction were significantly reduced in DsRed⁺TIL04#9/04 cells (Fig. 4m,n). As the CCR7^{high}CD45RA^{high} naive fraction was small in TILs, we further evaluated memory formation using PBLs. When sorted CCR7^{high}CD45RA^{high} naive CD8⁺ T cells from PBLs were differentiated in the presence of MELO2-MitoDsRed cells or MELO4-MitoDsRed cells, the CCR7^{high}CD45RA^{low} central memory and long-lived KLRG1^{low} cell fractions were also significantly reduced in mtDNA-mutated DsRed⁺CD8⁺ T cells (Extended Data Fig. 3j,k). Furthermore, when each CD8⁺ T cell fraction sorted from PBLs was

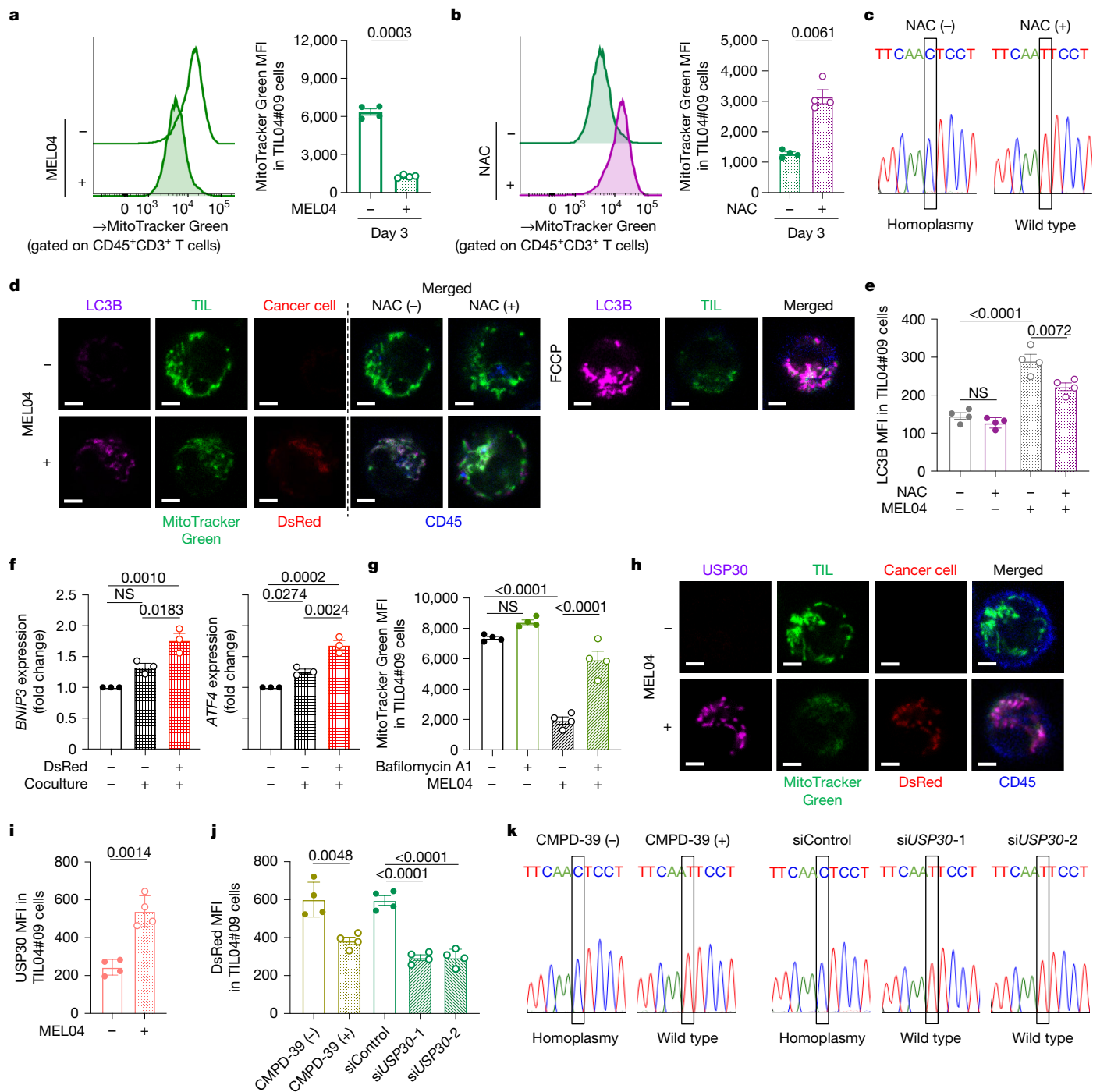


Fig. 3 | Mitochondria from cancer cells are resistant to mitophagy because of USP30. **a,b**, Quantification of mitochondria in TILs. TIL04#9 cells labelled with MitoTracker Green were cocultured with MEL04 cells for 3 days (**a**, without NAC; **b**, with NAC) and were subsequently analysed. Representative flow cytometry staining (left) and quantification (right) are shown ($n = 4$ per group). **c**, Capillary sequencing chromatograms of mtDNA in TIL04#9 cells cocultured with MEL04 cells with or without NAC at day 14. After single-cell sorting, mtDNA was sequenced. **d,e**, LC3B staining. TIL04#9 cells labelled with MitoTracker Green were cocultured with MEL04-MitoDsRed cells for 3 days and were subsequently stained and analysed. Representative confocal microscopy images (**d**) and quantification (**e**) are shown ($n = 4$ per group). Scale bars, 2 μ m. FCCP, carbonyl cyanide 4-(trifluoromethoxy)phenylhydrazone. **f**, BNP3 and ATF4 expression. TIL04#9 cells were cocultured with MEL04-MitoDsRed cells for 14 days and sorted TILs were analysed by real-time PCR. Quantification of fold change values to the controls are shown ($n = 3$ per group). **g**, Quantification of mitochondria in

TIL04#9 cells treated with a mitophagy inhibitor. Coculture was performed as described in **a** with or without bafilomycin A1 and TILs were subsequently analysed. Quantification is shown ($n = 4$ per group). **h,i**, USP30 staining. TIL04#9 cells labelled with MitoTracker Green were cocultured with MEL04-MitoDsRed cells for 3 days and were subsequently stained and analysed. Representative confocal microscopy images (**h**) and quantification (**i**) are shown ($n = 4$ per group). Scale bars, 2 μ m. **j**, Quantification of mitochondrial transfer in TILs treated with a USP30 inhibitor or siRNAs. TIL04#9 cells were cocultured with MEL04-MitoDsRed cells for 3 days with or without CMPD-39 or siRNAs and were subsequently analysed. Quantification is shown ($n = 4$ per group). **k**, Capillary sequencing chromatograms of mtDNA in TIL04#9 cells cocultured with MEL04 cells with or without CMPD-39 or siRNAs at day 14. After single-cell sorting, mtDNA was sequenced. *P*values (shown on charts) were calculated using two-sided t-tests (**a,b,i**) or one-way ANOVA with Bonferroni corrections (**e-g,j**). Error bars show s.e.m.

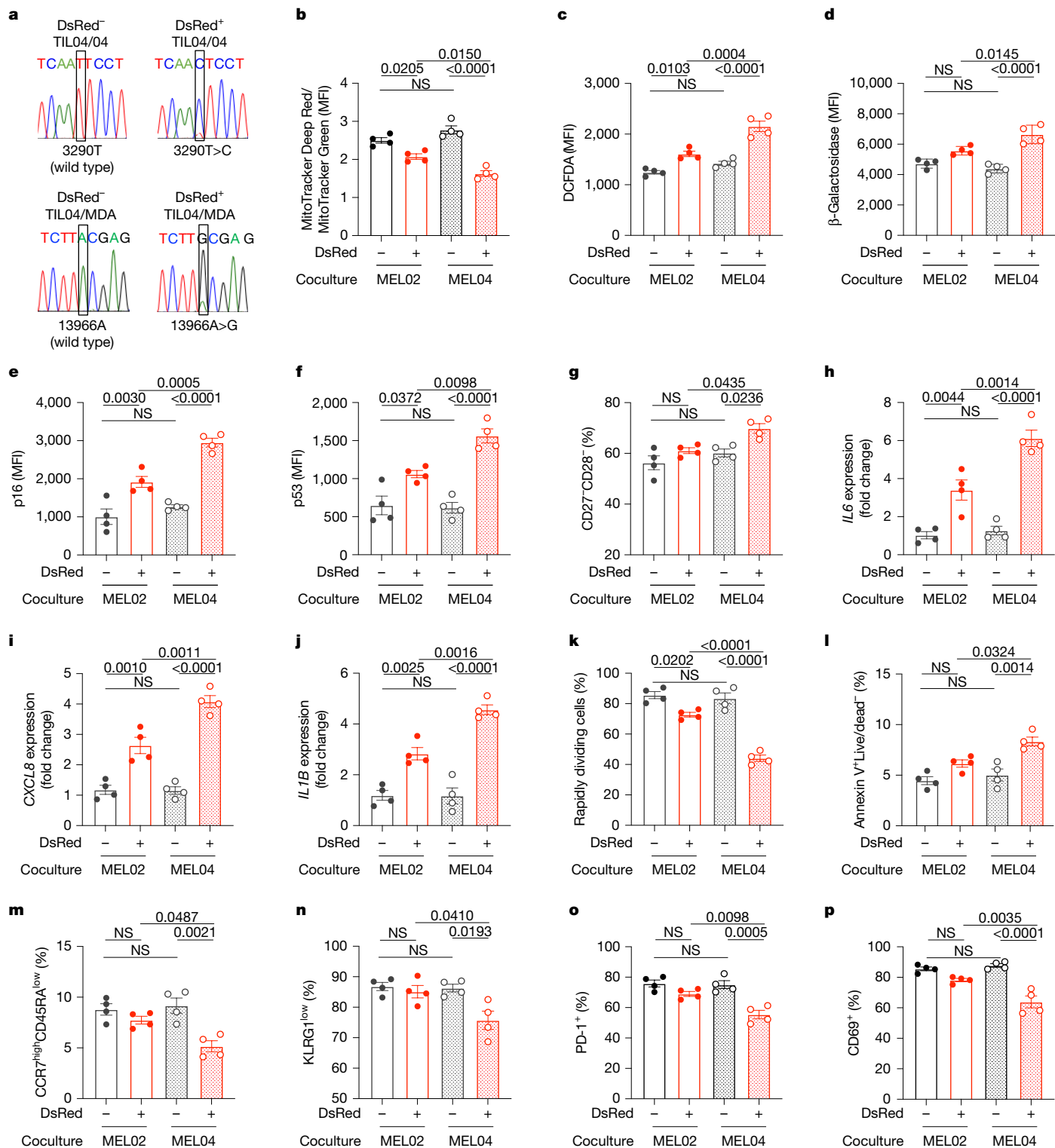


Fig. 4 | TIL function is impaired by mtDNA-mutated mitochondrial transfer. **a**, Capillary sequencing chromatograms of mtDNA in DsRed⁻ TIL04#9 cells and DsRed⁺ TIL04#9 cells. We established DsRed⁻ TIL04#9/02 (wild type), DsRed⁺ TIL04#9/02 (wild type), DsRed⁻ TIL04#9/04 (wild type), DsRed⁺ TIL04#9/04 (mutated), DsRed⁻ TIL04#9/MCF7 (wild type), DsRed⁺ TIL04#9/MCF7 (wild type), DsRed⁻ TIL04#9/MDA (wild type) and DsRed⁻ TIL04#9/MDA cells (mutated), as described in Supplementary Fig. 4. **b–p**, The following parameters were analysed in TILs established in **a**: membrane potentials, evaluated using MitoTracker Deep Red and Green (**b**); cellular ROS production, evaluated using DCFDA (**c**); β-galactosidase activity (**d**); p16 (**e**) and

p53 (**f**) expression; CD27 CD28⁻ senescent fraction (**g**); IL6 (**h**), CXCL8 (**i**) and IL1B (**j**) expression; rapidly dividing cells, evaluated by CFSE dilution (**k**); apoptosis, evaluated using Annexin V (**l**); frequencies of CCR7^{high}CD45RA^{low} central memory (**m**) and KLRL1^{low} long-lived (**n**) fractions; and PD-1 (**o**) and CD69 (**p**) expression. To analyse cell division, PD-1 and CD28 monoclonal antibodies. Rapidly dividing cells were counted after the third division on day 3. Quantifications are shown ($n = 4$ per group). P values (shown on charts) were calculated using one-way ANOVA with Bonferroni corrections (**b–p**). Error bars show s.e.m.

cocultured with MELO2-MitoDsRed cells or MELO4-MitoDsRed cells, the mtDNA-mutated DsRed⁺CCR7^{high}CD45RA^{low} central memory fraction was slightly more apoptotic than the wild-type cells. By contrast, the other fractions had comparable apoptotic levels between the wild-type and mutated cells (Extended Data Fig. 3l). These data suggest that mtDNA mutations primarily impair memory formation and partially induce apoptosis in the central memory fraction. When we evaluated effector functions after T cell stimulation using anti-CD3 and anti-CD28 monoclonal antibodies, the activation markers PD-1 and CD69 were significantly reduced in mtDNA-mutated DsRed⁺TIL04#9/04 cells. This finding suggests that mtDNA-mutated TILs cannot be efficiently activated because the function of mitochondria is impaired (Fig. 4o,p). To confirm these results, TILs with non-mutated mitochondria and TILs with mutated mitochondria transferred after coculture with breast cancer cells were analysed. MitoDsRed-labelled MCF7 cells (wild type) and MDA-MB-231 cells (mutated) (Fig. 4a and Supplementary Figs. 2 and 4) showed similar results to those obtained with the MELO2 and MELO4 cells (Extended Data Fig. 4a–l). Experiments using mtDNA-mutated MELc03 cells and cloned wild-type mtDNA TILc03#5 cells showed similar but weaker trends (Extended Data Fig. 4m–p). This reduced effect may be because the mtDNA mutation in MELc03 cells is heteroplasmic (Extended Data Fig. 1c and Supplementary Figs. 2 and 4). Notably, treatment with a USP30 inhibitor or siRNAs targeting *USP30* in these coculture conditions partially prevented TIL dysfunction (Extended Data Fig. 2j–m).

Next, we created mtDNA-deficient Rho⁰ cells (Jurkat/Rho⁰) by culturing them with ethidium bromide and then mitochondria isolated from cancer cells (MELO2, wild type; MELO4, mutated; MCF7, wild type; and MDA-MB-231, mutated) using a MitoCeption protocol⁴⁹ were transferred to the Jurkat/Rho⁰ cells (Rho⁺MELO2-Mito, Rho⁺MELO4-Mito, Rho⁺MCF7-Mito and Rho⁺MDA-Mito, respectively) (Supplementary Fig. 4). We adjusted the amount of mtDNA so that each cell line had the same and confirmed the presence of mutations (Extended Data Fig. 5a,b). mtDNA-mutated Rho⁺MELO4-Mito cells and Rho⁺MDA-Mito cells had significantly reduced membrane potentials (Extended Data Fig. 5c). We then used a flux analyser to assess mitochondrial OXPHOS and glycolysis levels, and the results showed that mtDNA-mutated Jurkat cells had reduced basal respiration and an increased dependency on glycolysis (Extended Data Fig. 5d,e). Similar results were obtained when ATP composition was evaluated, with total ATP and ATP produced by OXPHOS reduced in mtDNA-mutated Jurkat cells (Extended Data Fig. 5f). Accordingly, the mtDNA-mutated Jurkat cells exhibited a substantial increase in ROS production (Extended Data Fig. 5g). Similar to primary TILs, mtDNA-mutated Jurkat cells showed increased β-galactosidase activity (Extended Data Fig. 5h), reduced division potential and were more apoptotic (Extended Data Fig. 5i,j). The CCR7^{high}CD45RA^{low} central memory and long-lived KLRG1^{low} cell fractions were significantly reduced in mtDNA-mutated Jurkat cells (Extended Data Fig. 5k,l). After treatment with anti-CD3 and anti-CD28 monoclonal antibodies, PD-1 expression was significantly reduced in mtDNA-mutated Jurkat cells (Extended Data Fig. 5m). When these Rho⁺ cells were cultured in normal medium without sodium pyruvate and uridine, mtDNA bands were still observed. This result indicates that mtDNA-mutated mitochondria are maintained after homoplasmic replacement (Extended Data Fig. 5n). Together, these results show that T cells that receive cancer-cell-derived mtDNA-mutated mitochondria can become senescent and have defects in effector functions and memory formation, together with metabolic abnormalities.

EV-mediated transfer of mtDNA can alter mitochondrial function in recipient cells^{21,22,26,27}. Thus, we created T cell lines in which mitochondria are transferred through EVs (Supplementary Fig. 4). EVs extracted from MELO2 cells (wild-type mtDNA) and MELO4 cells (mutated mtDNA) were added to Jurkat/Rho⁰ cells. The amount of mtDNA was adjusted so that each cell line had the same and the presence of mutations was confirmed (Extended Data Fig. 6a,b). The membrane potential, metabolic

function, senescence, metabolic status, ROS production, cell division, apoptosis, memory formation and activation parameters showed similar trends to those observed in primary TILs and in Jurkat cells in which mitochondria were directly transferred (Extended Data Fig. 6c–m). Thus, the transfer of mtDNA-mutated mitochondria through EVs from cancer cells can also cause mitochondrial dysfunction in T cells.

In vivo transfer and antitumour immunity

To further investigate the effects of mitochondrial transfer *in vivo*, we used another cell line established from mouse Lewis lung carcinoma with non-mutated mtDNA (LLC/P29 cells)¹⁷ (Supplementary Fig. 2). The expression of ND6 protein in *Nd6*-mutated LLC/A11 cells was lower than in LLC/P29 cells (Extended Data Fig. 3c). mtDNA-mutated LLC/A11 cells had impaired OXPHOS and increased dependency of glycolysis and reduced activities of complex I (Extended Data Fig. 3d–i). We introduced MitoDsRed into LLC/P29 cells (LLC/P29-MitoDsRed) (Supplementary Fig. 2) and analysed TILs in LLC/P29-MitoDsRed and LLC/A11-MitoDsRed tumours on day 42 (Supplementary Fig. 3). CD8⁺ T cell infiltration was comparable between LLC/P29 and LLC/A11 tumours (Extended Data Fig. 7a). Moreover, DsRed expression in tumour-infiltrating CD8⁺ T cells, indicative of mitochondrial transfer, was also comparable (Fig. 5a). LLC/P29 cells had a single-nucleotide polymorphism (SNP) (*Nd6*, 13672A>T) (Supplementary Fig. 2), and sorted DsRed⁺ T cells from TILs had this SNP but DsRed[−] TILs did not, as observed in LLC/A11 cells (Extended Data Fig. 7b). DsRed⁺CD8⁺ T cells that received mitochondria with the mtDNA mutation from LLC/A11 tumours exhibited significantly higher β-galactosidase activity and were more apoptotic (Fig. 5b,c). Moreover, a reduced frequency in CD127^{high}KLRG1^{low} long-lived memory precursor effector T cells (MPECs) was observed⁵⁰ (Fig. 5d). PD-1 expression in DsRed⁺CD8⁺ T cells from LLC/A11 tumours with the mtDNA mutation was significantly lower than in DsRed⁺CD8⁺ T cells from LLC/P29 tumours with non-mutated mtDNA. This finding suggests that mtDNA-mutated CD8⁺ T cells cannot be efficiently activated owing to mitochondrial dysfunction (Fig. 5e and Supplementary Fig. 5), a result similar to that observed for the *in vitro* experiments. Furthermore, DsRed⁺PD-1⁺CD8⁺ T cells in LLC/A11 tumours exhibited a more terminally differentiated exhaustion phenotype, with high TIM3 and low TCF1 expression compared with those in LLC/P29 mouse models^{51,52} (Fig. 5f). We transplanted LLC/P29 or LLC/A11 tumours into OT-1 mice and collected DsRed⁺CD8⁺ T cells from TILs. Killing assays against OVA-overexpressing cancer cells were performed using these selected T cells. Mitochondrial transfer with wild-type mtDNA (LLC/P29 cells) slightly reduced cytotoxic activity, whereas mtDNA-mutated mitochondrial transfer (LLC/A11 cells) markedly reduced such activity (Fig. 5g). Accordingly, CD8⁺ T cell depletion promoted LLC/P29 tumour growth but little LLC/A11 tumour growth (Extended Data Fig. 7c). Moreover, LLC/P29 cells grew more rapidly *in vitro* than LLC/A11 cells (Extended Data Fig. 7d). This result indicates that CD8⁺ T cells in LLC/A11 tumours are dysfunctional because of the transfer of mitochondrial with mutated mtDNA. We sorted mitochondria-transferred DsRed⁺ T cells from TILs, which were subsequently cultured *in vitro*. Along with gradually decreased DsRed expression in bulk TILs (Extended Data Fig. 2a), the impairment in functions was partially recovered (Extended Data Fig. 7e,f). Notably, LLC/P29 tumours (non-mutated mtDNA) responded to PD-1 blockade, whereas LLC/A11 tumours (mutated mtDNA) failed to respond and PD-1 blockade did not affect mitochondrial transfer (Fig. 5h and Supplementary Fig. 3).

As EVs can have crucial roles in transfer, we treated these tumours with the EV release inhibitor GW4869 (Supplementary Fig. 3). Mitochondrial transfer was reduced by GW4869, which in turn resulted in reduced β-galactosidase activity and apoptosis (Fig. 5i–k) and increased frequencies of MPECs and PD-1⁺CD8⁺ T cells in TILs (Fig. 5l,m). Furthermore, GW4869 reversed the exhaustion phenotype from terminally

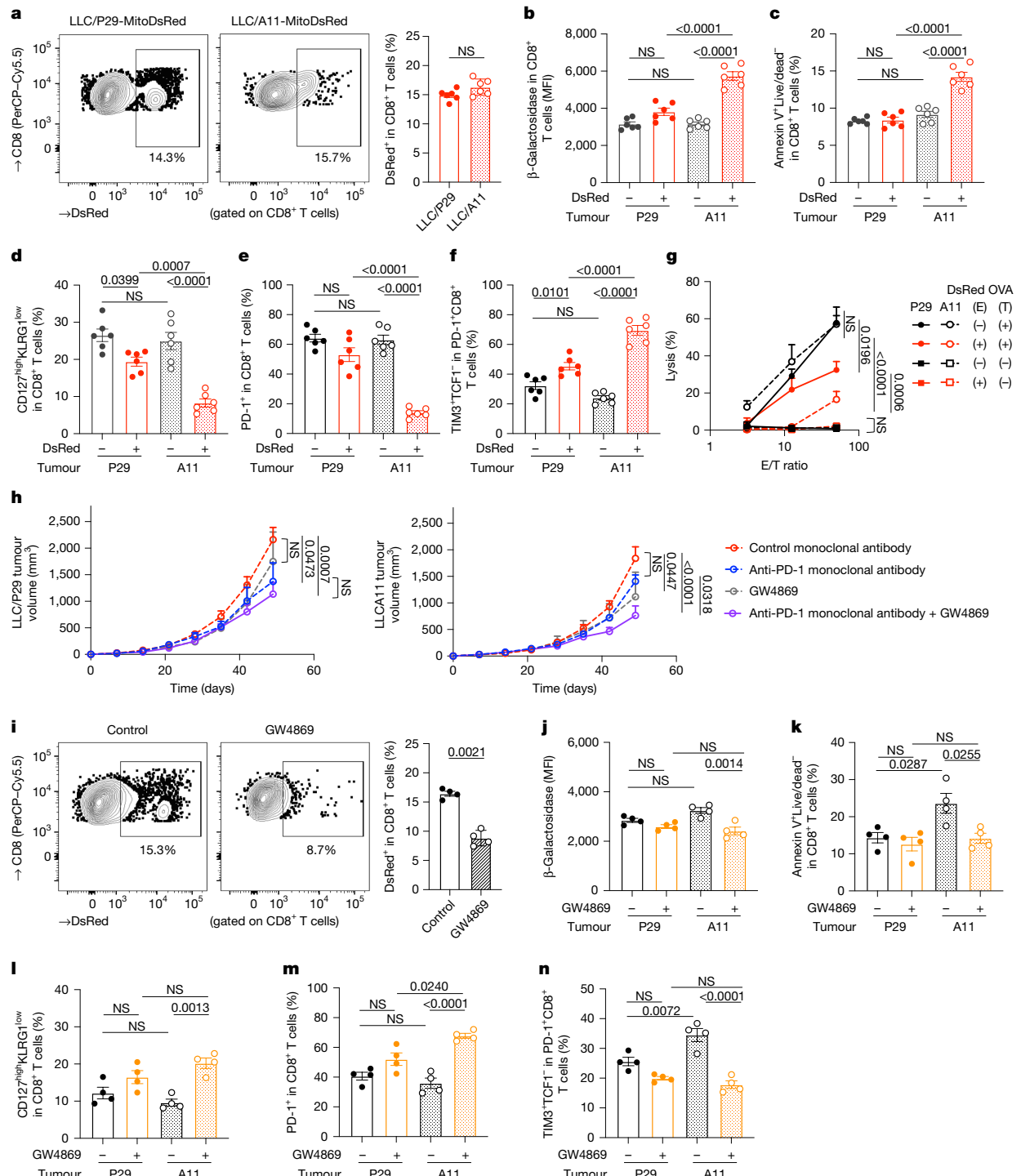


Fig. 5 | mtDNA-mutated mitochondrial transfer reduces antitumour immunity in vivo. **a**, Comparison of mitochondrial transfer rates. In vivo experiments were performed as described in Supplementary Fig. 3. Representative flow cytometry staining (left) and quantification (right) are shown ($n = 6$ per group). **b–f**, β -Galactosidase activity (**b**), apoptosis evaluated by Annexin V (**c**), frequency of CD127^{high}KLRG1^{low} MPECs (**d**), PD-1 expression (**e**) in CD8⁺ TILs, and frequency of TIM3⁺TCF1⁺ terminally differentiated exhausted CD8⁺ T cells in PD-1⁺CD8⁺ TILs (**f**) from LLC/P29-MitoDsRed or LLC/A11-MitoDsRed tumours. In vivo experiments were performed as described in Supplementary Fig. 3. Quantifications are shown ($n = 6$ per group). **g**, Killing assays. LLC/P29-MitoDsRed or LLC/A11-MitoDsRed cells were subcutaneously injected into OT-1 mice. Forty-two days later, we sorted DsRed⁺ and DsRed[−]CD8⁺ T cells from each TIL fraction (effector cells (**E**)), with which we performed a killing assay against LLC/P29-OVA or LLC/A11-OVA cells (target cells (**T**)), respectively. Quantifications are shown ($n = 4$ per group). **h**, Tumour growth

of LLC/P29-MitoDsRed and LLC/A11-MitoDsRed tumours treated with an anti-PD-1 antibody and/or an EV release inhibitor (GW4869). In vivo experiments were performed as described in Supplementary Fig. 3 ($n = 6$ per group). **i**, Mitochondrial transfer after GW4869 local injection. In vivo experiments were performed as described in Supplementary Fig. 3. Representative flow cytometry staining (left) and summary (right) are shown ($n = 4$ per group). **j–n**, β -Galactosidase activity (**j**), apoptosis evaluated by Annexin V (**k**), frequency of CD127^{high} KLRG1^{low} MPECs (**l**), PD-1 expression (**m**) in CD8⁺ TILs, and frequency of TIM3⁺TCF1⁺ terminally differentiated exhausted CD8⁺ T cells in PD-1⁺CD8⁺ TILs (**n**) from LLC/P29-MitoDsRed and LLC/A11-MitoDsRed tumours treated with GW4869. In vivo experiments were performed as described in Supplementary Fig. 3. Quantifications are shown ($n = 4$ per group). *P* values (shown on charts) were calculated using two-sided *t*-tests (**a,i**), one-way ANOVA with Bonferroni corrections (**b–g,j–n**) or two-way ANOVA with Bonferroni corrections (**h**). Error bars show s.e.m.

Article

differentiated to stem-like progenitor exhaustion (Fig. 5n). GW4869 treatment inhibited LLC/A11 tumour growth but not LLC/P29 tumour growth, and overcame the resistance to PD-1 blockade in LLC/A11 tumours (Fig. 5h and Supplementary Fig. 3). Notably, GW4869 did not have any effect on LLC/A11 tumour growth in immunodeficient SCID mice (Extended Data Fig. 7g).

We conducted *in vivo* adoptive T cell transfer experiments using immunodeficient SCID mice with LLC/P29-OVA-MitoDsRed and LLC/A11-OVA-MitoDsRed tumours (Supplementary Fig. 3). DsRed expression in tumour-infiltrating CD8⁺ T cells transferred from OT-1 mice was significantly higher than that from C57BL/6J wild-type mice (Extended Data Fig. 7h). This result highlights the importance of long-term persistence and direct cell-cell contact in the TME in T cell transfer. When CD8⁺ T cells from OT-1 mice were transferred, DsRed⁺CD8⁺ T cells that received mitochondrial transfer from LLC/A11-OVA tumours (mutated mtDNA) had lower PD-1 expression than DsRed⁺CD8⁺ T cells from LLC/P29-OVA tumours (non-mutated mtDNA) (Extended Data Fig. 7i). Furthermore, DsRed⁺PD-1⁺CD8⁺ T cells in LLC/A11-OVA tumours exhibited a more terminally differentiated exhaustion phenotype than those in LLC/P29-OVA tumours (Extended Data Fig. 7j). Accordingly, the T cells transferred from OT-1 mice exhibited antitumour effects against LLC/P29-OVA tumours but not LLC/A11-OVA tumours (Extended Data Fig. 7k). Overall, these results show that mtDNA-mutated mitochondria transferred from cancer cells to TILs can reduce antitumor immunity, including that mediated by PD-1 blockade, through T cell dysfunction *in vivo*.

Mitochondrial function and ICI efficacy

For further *in vivo* analyses, we created a conditional knockout mouse model in which T cells have mitochondrial dysfunction (*Tfam*^{fl/fl}*Cd4*^{cre} mice)⁴⁷. In these mice, mitochondrial mass in T cells was decreased, basal mitochondria respiration was reduced, dependency on glycolysis was increased and T cells were senescent (Extended Data Fig. 8a–d). Moreover, the efficacy of PD-1 blockade was impaired in *Tfam*^{fl/fl}*Cd4*^{cre} mice (Extended Data Fig. 8e and Supplementary Fig. 3). PD-1 blockade increased the frequencies of tumour-infiltrating CD44^{high}CD62L^{low} effector memory CD8⁺ T cells, PD-1⁺CD8⁺ T cells and granzyme B⁺CD8⁺ T cells in the control mice but not in the *Tfam*^{fl/fl}*Cd4*^{cre} mice (Extended Data Fig. 8f–h).

Next, using these mice, we performed rechallenge experiments to evaluate memory formation and durable responses to PD-1 blockade. Mice that had complete eradication of the initial tumours after anti-PD-1 monoclonal antibody treatment were rechallenged with the same cancer cells on day 32 (Supplementary Fig. 3). After complete eradication, most of the rechallenged tumours were rejected in control mice (Extended Data Fig. 8i), whereas more than half of the rechallenged tumours were not rejected in *Tfam*^{fl/fl}*Cd4*^{cre} mice (MC-38 tumours, 8 out of 8 versus 2 out of 6, *P* < 0.05; and B16F10-OVA tumours, 6 out of 8 versus 1 out of 8, *P* < 0.05) (Extended Data Fig. 8i). The frequency of senescent CD27⁻CD28⁻CD8⁺ T cells in TILs was increased in *Tfam*^{fl/fl}*Cd4*^{cre} mice (Extended Data Fig. 8j), whereas the frequency of KLRG1^{low}CD127^{high}CD8⁺ TILs (MPECs) was reduced (Extended Data Fig. 8k). Moreover, the frequency of MPECs in control mice increased after PD-1 blockade, whereas it did not in *Tfam*^{fl/fl}*Cd4*^{cre} mice (Extended Data Fig. 8k).

To evaluate these results in the human setting, we analysed clinical data from patients with melanoma (cohort B, *n* = 95) and from patients with NSCLC (cohort C1, *n* = 86) who received first-line PD-1 blockade therapy without any cytotoxic chemotherapies (Extended Data Table 1). We also analysed additional samples from patients with advanced NSCLC who received first-line platinum-doublet cytotoxic chemotherapies without any ICIs (cohort C2, *n* = 56) (Supplementary Table 3). Few patients in cohorts C1 and C2 had driver mutations, because such individuals generally received molecularly

targeted therapies as first-line therapy before PD-1 blockade therapy or platinum-doublet cytotoxic chemotherapies. As summarized in Extended Data Fig. 9a–c and Supplementary Table 4, we identified 158 mtDNA variants, including 48 frameshift and 110 substitution variants, from 237 FFPE tumour samples. The variants were classified as mtDNA-mutation-positive if they presented truncating, missense, tRNA or rRNA variants (cohort B, 31 out of 95; cohort C1, 44 out of 86; cohort C2, 20 out of 56) and as mtDNA-mutation-negative if they had D-loop, intergenic site, silent variants or no variants. Chronic sun damage seemed to be associated with mtDNA mutations in our melanoma cohort, as they were significantly more common in melanomas located on the head, neck or dorsal surface of the distal extremities⁵³ (Extended Data Table 1). Consistent with our experimental results, analyses of patient tumour samples showed that patients with mtDNA mutations had significantly shorter progression-free survival and overall survival after initiation of PD-1 blockade therapies than individuals without mtDNA mutations (Extended Data Fig. 9d). By contrast, mtDNA mutations did not affect prognosis in patients with NSCLC treated with first-line platinum-doublet cytotoxic chemotherapies without any ICIs (Extended Data Fig. 9e). Overall, mtDNA-mutated mitochondrial transfer in the TME can impair antitumour immunity, which in turn leads to reduced ICI efficacy (Supplementary Fig. 6).

Discussion

Several studies have shown that mitochondrial dysfunction in TILs impairs antitumour immunity^{3,4}. However, the detailed mechanisms and clinical significance of this process were unclear¹¹. We sequenced mtDNA in TILs and frequently detected shared mutations with cancer cells. Furthermore, we demonstrated that mtDNA-mutated mitochondrial transfer from cancer cells to T cells in the TME leads to T cell dysfunction. Notably, the presence of mtDNA mutations in tumour tissue samples predicted poor outcomes in PD-1 blockade therapies. These findings suggest that mtDNA-mutated mitochondrial transfer from cancer cells to TILs causes mitochondrial dysfunction and impairments in antitumour immunity.

mtDNA is highly prone to mutations owing to the lack of histone protection and poor repair mechanisms^{12,13}. The mtDNA 3290T>C mutation we analysed is located in the region encoding tRNA-Leu (UUR). Some tRNA mutations are thought to prevent tm5U-modifying enzymes from recognizing the tRNAs, which results in defective mitochondrial translation owing to impaired taurine modification^{40,41}. Indeed, this mutation induced defective mitochondrial translation (which was restored by taurine treatment), reduced OXPHOS and increased the dependency on glycolysis. Other mtDNA mutations we analysed also impaired OXPHOS and promoted glycolysis. Beyond the mutations we evaluated, numerous other mtDNA mutations that can induce mitochondrial dysfunction have been reported⁵⁴. Thus, many mtDNA mutations in cancer cells can induce mitochondrial dysfunction in TILs through mitochondrial transfer.

Previous studies have experimentally shown mitochondrial transfer through TNTs and/or small EVs rather than microEVs or naked mitochondria^{20–27,30–32}. Several studies used MitoTracker to evaluate the transfer process, but this method has limitations owing to leakage²⁹. To address this issue, we used mitochondrial reporter proteins, and the results confirmed the importance of TNT formation and small EVs to the transfer process. We purified EVs smaller than 200 nm and detected a mitochondrial protein together with CD9 and TSG101, indicating that small EVs actually contain mitochondria. Furthermore, blocking the release of small EVs inhibited transfer and PD-1 blockade resistance, which reversed the TIL phenotype. However, as previously reported, EVs can contain other immunomodulatory factors⁵⁵. Thus, we also performed pure mitochondrial transfer using the MitoCep technique⁴⁹, and results from these experiments confirmed the effects associated with mtDNA mutations. T cells generally have

approximately 200–400 copy numbers of mtDNA⁵⁶; therefore, it may seem challenging to achieve homoplasmic replacement through mitochondrial transfer alone. Our results showed that the number of *in situ* mitochondria in T cells decreased owing to ROS-induced mitophagy from cancer cells, and this effect was reversible after treatment with an antioxidant or a mitophagy inhibitor. Mitophagy is often impaired in cancer cells⁵⁷, and mitophagy-inhibitory molecules such as USP30 are highly expressed in various cancer cells^{35–37} but not in T cells. Here we showed that USP30 in cancer cells could transfer to TILs together with the mitochondria. Mitochondria transferred from cancer cells along with USP30 did not undergo mitophagy. Moreover, inhibiting USP30 reduced mitochondrial transfer from cancer cells, which partially prevented the replacement to homoplasmy and affected TIL functions. This mitophagy difference in mitochondria between cancer cells and T cells, with respect to mitophagy-inhibitory molecules such as USP30, might explain the mechanism of homoplasmic replacement. However, other factors probably contribute, which presents a challenge for future research. Moreover, considering mitochondrial dynamics such as fusion and fission, other mechanisms may also be involved¹⁰; therefore further studies are warranted.

Mitochondria are essential for T cell metabolism^{2,10}, and OXPHOS dysfunction in T cells leads to impaired effector functions and memory formation⁴⁷. Although T cell effector differentiation depends on glycolysis², mtDNA mutations can impair T cell activation owing to poor energy production^{2–4}. PD-1 expression increases during T cell activation, which acts as a negative-feedback loop to inhibit T cell function. Therefore, our data suggested that mtDNA-mutated T cells cannot be efficiently activated. Mitochondrial dysfunction can also affect T cell exhaustion^{3,4}, and our results confirmed this effect. However, we also demonstrated that mitochondrial dysfunction in TILs can result from mtDNA mutations transferred from cancer cells. Consequently, mtDNA-mutated tumours showed resistance to PD-1 blockade, but EV inhibition reversed this. The mouse models we used have some limitations, as specific inhibition of mitochondrial transfer was difficult. However, the *in vitro* data showed that small EVs have a key role in the transfer process, with partial recovery of T cell functions after inhibitor treatment. CD8⁺ T cell depletion and adoptive transfer models further underscored the importance of mtDNA mutations. Although we wish we had a more robust *in vivo* model, this is an issue that will need to be addressed in future research. Clinical data from melanoma and NSCLC samples showed that the presence of mtDNA mutations is a poor prognostic factor for PD-1 blockade therapies but not for chemotherapies alone (that is, without PD-1 blockade therapies). In previous studies of patients who did not receive immunotherapies, the prognostic significance of mtDNA mutations has been controversial^{15,16,58}. We observed that 75% of mtDNA mutations in TILs were shared with cancer cells, which indicates that TILs frequently receive mitochondria through transfer from cancer cells. Moreover, mtDNA mutations were found in 5 out of 12 TILs, a frequency similar to that observed in FFPE tumour sequencing. Considering these findings, although we could not accurately evaluate mtDNA mutations in TILs from FFPE samples, most mtDNA mutations in TILs are probably transferred from cancer cells. These results confirm the importance of T cell mitochondria, particularly mtDNA mutations, in antitumour immunity.

Mitochondrial transfer might occur between many cell types in the TME. Although several studies have shown transfer from immune cells to cancer cells^{22,24}, replacement to homoplasmy in cancer cells could be rare owing to cancer cell ROS and mitophagy sensitivity in immune-cell mitochondria. In cancer cells with heteroplasmy, complete replacement of TILs may not occur, but a high mutation frequency (more than 60–80%) can still affect T cell function⁵⁹. Thus, complete replacement, which does not always occur, may not be necessary to affect T cell function.

In summary, we identified mtDNA mutations in TILs as a cause of mitochondrial dysfunction. Many mutations were shared with cancer

cells, and mitochondrial transfer from cancer cells to TILs probably occurs. Mutated T cells exhibited metabolic abnormalities and senescence, with defects in effector functions and memory formation, which in turn affected PD-1 blockade immunity. Patients with mtDNA mutations treated with PD-1 blockade therapy had a poor prognosis. These findings highlight a previously unknown immune-evasion mechanism of cancer cells that uses mitochondrial transfer.

Online content

Any methods, additional references, Nature Portfolio reporting summaries, source data, extended data, supplementary information, acknowledgements, peer review information; details of author contributions and competing interests; and statements of data and code availability are available at <https://doi.org/10.1038/s41586-024-08439-0>.

- Schreiber, R. D., Old, L. J. & Smyth, M. J. Cancer immunoediting: integrating immunity's roles in cancer suppression and promotion. *Science* **331**, 1565–1570 (2011).
- DePaeux, K. & Delgoffe, G. M. Metabolic barriers to cancer immunotherapy. *Nat. Rev. Immunol.* **21**, 785–797 (2021).
- Scharping, N. E. et al. The tumor microenvironment represses T cell mitochondrial biogenesis to drive intratumoral T cell metabolic insufficiency and dysfunction. *Immunity* **45**, 374–388 (2016).
- Yu, Y. R. et al. Disturbed mitochondrial dynamics in CD8. *Nat. Immunol.* **21**, 1540–1551 (2020).
- Topalian, S. L. et al. Safety, activity, and immune correlates of anti-PD-1 antibody in cancer. *N. Engl. J. Med.* **366**, 2443–2454 (2012).
- Hodi, F. S. et al. Improved survival with ipilimumab in patients with metastatic melanoma. *N. Engl. J. Med.* **363**, 711–723 (2010).
- Brahmer, J. R. et al. Safety and activity of anti-PD-L1 antibody in patients with advanced cancer. *N. Engl. J. Med.* **366**, 2455–2465 (2012).
- Nagasaki, J., Ishino, T. & Togashi, Y. Mechanisms of resistance to immune checkpoint inhibitors. *Cancer Sci.* **113**, 3303–3312 (2022).
- Sharma, P., Hu-Lieskovian, S., Wargo, J. A. & Ribas, A. Primary, adaptive, and acquired resistance to cancer immunotherapy. *Cell* **168**, 707–723 (2017).
- Mills, E. L., Kelly, B. & O'Neill, L. A. J. Mitochondria are the powerhouses of immunity. *Nat. Immunol.* **18**, 488–498 (2017).
- Siska, P. J. et al. Mitochondrial dysregulation and glycolytic insufficiency functionally impair CD8 T cells infiltrating human renal cell carcinoma. *JCI Insight* **2**, e93411 (2017).
- Alexeyev, M., Shokolenko, I., Wilson, G. & LeDoux, S. The maintenance of mitochondrial DNA integrity—critical analysis and update. *Cold Spring Harb. Perspect. Biol.* **5**, a012641 (2013).
- Sabharwal, S. S. & Schumacker, P. T. Mitochondrial ROS in cancer: initiators, amplifiers or an Achilles' heel? *Nat. Rev. Cancer* **14**, 709–721 (2014).
- Yuan, Y. et al. Comprehensive molecular characterization of mitochondrial genomes in human cancers. *Nat. Genet.* **52**, 342–352 (2020).
- Hopkins, J. F. et al. Mitochondrial mutations drive prostate cancer aggression. *Nat. Commun.* **8**, 656 (2017).
- Gorelick, A. N. et al. Respiratory complex and tissue lineage drive recurrent mutations in tumour mtDNA. *Nat. Metab.* **3**, 558–570 (2021).
- Ishikawa, K. et al. ROS-generating mitochondrial DNA mutations can regulate tumor cell metastasis. *Science* **320**, 661–664 (2008).
- Petros, J. A. et al. mtDNA mutations increase tumorigenicity in prostate cancer. *Proc. Natl Acad. Sci. USA* **102**, 719–724 (2005).
- Mahmood, M. et al. Mitochondrial DNA mutations drive aerobic glycolysis to enhance checkpoint blockade response in melanoma. *Nat. Cancer* **5**, 659–672 (2024).
- Spees, J. L., Olson, S. D., Whitney, M. J. & Prockop, D. J. Mitochondrial transfer between cells can rescue aerobic respiration. *Proc. Natl Acad. Sci. USA* **103**, 1283–1288 (2006).
- Borchering, N. & Brestoff, J. R. The power and potential of mitochondria transfer. *Nature* **623**, 283–291 (2023).
- Zhang, H. et al. Systematic investigation of mitochondrial transfer between cancer cells and T cells at single-cell resolution. *Cancer Cell* **41**, 1788–1802 (2023).
- Tan, A. S. et al. Mitochondrial genome acquisition restores respiratory function and tumorigenic potential of cancer cells without mitochondrial DNA. *Cell Metab.* **21**, 81–94 (2015).
- Saha, T. et al. Intercellular nanotubes mediate mitochondrial trafficking between cancer and immune cells. *Nat. Nanotechnol.* **17**, 98–106 (2022).
- Crewe, C. et al. Extracellular vesicle-based interorgan transport of mitochondria from energetically stressed adipocytes. *Cell Metab.* **33**, 1853–1868 (2021).
- Torralla, D. et al. Priming of dendritic cells by DNA-containing extracellular vesicles from activated T cells through antigen-driven contacts. *Nat. Commun.* **9**, 2658 (2018).
- Takenaga, K., Koshikawa, N. & Nagase, H. Intercellular transfer of mitochondrial DNA carrying metastasis-enhancing pathogenic mutations from high- to low-metastatic tumor cells and stromal cells via extracellular vesicles. *BMC Mol. Cell Biol.* **22**, 52 (2021).
- Ebrahimi-Fakhari, D. et al. Impaired mitochondrial dynamics and mitophagy in neuronal models of tuberous sclerosis complex. *Cell Rep.* **17**, 1053–1070 (2016).
- Chen, C., Li, H., Zhang, J. & Cheng, S. C. Exploring the limitations of mitochondrial dye as a genuine horizontal mitochondrial transfer surrogate. *Commun. Biol.* **7**, 281 (2024).
- Catalano, M. & O'Driscoll, L. Inhibiting extracellular vesicles formation and release: a review of EV inhibitors. *J. Extracell. Vesicles* **9**, 1703244 (2020).

31. Li, B., Antonyak, M. A., Zhang, J. & Cerione, R. A. RhoA triggers a specific signaling pathway that generates transforming microvesicles in cancer cells. *Oncogene* **31**, 4740–4749 (2012).
32. Ikeda, G. et al. Mitochondria-rich extracellular vesicles from autologous stem cell-derived cardiomyocytes restore energetics of ischemic myocardium. *J. Am. Coll. Cardiol.* **77**, 1073–1088 (2021).
33. Chiavarina, B. et al. HIF1- α functions as a tumor promoter in cancer associated fibroblasts, and as a tumor suppressor in breast cancer cells: autophagy drives compartment-specific oncogenesis. *Cell Cycle* **9**, 3534–3551 (2010).
34. Zhang, Q. et al. Microvesicles derived from hypoxia/reoxygenation-treated human umbilical vein endothelial cells promote apoptosis and oxidative stress in H9c2 cardiomyocytes. *BMC Cell Biol.* **17**, 25 (2016).
35. Aryapour, E. & Kietzmann, T. Mitochondria, mitophagy, and the role of deubiquitinases as novel therapeutic targets in liver pathology. *J. Cell. Biochem.* **123**, 1634–1646 (2022).
36. Cunningham, C. N. et al. USP30 and parkin homeostatically regulate atypical ubiquitin chains on mitochondria. *Nat. Cell Biol.* **17**, 160–169 (2015).
37. Bingol, B. et al. The mitochondrial deubiquitinase USP30 opposes parkin-mediated mitophagy. *Nature* **510**, 370–375 (2014).
38. Niu, K. et al. USP33 deubiquitinates PRKN/parkin and antagonizes its role in mitophagy. *Autophagy* **16**, 724–734 (2020).
39. Wang, Y. et al. Deubiquitinating enzymes regulate PARK2-mediated mitophagy. *Autophagy* **11**, 595–606 (2015).
40. Suzuki, T. The expanding world of tRNA modifications and their disease relevance. *Nat. Rev. Mol. Cell Biol.* **22**, 375–392 (2021).
41. Asano, K. et al. Metabolic and chemical regulation of tRNA modification associated with taurine deficiency and human disease. *Nucleic Acids Res.* **46**, 1565–1583 (2018).
42. Imanishi, H. et al. Mitochondrial DNA mutations regulate metastasis of human breast cancer cells. *PLoS ONE* **6**, e23401 (2011).
43. Balaban, R. S., Nemoto, S. & Finkel, T. Mitochondria, oxidants, and aging. *Cell* **120**, 483–495 (2005).
44. Shidara, Y. et al. Positive contribution of pathogenic mutations in the mitochondrial genome to the promotion of cancer by prevention from apoptosis. *Cancer Res.* **65**, 1655–1663 (2005).
45. Chouchani, E. T. et al. Ischaemic accumulation of succinate controls reperfusion injury through mitochondrial ROS. *Nature* **515**, 431–435 (2014).
46. Scialò, F. et al. Mitochondrial ROS produced via reverse electrontransport extend animal lifespan. *Cell Metab.* **23**, 725–734 (2016).
47. Desdín-Micó, G. et al. T cells with dysfunctional mitochondria induce multimorbidity and premature senescence. *Science* **368**, 1371–1376 (2020).
48. van der Windt, G. J. et al. Mitochondrial respiratory capacity is a critical regulator of CD8 $^{+}$ T cell memory development. *Immunity* **36**, 68–78 (2012).
49. Caicedo, A. et al. MitoCeption as a new tool to assess the effects of mesenchymal stem/stromal cell mitochondria on cancer cell metabolism and function. *Sci. Rep.* **5**, 9073 (2015).
50. Joshi, N. S. et al. Inflammation directs memory precursor and short-lived effector CD8 $^{+}$ T cell fates via the graded expression of T-bet transcription factor. *Immunity* **27**, 281–295 (2007).
51. Im, S. J. et al. Defining CD8 $^{+}$ T cells that provide the proliferative burst after PD-1 therapy. *Nature* **537**, 417–421 (2016).
52. He, R. et al. Follicular CXCR5-expressing CD8 $^{+}$ T cells curtail chronic viral infection. *Nature* **537**, 412–428 (2016).
53. Krishnan, K. J. & Birch-Machin, M. A. The incidence of both tandem duplications and the common deletion in mtDNA from three distinct categories of sun-exposed human skin and in prolonged culture of fibroblasts. *J. Invest. Dermatol.* **126**, 408–415 (2006).
54. Wallace, D. C. Mitochondrial genetic medicine. *Nat. Genet.* **50**, 1642–1649 (2018).
55. Buzas, E. I. The roles of extracellular vesicles in the immune system. *Nat. Rev. Immunol.* **23**, 236–250 (2023).
56. O'Hara, R. et al. Quantitative mitochondrial DNA copy number determination using droplet digital PCR with single-cell resolution. *Genome Res.* **29**, 1878–1888 (2019).
57. White, E. Deconvoluting the context-dependent role for autophagy in cancer. *Nat. Rev. Cancer* **12**, 401–410 (2012).
58. Hong, Y. S. et al. Deleterious heteroplasmic mitochondrial mutations are associated with an increased risk of overall and cancer-specific mortality. *Nat. Commun.* **14**, 6113 (2023).
59. Stewart, J. B. & Chinberry, P. F. The dynamics of mitochondrial DNA heteroplasmy: implications for human health and disease. *Nat. Rev. Genet.* **16**, 530–542 (2015).

Publisher's note Springer Nature remains neutral with regard to jurisdictional claims in published maps and institutional affiliations.



Open Access This article is licensed under a Creative Commons Attribution-NonCommercial-NoDerivs 4.0 International License, which permits any non-commercial use, sharing, distribution and reproduction in any medium or format, as long as you give appropriate credit to the original author(s) and the source, provide a link to the Creative Commons licence, and indicate if you modified the licensed material. You do not have permission under this licence to share adapted material derived from this article or parts of it. The images or other third party material in this article are included in the article's Creative Commons licence, unless indicated otherwise in a credit line to the material. If material is not included in the article's Creative Commons licence and your intended use is not permitted by statutory regulation or exceeds the permitted use, you will need to obtain permission directly from the copyright holder. To view a copy of this licence, visit <http://creativecommons.org/licenses/by-nc-nd/4.0/>.

© The Author(s) 2025, corrected publication 2025

Methods

Patients and samples

Ten patients with melanoma, one with breast cancer and one with skin squamous cell carcinoma were enrolled in this study, and samples were used to establish TILs and matched cancer cell lines (cohort A; Supplementary Table 1). Participants had undergone surgical resection at Yamanashi University Hospital, Chiba University Hospital, Shinshu University Hospitals or Saitama Medical University International Medical Center. The tumour tissues were processed as previously described⁶⁰. In brief, surgically resected samples were enzymatically digested with 0.1% collagenase, 0.01% hyaluronidase and 30 U ml⁻¹ deoxyribonuclease (Sigma-Aldrich) in RPMI1640 (Thermo Fisher Scientific) at room temperature. The digested tumour cells were subjected to filtration and density-gradient separation before use. Peripheral blood mononuclear cells were obtained from donated blood and through Ficoll-Uropoline density-gradient centrifugation. All participants provided written informed consent.

In addition to abovementioned tumour samples, FFPE tissue samples were obtained from three other groups of participants for mtDNA mutation analyses. Cohort B comprised 95 patients with melanoma treated with anti-PD-1 monoclonal antibody and/or anti-CTLA-4 monoclonal antibody as first-line therapy. FFPE tissue samples were obtained between 2014 and 2020 from Yamanashi University Hospital, Chiba University Hospital, Shinshu University Hospital and Saitama Medical University International Medical Center from 2014 to 2020 (Extended Data Table 1). Cohort C1 comprised 86 patients with NSCLC treated with anti-PD-1 monoclonal antibody monotherapy as first-line treatment. FFPE tissue samples were obtained between 2017 and 2021 from Chiba University Hospital, Okayama University Hospital and Kindai University Hospital (Extended Data Table 1). Cohort C2 comprised 56 patients with NSCLC treated with platinum-doublet cytotoxic chemotherapies without any ICIs as first-line treatment. FFPE tissue samples were obtained between 2011 and 2012 from Chiba University Hospital, Okayama University Hospital and Kindai University Hospitals (Supplementary Table 3). Clinical information on the participants was obtained from their medical records. Informed consent was obtained by the patient opting out on the website of our institutions.

The protocol for this study was approved by the appropriate institutional review boards and ethics committees of Yamanashi University Hospital, Chiba University Hospital, Shinshu University Hospital, Okayama University Hospital, Kindai University Hospital and Saitama Medical University International Medical Center. This study was conducted in accordance with the principles of the Declaration of Helsinki.

Sequencing of total mtDNA from clinical samples

Sequencing of total mtDNA from TILs with matched LCL cells, peripheral blood and/or cancer cells from cohort A was performed. mtDNA was isolated from these cells using a QIAmp DNA Mini kit (Qiagen). We also collected FFPE tumour samples from 95 patients with melanoma (cohort B) and 142 patients with NSCLC (cohorts C1 and C2) and matched normal tissue samples from 45 patients for total mtDNA sequencing. Areas with high tumour content were marked in FFPE samples, and mtDNA from these areas was isolated using a Gene-Read DNA FFPE kit (Qiagen). A Precision ID mtDNA Whole Genome Panel (Thermo Fisher Scientific) was used to amplify the entire mtDNA sequence using 81 primer pairs, followed by library construction and sequencing on an Ion Torrent Proton sequencer (Thermo Fisher Scientific). After adapter trimming using BaseCaller (with parameter settings --trim-qual-cutoff 15 --barcode-filter-minreads 10 --phasing-residual-filter=2.0 --max-phasing-levels 2 --num-unfiltered 1000 --barcode-filter-postpone 1), reads were mapped to the Revised Cambridge Reference Sequence mitochondrial sequence using TMAP (v.5.12.3; -i bam -v -Y -u --prefix-exclude 5-o 2 stage1 map4) to generate binary alignment maps for subsequent analyses. For each sample,

variants were called using Mutect2 in the Genome Analysis Toolkit (v.4.1.8) under mitochondrial mode and with the read filter marked as duplicate disabled. The detected variants were annotated using GRCh38.p14 as the reference by SnpEff (v.5.1d)⁶¹ and subjected to additional candidate validation by EAGLE (v.1.1.1)⁶². Allele frequencies computed by EAGLE (--hetbias=0 and --omega=1e-6) were used as the basis for subsequent variant analyses.

After pooling the EAGLE results from all samples, we used z scores determined from the variant allele frequency (VAF) per position as a metric to evaluate potential variants. Alterations with z scores > 3, VAF > 0.2 and read depths exceeding 100 were selected to minimize false positives from sequencing errors. In cohorts B, C1 and C2, variants with VAF > 0.85 were initially considered polymorphisms and excluded from final reporting under the assumption that somatic variants would not exhibit high VAFs owing to the presence of a substantial fraction of non-cancerous cells in the tumour tissue in the specimens collected. Haplogrep (v.2.4.0; Kulczyński classification mode with 17_FU1 phylotree, 10 top hits, extended final output and heteroplasmy levels set to 0.85)⁶³ was used to characterize potential haplogroups of individual cases and to identify possible unlabelled SNPs from our frequency-based selection criteria. Variants labelled as 'hotspot' and 'local private variant' were regarded as polymorphic variants; filtered variants were visually inspected to exclude probable sequencing errors at the termini of PCR amplicons or in homopolymer sequence stretches. For performance assessment, we compared the presence of true variants, confirmed through a paired analysis of matched tumour and normal tissue samples ($n = 45$), with variants that were called only from tumour samples. Using these criteria, true variants were called with a false-positive rate of 0% and a false-negative rate of 12.2%.

In cohort A, if a sample had LCL, PBL, TIL and/or cancer cell sequencing data, the results were compared with LCLs or PBLs as controls for somatic calling; mutations in TILs or cancer cells were not considered somatic if they existed in the matched LCLs. Using this criterion, ten mtDNA mutations were confirmed in TILs and cancer cells (Supplementary Tables 1 and 2). In cohorts B, C1 and C2, we identified 158 variants, including 48 frameshift and 110 substitution variants, from 237 FFPE tumour samples (Supplementary Table 4). For each sample, the overall mtDNA variant status was classified as truncating, missense, silent, tRNA, rRNA, D-loop or intergenic sites. For survival analysis, samples were divided into mtDNA-mutation-positive if they presented truncating, missense, tRNA or rRNA variants (melanoma, 32.6%; NSCLC (C1), 51.2%; NSCLC (C2), 35.7%) and mtDNA-mutations-negative if they had a D-loop or an intergenic site or had silent or no variants.

Cell lines and culture conditions

To establish cancer cell lines, 1×10^7 digested tumour cells were cultured in RPMI1640 medium containing 10% FBS (Cytiva), 1% penicillin-streptomycin (PS) and 1% amphotericin B (Thermo Fisher Scientific). Tumour cells were passaged at approximately 80–90% confluence and used when free of fibroblasts and proliferating beyond the tenth passage. To establish and expand cultured TILs, tumour digests were incubated in RPMI1640 medium supplemented with 10% human AB serum, 1% PS and recombinant human interleukin-2 (rhIL-2; 6,000 IU ml⁻¹, PeproTech) in a humidified 37 °C incubator with 5% CO₂. Half of the medium was aspirated from the wells and replaced with fresh complete medium and rhIL-2 every 2–3 days.

The MC-38 cell line (mouse colon adenocarcinoma) was purchased from Kerafast, and the B16F10 (mouse melanoma), MCF7 (human breast cancer), MDA-MB-231 (human breast cancer) and Jurkat (human T cell leukaemia) cell lines were purchased from the American Type Culture Collection (ATCC). The LLC/P29 and LLC/A11 (mouse lung carcinoma) cell lines were established from mouse Lewis Lung carcinomas as previously described^{17,64,65}. MCF7, MDA-MB-231, MC-38, LLC/P29 and LLC/A11 cells were maintained in Dulbecco's modified Eagle's medium (DMEM; Thermo Fisher Scientific), and Jurkat cells

Article

were cultured in RPMI1640 medium containing 10% FBS and 1% PS in a humidified 37 °C incubator with 5% CO₂. mtDNA-deficient Jurkat (Jurkat/Rho⁰) cells were generated by culturing Jurkat cells in the presence of 200 ng ml⁻¹ ethidium bromide for 6 weeks and then maintained in RPMI1640 medium containing 10% FBS, 1% PS, 100 µg ml⁻¹ sodium pyruvate and 50 µg ml⁻¹ uridine.

All cell lines were used after confirming that they were mycoplasma-free, which was assessed using a PCR Mycoplasma Detection kit (Takara) according to the manufacturer's instructions.

Transmission electron microscopy

For pre-fixation, cell specimens were immersed in 0.1 M PBS, pH 7.4, containing 2% glutaraldehyde and 2% paraformaldehyde for 16–18 h. Post-fixation was performed with 2% osmium tetroxide for 1.5 h. After washing with PBS, the specimens were dehydrated in a graded ethanol series and embedded in a low-viscosity resin (Spurr resin, Polysciences). Subsequently, 80-nm-thick sections were prepared using an ultramicrotome (EM-UC7; Leica) and stained with uranyl acetate and lead citrate. The specimens were observed using a transmission electron microscope (H-7650, Hitachi). We counted and quantified the number of cristae per mitochondrion.

Constructs, virus production and transfection

pcDNA3-TfR-OVA (Addgene, 64600)⁶⁶, pBABE-puro (1764)⁶⁷ and pVL-MitoDsRed (44386)⁶⁸ were purchased from Addgene. The *TfR*-OVA cDNA was cloned into a pBABE-puro vector using In-Fusion Snap Assembly master mix (Takara Bio) according to the manufacturer's instructions. The resulting pBABE-puro-TfR-OVA vector was transfected with a pVSV-G vector (Takara Bio) into packaging cells using Lipofectamine 3000 reagent (Thermo Fisher Scientific). The pVL-MitoDsRed vector was transfected with packaging plasmids (pMDLg/prRE, Addgene, 12251 (ref. 69); pRSV-Rev, Addgene, 12253 (ref. 69); and pMD2.G, Addgene, 12259) into packaging cells using Lipofectamine 3000 reagent. After 48 h, the supernatants were concentrated and transduced into cell lines MELO2, MELO4, MELc03, MCF7, MDA-MB-231, B16F10, LLC/P29 and LLC/A11. The transfected cell lines were named MELO2-MitoDsRed, MELO4-MitoDsRed, MELc03-MitoDsRed, MCF7-MitoDsRed, MDA-MB-231-MitoDsRed, B16F10-OVA, LLC/P29-MitoDsRed, LLC/A11-MitoDsRed, respectively. LLC/P29-OVA-MitoDsRed and LLC/A11-OVA-MitoDsRed cell lines were also generated.

Detection of mtDNA

Capillary sequencing and several primers were used to check the status of mtDNA in cell lines and TILs (Supplementary Table 5). For single-cell sequencing, PrimeSTAR GXL DNA Polymerase (Takara) and the primers were prepared in 96-well plates for sequencing before cell sorting. CD3⁺CD45⁺ T cells were sorted from TILs at the single-cell level into 96-well plates using a cell sorter (FACSMelody; BD Biosciences). Oligonucleotides were amplified by PCR and sequenced (Eurofins Genomics).

Imaging of mitochondrial transfer

TILO4#9 and MELO4 cells were labelled with MitoTracker Green (Thermo Fisher Scientific) and MitoDsRed, respectively. After 24 h, 2 × 10⁵ MELO4-MitoDsRed cells were cocultured with labelled 1 × 10⁶ TILO4#9 cells in a 35-mm glass-bottom culture dish for 2 days and observed under a Leica TSC SP8 confocal laser microscope (Leica Microsystems) without fixation. TILO4#9 cells were labelled with a BV421-conjugated monoclonal antibody specific for CD45 (clone HI100, BioLegend).

For time-lapse imaging, 2 × 10⁵ MELO4-MitoDsRed cells were seeded onto a 35-mm glass-bottom culture dish 24 h before coculture and allowed to adhere. The following day, coculture with 1 × 10⁶ TILO4#9 cells labelled with MitoTracker Green was initiated. Twenty-four hours later, we began capturing images every 30 min using a

digital holographic microscope (3D Cell Explorer CX-A, Nanolive). The images were analysed using Fiji software (<https://imagej.net/software/fiji>).

Quantification of mitochondrial transfer

To quantify the transfer of mitochondria from cancer cells to TILs, MELO4-MitoDsRed cells were cocultured with TILO4#9 cells for 1, 2, 3 or 14 days with or without 10 mM NAC (Cayman Chemical), 20 nM USP30 inhibitor (CMPD-39; MedChemExpress) or siRNAs for *USP30* transfection (si*USP30*-1, CAAAAGGUCAUCUGAGGUAGGCTA; si*USP30*-2, CGUCAGAUUAAGUCAUGAAGAAC; Integrated DNA Technologies). When using siRNAs, we prepared siRNA-transfected cancer cells every 5 days and cocultured them with TILs, replacing the old, transfected cancer cells. siRNA transfection of cancer cells was performed using Lipofectamine RNAiMAX reagent (Thermo Fisher Scientific) according to the manufacturer's protocol. To quantify mitochondrial transfer, MELO2-MitoDsRed or MELO4-MitoDsRed cells were cocultured with TILs (TILO2, TILO4#9 or TILc04) for 2 days in the presence of 1:100 anti-MHC-I monoclonal antibody (anti-human HLA-ABC monoclonal antibody, clone W6/32, Thermo Fisher Scientific), 350 nM TNT inhibitor (cytochalasin B; Wako), 1 µM small EV release inhibitor (GW4869; Cayman Chemical) and/or 5 µM microEV release inhibitor (Y-27632; MedChemExpress)³⁰ with or without cell culture inserts to avoid direct cell-cell contact (3 or 0.4 µm pore; Nunc Polycarbonate Cell Culture Inserts in Multi-Well Plates, Thermo Fisher Scientific). Subsequently, TILs were analysed by flow cytometry.

To quantify the transfer of mitochondria from T cells to cancer cells, we used OT-1 and PhaM^{excised} mice expressing mitochondrial-specific fluorescence (mito-Dendra2), which were obtained from the Jackson Laboratory (Supplementary Fig. 2). OVA-overexpressing LLC/A11 cells were cocultured with or without CD8⁺ T cells from PhaM^{excised} OT-1 mice for 3 days. Afterwards, floating T cells were discarded and LLC/A11 cells were repeatedly washed with PBS. These cells were subsequently analysed by flow cytometry as CD45⁻ cells.

Quantification of mitochondria in T cells

To quantify *in situ* mitochondria in T cells, TILO4#9 cells were labelled with MitoTracker Green for 24 h and then cocultured with MELO4 cells with or without 10 mM NAC for 3 days. To inhibit mitophagy, 100 nM of a mitophagy inhibitor (bafilomycin A1; Adipogen Life Sciences) was added every 12 h for 3 days. Subsequently, the TILs were analysed by flow cytometry.

Quantification of mitochondria in cancer cells

OVA-overexpressing LLC/A11 cells or MELO4 cells were labelled with MitoTracker Green. After 24 h, labelled OVA-overexpressing LLC/A11 cells or MELO4 cells were cocultured with or without CD8⁺ T cells from OT-1 mice or TILO4#9 cells for 3 days, respectively. Floating T cells were then discarded and OVA-overexpressing LLC/A11 cells or MELO4 cells were repeatedly washed with PBS. These cells were then analysed by flow cytometry as CD45⁻ cells.

Gene expression analysis

TILO4#9 cells were cocultured with MELO4-MitoDsRed cells for 14 days, and DsRed⁻ cells and DsRed⁺CD3⁺ T cells were sorted. Total RNA was then extracted using a RNeasy Plus Mini kit (Qiagen) and 100 ng of total RNA was reverse-transcribed into cDNA using Prime-Script RT master mix (Takara). Real-time PCR was performed using PowerUp SYBR Green master mix according to the manufacturer's instructions. For each sample, the ΔC_t for *BNIP3*, *ATF4*, *IL6*, *CXCL8* and *IL1B* versus *ACTB* (used as an internal control) was calculated as $\Delta C_t = C_t(BNIP3, ATF4, IL6, CXCL8 \text{ or } IL1B) - C_t(ACTB)$. The $\Delta\Delta C_t$ for DsRed⁻ cells and DsRed⁺TILO4#9 cells versus TILO4#9 cells was calculated as $\Delta\Delta C_t = \Delta C_t(DsRed^+ \text{ or } DsRed^+ \text{ TILO4#9 cells}) - \Delta C_t(TILO4#9 \text{ cells})$. The primers are listed in Supplementary Table 5.

Evaluation for mitophagy

TIL04#9 cells were labelled with MitoTracker Green. Twenty-four hours later, TIL04#9 cells were cocultured with MEL04-MitoDsRed cells for 3 days with or without 10 mM NAC. Subsequently, the cells were stained with an LC3B-specific polyclonal antibody (Proteintech, Rosemont, 18725-1-AP) followed by an APC-conjugated secondary antibody (goat anti-rabbit IgG, Abcam, ab130805), and observed under a confocal laser microscope or analysed by flow cytometry. We used 10 µM carbonyl cyanide 4-(trifluoromethoxy)phenylhydrazone (FCCP) (Selleck Biotech) as a positive control.

Database analyses

We obtained RNA-sequencing expression data from The Cancer Genome Atlas (TCGA) in the Genomic Data Commons data portal of patients with melanoma from the USCS Xena database (<https://xenabrowser.net>). *USP30*, *USP33* and *USP35* expression data in tumour tissues were used.

USP30 staining and quantification

TIL04#9 cells were labelled with MitoTracker Green and cocultured with MEL04-MitoDsRed cells for 3 days. Subsequently, TIL04#9 cells were stained using an AF546-conjugated anti-USP30 monoclonal antibody (Santa Cruz Biotechnology, sc-515235, B-6) or an anti-USP30 polyclonal antibody (Proteintech, 15402-1-AP) with APC-conjugated secondary monoclonal antibody and observed under a confocal laser microscope or analysed by flow cytometry.

Extraction and evaluation of EVs

EVs in the cell culture medium were isolated using Total Exosome Isolation reagent (Thermo Fisher Scientific) according to the manufacturer's instructions. In brief, 1×10^6 cells were cultured in RPMI1640 medium containing 10% EV-depleted FBS (System Biosciences) for 3 days. The conditioned medium was centrifuged at 400g for 5 min to remove cells, and the supernatant was centrifuged at 2,000g for 30 min to remove cell debris. The supernatant was passed through a syringe filter (0.45 µm pore; GVS North America) and then mixed with 0.5 volumes of Total Exosome Isolation reagent and incubated at 4 °C overnight. The mixture was then passed through a syringe filter (0.22 µm pore) and ultracentrifuged at 10,000g for 60 min at 4 °C. The pellet was resuspended in PBS and purified using a miniPURE-EV size-exclusion chromatography column (HBM-MPEV-10, Hansa-BioMed Life Sciences) according to the manufacturer's instructions. The resulting EVs (less than 200 nm in size) were used for western blotting experiments. In brief, we used CD9 and TSG101 as EV markers⁷⁰. To evaluate the purity of FBS-containing medium-derived EVs, we checked BSA⁷¹. We also evaluated cytochrome c as a mitochondrial protein.

We used a DCFDA/H2DCFDA Cellular ROS Assay kit (Abcam) to detect ROS. In brief, PBL04 cells and MEL04 cells were incubated with 20 µM DCFDA solution for 30 min at 37 °C in 5% CO₂. Next, we extracted and purified EVs from the cells and analysed them by flow cytometry with a PS Capture Exosome Flow Cytometry kit (Wako) to create EV-conjugated beads.

Western blotting

Cell lysates from MEL02, MEL04, MCF7 and MDA-MB-231 cells, EV lysates from MEL02 and MEL04 cells, and medium used for the culture of MEL02 and MEL04 cells were separated by SDS-PAGE and blotted onto polyvinylidene fluoride membranes (Merck Millipore). The membranes were blocked and then incubated with primary antibodies. After washing, the membranes were incubated with horseradish peroxidase (HRP)-conjugated secondary antibodies. Finally, the bands were detected using Clarity Western ECL substrate (Bio-Rad) or ImmunoStar LD (Wako), and confirmed using a LAS4000 system (Cytiva).

The protein concentration in each sample was evaluated and adjusted to each other using Pierce BCA Protein Assay kits (Thermo Fisher Scientific) according to the manufacturer's instruments.

Electron transport chain activity assays

MitoCheck Activity Assay kits (complexes I, II and III, and IV) were purchased from Cayman Chemical. Mitochondrial protein isolation from cell lines was performed using a Mitochondria Isolation kit for cultured cells (Thermo Fisher Scientific) according to the manufacturer's instructions. We used activity buffer with the isolated mitochondrial protein in place of the supplied mitochondria, following the manufacturer's instructions as previously described⁷². Reactions were conducted at 25 °C using a FlexStation 3 microplate reader (Molecular Devices), with readings taken every 30 s for 15 min at the Central Research Laboratory of the Okayama University Medical School.

Creation of mitochondria-transferred TILs for functional analyses

We cocultured wild-type mtDNA TIL04#9 or TILc03#5 cells with melanoma (MEL02-MitoDsRed, wild type; MEL04-MitoDsRed, mutated; MELc03-MitoDsRed, mutated) or breast cancer (MCF7-MitoDsRed, wild type; MDA-MB-231-MitoDsRed, mutated) cells for 14 days and subsequently sorted the TILs according to DsRed expression. The sorted TILs were named as follows: DsRed⁻TIL04#9/02 (wild type), DsRed⁺TIL04#9/02 (wild type), DsRed⁻TIL04#9/04 (wild type), DsRed⁺TIL04#9/04 (mutated), DsRed⁻TIL04#9/MCF7 (wild type), DsRed⁺TIL04#9/MCF7 (wild type), DsRed⁻TIL04#9/MDA (wild type), DsRed⁺TIL04#9/MDA (mutated), DsRed⁻TILc03#5/02 (wild type), DsRed⁺TILc03#5/02 (wild type), DsRed⁻TILc03#5/c03 (wild type) and DsRed⁺TILc03#5/c03 cells (mutated). These TILs were then analysed.

Mitochondria-transferred PBL assay to evaluate differentiation and apoptosis

Sorted CCR7^{high}CD45RA^{high}CD8⁺ naive T cells from PBLs of healthy donors were cocultured with MEL02-MitoDsRed cells or MEL04-MitoDsRed cells for 7 days while being stimulated with an anti-CD3 monoclonal antibody (50 ng ml⁻¹) in the presence of rhIL-7 (10 ng ml⁻¹, PeproTech), rhIL-15 (10 ng ml⁻¹, PeproTech) and rhIL-2 (300 IU ml⁻¹). The central memory fraction and KLRG1 expression level were analysed by flow cytometry. Each CD8⁺ T cell fraction (naive, CCR7^{high}CD45RA^{high}; central memory, CCR7^{high}CD45RA^{low}; effector memory, CCR7^{low}CD45RA^{low}; terminally differentiated effector memory, CCR7^{low}CD45RA^{high}) sorted from PBLs of healthy donors was also cocultured with MEL02-MitoDsRed cells or MEL04-MitoDsRed cells for 4 days in the presence of IL-2 (300 IU ml⁻¹) alone, and apoptosis was analysed by flow cytometry.

Creation of mitochondria-transferred Jurkat cells through MitoCeption or EVs for functional analyses

Mitochondria were isolated from 1×10^6 MEL02 (wild type), MEL04 (mutated), MCF7 (wild type) and MDA-MB-231 (mutated) cells following a MitoCeption protocol using a Mitochondria Isolation kit for cultured cells (Thermo Fisher Scientific) according to the manufacturer's instructions⁴⁹. The isolated mitochondria were added to Jurkat/Rho⁰ cells, which were subsequently incubated for 24 h after centrifugation (2,000g for 15 min). This procedure was repeated four times weekly. EVs isolated using the above-described protocols were added to Jurkat/Rho⁰ cells using the EV-Entry system (System Biosciences), which were immediately centrifuged at 1,500g for 15 min at 4 °C and incubated overnight. These EV-transferred Jurkat/Rho⁰ cells were cultured for 6 weeks, and this procedure was repeated every 5–7 days.

After confirming mitochondrial transfer by PCR and mtDNA sequencing, the transferred Jurkat/Rho⁰ cells were cultured as Rho⁺ cells in RPMI1640 medium containing 10% FBS and 1% PS without sodium pyruvate and uridine. We also performed real-time PCR to quantify mtDNA using the Human Mitochondrial DNA (mtDNA)

Article

Monitoring primer set (Takara) and PowerUp SYBR Green master mix (Thermo Fisher Scientific) according to the manufacturer's instruments, and adjusted the amounts to each other. In brief, this primer set calculates the $2^{\Delta Ct}$ value as the relative mtDNA copy number from the average value of ΔCt (mtDNA: *ND1* – nuclear DNA: *SLCO2B1*) and ΔCt (mtDNA: *NDS* – nuclear DNA: *SERPIN A1*). Then, we calculated the fold changes in mtDNA copy number relative to that of the parental Jurkat cells. The Rho⁺ cells containing mitochondria derived from MELO2, MELO4, MCF7 and MDA-MB-231 cells or EVs derived from MELO2 and MELO4 cells were named Rho⁺MELO2-Mito (wild type), Rho⁺MELO4-Mito (mutated), Rho⁺MCF7-Mito (wild type), Rho⁺MDAMB231-Mito (mutated), Rho⁺MELO2-EV (wild type) and Rho⁺MELO4-EV (mutated) cells, respectively. The procedures are summarized in brief in Supplementary Fig. 4.

Mitochondrial membrane potential analysis

Primary TILs were stained with 200 nM MitoTracker Deep Red and Green, incubated at 37 °C in 5% CO₂ for 15 min and then analysed by flow cytometry. The membrane potential was evaluated on the basis of the ratio of each MFI⁴. Additionally, each Jurkat cell was stained with 250 nM TMRE (Thermo Fisher Scientific), incubated at 37 °C in 5% CO₂ for 20 min and then analysed by flow cytometry.

Characterization of metabolic changes by flux analyses

Metabolic analyses were performed using a flux analyser (Seahorse XF HS mini, Agilent Technologies), according to the manufacturer's instructions. In brief, 0.8 × 10⁵ cells were seeded in supplemented Seahorse XF RPMI medium containing 1 mM pyruvate, 2 mM glutamine and 10 mM glucose (pH 7.4) in poly-D-lysine-coated XFp miniplates, followed by centrifugation at 200g for 1 min at room temperature. The plate was then equilibrated at 37 °C in an incubator without CO₂ for 40 min. The oxygen consumption rate was evaluated with sequential injections of oligomycin (1 μM), FCCP (0.75 μM) and rotenone– antimycin A (0.5 μM). The extracellular acidification rate was evaluated by sequential injections of glucose (10 mM), oligomycin (1 μM) and 2-deoxy-glucose (50 mM). The ATP production rate was evaluated with sequential injections of oligomycin (1.5 μM) and otenone– antimycin A (0.5 μM). All chemicals were purchased from Agilent Technologies. All data were normalized to the cell number.

ROS production analyses

To evaluate ROS production, we used a DCFDA/H2DCFDA Cellular ROS Assay kit (Abcam), as described above.

β-Galactosidase staining to evaluate senescence

A Cellular Senescence Detection kit (Dojindo) was used to assess cellular senescence according to the manufacturer's instructions. In brief, cells were incubated with baflomycin A1 for 1 h at 37 °C in 5% CO₂, then incubated with SPiDER-β-Gal for 30 min and analysed by flow cytometry.

Apoptosis and cellular proliferation assay

Apoptosis was evaluated by combining Annexin V (Thermo Fisher Scientific) and eBioscience Fixable Viability Dye eFluor (Thermo Fisher Scientific) for live/dead cell staining. According to the manufacturer's instructions, each cell was incubated with Annexin V and eFluor for 15 min at room temperature and then analysed by flow cytometry. Cellular proliferation was assessed on the basis of the dilution of cells labelled with carboxyfluorescein succinimidyl ester (CFSE) using a CFSE Cell Proliferation kit (Thermo Fisher Scientific) and flow cytometry. Cells were incubated with 10 μM CFSE for 20 min at 37 °C in 5% CO₂, washed 3 times with RPMI medium and incubated for 3 days, followed by additional live/dead cell staining and flow cytometry analysis.

In vitro cellular proliferation analysis

Twenty-four hours after cells (10³) were passaged on 96-well plates, in vitro cellular proliferation was evaluated using an IncuCyte ZOOM System (Essen BioScience) every 6 h for 48 h.

In vivo animal models

Female C57BL/6J mice (6–8 weeks old) were purchased from SLC Japan. C57BL/6J-Prkdc<scid>/Rbrc mice (B6 SCID) were provided by RIKEN BRC through the National BioResource Project of the Japan Ministry of Education, Culture, Sports, Science and Technology/Agency for Medical Research and Development. OT-1, *Cd4*^{cre} and *Tfam*^{fl/fl} mice (*Tfam*; mitochondrial transcription factor A) were purchased from the Jackson Laboratory. Rat anti-mouse PD-1 monoclonal antibody (RMPI-14) and anti-mouse CD8β monoclonal antibody (Lyt 3.2) were obtained from Bio X Cell. The control rat IgG2a monoclonal antibody (RTK2758) was obtained from BioLegend.

LLC/P29-MitoDsRed cells (5 × 10⁴) or LLC/A11-MitoDsRed cells (1 × 10⁵) were subcutaneously inoculated into C57BL/6J or B6 SCID mice. To confirm transfer, tumours were collected 21 or 42 days after tumour inoculation to collect the TILs for evaluation. For treatment, the mean values of the long and short diameters were used to generate the tumour growth curves. When the tumour volume reached approximately 100 mm³ on day 14, anti-PD-1 monoclonal antibody (200 μg per mouse) or control monoclonal antibody was intraperitoneally administered 3 times every 3 days. For CD8⁺ T cell depletion, anti-CD8β monoclonal antibody (100 μg per mouse) was intraperitoneally administered 1 day before tumour cell inoculation and then injected every 7 days thereafter. An EV release inhibitor, GW4869 (60 μg per mouse), was injected locally into the tumours once every 2 days. Tumours were collected 42 days after tumour inoculation to collect TILs for evaluation by flow cytometry. In addition, collected TILs were sorted for DsRed⁺ cells and cultured for 7 days, then evaluated by flow cytometry or mtDNA sequencing.

Similarly, we created adoptive T cell transfer models using B6 SCID mice. In brief, sorted CD8⁺ T cells (1 × 10⁷) from splenocytes of C57BL/6J or OT-1 mice were transferred into the SCID mice 7 days after tumour inoculation (LLC/P29-OVA-MitoDsRed, 1 × 10⁵; LLC/A11-OVA-MitoDsRed, 3 × 10⁵). Tumours were collected 28 days after tumour inoculation to collect TILs for evaluation by flow cytometry.

MC-38 (1 × 10⁶) or B16F10-OVA (3 × 10⁵) cells were subcutaneously inoculated into *Tfam*^{fl/fl} mice or *Tfam*^{fl/fl}*Cd4*^{cre} mice, and tumour volume was monitored every 3 days. The means of the long and short diameters were used to generate the tumour growth curves. Anti-PD-1 monoclonal antibody (200 μg per mouse) or control monoclonal antibody was intraperitoneally administered 3 times every 3 days. Tumours were collected 14 days after tumour inoculation to collect TILs for evaluation by flow cytometry. Furthermore, we performed rechallenge mouse experiments. In brief, mice that had shown complete eradication of the initial tumours after anti-PD-1 monoclonal antibody treatment were secondarily challenged with parental tumour cells on day 32.

All mice were maintained under specific pathogen-free conditions at the animal facility of the Institute of Biophysics (Chiba Cancer Center Research Institute and Okayama University). All mouse experiments were approved by the Animal Committee for Animal Experimentation of Chiba Cancer Center and Okayama University, and met the US Public Health Service Policy on Humane Care and Use of Laboratory Animals. When the maximum tumour diameter exceeded 20 mm, mice were killed as a humane end point. The experimental schematics are summarized in Supplementary Fig. 3.

Killing assay

LLC/P29-MitoDsRed cells (1 × 10⁵) or LLC/A11-MitoDsRed cells (2 × 10⁵) were subcutaneously inoculated into OT-1 mice. Forty-two days after tumour inoculation, DsRed⁻ or DsRed⁺CD8⁺ T cells (effector cells)

were sorted from TILs and subsequently cocultured with calcein-AM (Thermo Fisher Scientific)-labelled LLC/P29-OVA or LLC/A11-OVA cells (target cells), respectively, at the indicated effector-to-target cell ratios. LLC/P29 or LLC/A11 cells were used as the controls. After 3 h of incubation, fluorescence was determined using an excitation/emission filter set of 490/535 nm on an ARVO X3 Multilabel reader (PerkinElmer).

Flow cytometry analyses

Flow cytometry was performed as previously described⁷³. In brief, cells were washed with PBS containing 2% FBS and stained with surface antibodies. Intracellular staining was performed with specific antibodies using a FOXP3/Transcription Factor Staining Buffer set (Thermo Fisher Scientific) according to the manufacturer's instructions. For intracellular granzyme B staining in mouse models, cells were stimulated for 5 h with PMA (0.1 mg ml⁻¹) and ionomycin (2 µg ml⁻¹) (Sigma Aldrich). GolgiPlug reagent (1.3 µl ml⁻¹; BD Biosciences) was added during the last 4 h of culture. Samples were assessed using a FACSVerse, FACSLyric or FACSFortessa flow cytometer (BD Biosciences) and FlowJo software (BD Biosciences). Staining antibodies in the flow cytometry analysis were diluted according to the manufacturer's instructions and are summarized in Supplementary Table 6.

Statistical analyses

Patient characteristics were compared between the two groups using Fisher's exact tests. The relationships between continuous variables between and among groups were compared using a *t*-test and one-way ANOVA, respectively. Tumour volume curves were compared using a two-way ANOVA. For multiple testing, Bonferroni correction was used. Progression-free survival and overall survival were defined as the time intervals from the initiation of anti-PD-1 monoclonal antibody therapy until the first observation of disease progression or death from any cause, and until death from any cause, respectively. Survival curves were analysed using the Kaplan–Meier method and compared among groups using the log-rank test. All tests were two-tailed with a predefined significance level of *P* < 0.05. Statistical analyses were performed using GraphPad Prism 9 (GraphPad Software). The means and standard error of the means (error bars) are shown.

Statistics and reproducibility

All *in vitro* experiments were biologically repeated independently three to four times and produced consistent results. All *in vivo* mouse experiments were conducted with four to six mice per group and were repeated at least twice, which also produced consistent results.

Reporting summary

Further information on research design is available in the Nature Portfolio Reporting Summary linked to this article.

Data availability

The data supporting the findings of this study are available from the corresponding authors upon reasonable request. The data of total mtDNA sequencing have been deposited into the Japanese Genotype–phenotype Archive (accession number: JGAS000589). Source data are provided with this paper.

Code availability

Shell and R scripts for variant calling and subsequent mtDNA mutation calls are available from GitHub (https://github.com/jlincbio/mito_somatic_mutect2/tree/v0.3) and Zenodo (<https://doi.org/10.5281/zenodo.12216418>)⁷⁴.

60. Inozume, T. et al. Analysis of the tumor reactivity of tumor-infiltrating lymphocytes in a metastatic melanoma lesion that lost MHC class I expression after anti-PD-1 therapy. *J. Invest. Dermatol.* **139**, 1490–1496 (2019).

61. Cingolani, P. et al. A program for annotating and predicting the effects of single nucleotide polymorphisms, SnpEff: SNPs in the genome of *Drosophila melanogaster* strain w1118; iso-2; iso-3. *Fly* **6**, 80–92 (2012).
62. Kuo, T., Frith, M. C., Sese, J. & Horton, P. EAGLE: explicit alternative genome likelihood evaluator. *BMC Med. Genomics* **11**, 28 (2018).
63. Weissensteiner, H. et al. HaploGrep 2: mitochondrial haplogroup classification in the era of high-throughput sequencing. *Nucleic Acids Res.* **44**, W58–W63 (2016).
64. Akimoto, M., Hayashi, J. I., Nakae, S., Saito, H. & Takenaga, K. Interleukin-33 enhances programmed oncosis of ST2L-positive low-metastatic cells in the tumour microenvironment of lung cancer. *Cell Death Dis.* **7**, e2057 (2016).
65. Takenaga, K., Nakamura, Y. & Sakiyama, S. Expression of antisense RNA to S100A4 gene encoding an S100-related calcium-binding protein suppresses metastatic potential of high-metastatic Lewis lung carcinoma cells. *Oncogene* **14**, 331–337 (1997).
66. Diebold, S. S., Cotten, M., Koch, N. & Zenke, M. MHC class II presentation of endogenously expressed antigens by transfected dendritic cells. *Gene Ther.* **8**, 487–493 (2001).
67. Morgenstern, J. P. & Land, H. Advanced mammalian gene transfer: high titre retroviral vectors with multiple drug selection markers and a complementary helper-free packaging cell line. *Nucleic Acids Res.* **18**, 3587–3596 (1990).
68. Kitay, B. M., McCormack, R., Wang, Y., Tsoulfas, P. & Zhai, R. G. Mislocalization of neuronal mitochondria reveals regulation of Wallerian degeneration and NMNAT/WLD(S)-mediated axon protection independent of axonal mitochondria. *Hum. Mol. Genet.* **22**, 1601–1614 (2013).
69. Dull, T. et al. A third-generation lentivirus vector with a conditional packaging system. *J. Virol.* **72**, 8463–8471 (1998).
70. Théry, C. et al. Minimal information for studies of extracellular vesicles 2018 (MISEV2018): a position statement of the International Society for Extracellular Vesicles and update of the MISEV2014 guidelines. *J. Extracell. Vesicles* **7**, 1535750 (2018).
71. Sanz-Ros, J. et al. Small extracellular vesicles from young adipose-derived stem cells prevent frailty, improve health span, and decrease epigenetic age in old mice. *Sci. Adv.* **8**, eabq2226 (2022).
72. Keeney, J. N., Winters, A. D., Sitcheran, R. & West, A. P. NF-κB-inducing kinase governs the mitochondrial respiratory capacity, differentiation, and inflammatory status of innate immune cells. *J. Immunol.* **210**, 1123–1133 (2023).
73. Kumagai, S. et al. An oncogenic alteration creates a microenvironment that promotes tumor progression by conferring a metabolic advantage to regulatory T cells. *Immunity* **53**, 187–203.e188 (2020).
74. jlincbio. jlincbio/mito_somatic_mutect2: release update (v0.3). Zenodo <https://doi.org/10.5281/zenodo.12216418> (2024).

Acknowledgements We thank H. Nagase, E. Tanji and N. Sakurai for their technical assistance. The graphical abstract in Supplementary Fig. 6 was created using BioRender (<https://biorender.com>). This study was supported by Grants-in-Aid for Scientific Research (Promotion of Joint International Research no. JP23KK0149 (to J.N. and Y.Togashi), B grant no. JP24K02549 (to Y.Togashi) and Challenging Exploratory Research no. JP22K1945904 and no. JP24K22071 (to Y.Togashi)) and a Grant-in-Aid for Research Fellow (grant no. JP22J22286 (to H.I.)) from the Japan Society for the Promotion of Science (JSPS); the Project for Cancer Research and Therapeutic Evolution (P-CREATE, no. JP19cm0106502 (to M.K.), no. JP21cm0106383 (to Y.Togashi), no. JP23ama221325h0001 (to T.Inozume, M.K. and Y.Togashi) and no. JP23ama221427h0001 (to H.H. and Y.Togashi)); Practical Research for Innovative Cancer Control (no. JP22ck0106775h0001 (to J.N.) and no. JP22ck0106723h0001 (to M.K. and Y.Togashi)); the Core Research for Evolutional Science and Technology (CREST, no. JP22gm1810002s0101 to Y.Togashi); Practical Research Project for Rare/Intractable Diseases (no. JP22ek0109495h0002 (to J.L.); and Research Program for Hepatitis (no. JP24fk0210518h0001 (to Y.Togashi)) from the Japan Agency for Medical Research and Development (AMED); the Fusion Oriented Research for disruptive Science and Technology (FOREST, no. JPMJFR2049 (to Y.Togashi)); the ACT-X (no. JPMJAX2321 (to T.Ishino)) from the Japan Science and Technology Agency (JST); the National Cancer Center Research and Development Fund (no. 2023-A-05 (to Y.Togashi)); the Chiba Prefecture Research Grant (to M.K. and Y.Togashi); the Takeda Science Foundation (to Y.Togashi); the Naito Foundation (to Y.Togashi); the Mochida Memorial Foundation (to Y.Togashi); the MSD Life Science Foundation (to Y.Togashi); the GSK Japan foundation (to Y.Togashi); the Research Grant of the Princess Takamatsu Cancer Research Fund (no. 21-25329 (to Y.Togashi)); the Kowa Life Science Foundation (to J.N. and Y.Togashi); the Kato Memorial Bioscience Foundation (to Y.Togashi); the Inamori Foundation (to Y.Togashi); the Astellas Foundation for Research on Metabolic Disorders (to Y.Togashi); the Suzuken Memorial Foundation (to Y.Togashi); the SGH Foundation (to J.N.); the Sumitomo Foundation Grant for Basic Science Research Projects (no. 2300348 (to Y.Togashi)); the Terumo Life Science Foundation (to Y.Togashi); the Chugai Foundation for Innovative Drug Discovery Science (to Y.Togashi); the Ono Pharmaceutical Foundation for Oncology, Immunology, and Neurology (to Y.Togashi); the Kobayashi Foundation for Cancer Research (to M.K. and Y.Togashi); the Taiju Life Social Welfare Foundation (to J.L.); the 2023 Healthcare Innovation Research Grant established with donations from T.Togawa (former president of Kasen Nozzle). Sequencing and bioinformatics analyses were performed on institutional computing resources that included hardware provided by NVIDIA to J.L.

Author contributions Conception and design: Y.Togashi. Development of the methodology: H.I., K.K., T.N., K.T., T.W., T.Ishino, S.A., J.L., Y.Ueda, J.N., Y.S., T.M., M.K. and Y.Togashi. Funding acquisition: H.I., T.Ishino, J.N., J.L., T.Inozume, H.H., M.K. and Y.Togashi. Collection of clinical samples and data: H.I., T.N., T.Inozume, S.K., K.K., S.S., M.I., Yuki Nakamura, A.H.-T., T.Ohnuma, T.K., Y.Umeda, Yasuhiro Nakamura, Y.K., E.I., H.H., J.-i. and T.H. Formal analyses: H.I., K.K., T.N., T.W., T.Ishino, S.A., J.L., H.Makinoshima, Yuki Nakamura and Y.Tatsumi. Writing the original draft: H.I. and Y.Togashi. Writing, reviewing and/or revising the manuscript: H.I., K.K., T.N., K.T., T.Inozume, T.W., T.Ishino, S.A., J.L., S.K., Y.Ueda, J.N., S.S., H.Makinoshima, M.I., Yuki Nakamura, Y.Tatsumi, Y.S., T.M., A.H.-T., T.Ohnuma, T.K., Y.Umeda, Yasuhiro Nakamura, Y.K., E.I., H.H., J.-i., T.H., S.T., H.Manu, T.S., T.Osawa, M.K. and Y.Togashi. Study supervision: J.-i., S.T., H.Manu, T.S. and M.K. All authors read and approved the final manuscript.

Article

Competing interests T. Inozume, received honoraria from Ono Pharmaceutical, Bristol-Myers Squibb and MSD outside this study. S.S. received honoraria from AstraZeneca outside this study. Yasuhiro Nakamura, received honoraria from Ono Pharmaceutical and Novartis Pharma outside this study. E.I. received grants from Janssen Pharmaceutical, Bristol-Myers Squibb, Takeda Pharmaceutical, Pfizer Japan and Ono Pharmaceutical; honoraria from AstraZeneca, Novartis Pharma, Janssen Pharmaceutical, Boehringer Ingelheim, Chugai Pharmaceutical, Eli Lilly Japan and Pfizer Japan outside this study. H.H. received research grants from AstraZeneca, Astellas Pharma, MSD, Ono Pharmaceutical, Nippon Boehringer Ingelheim, Novartis Pharma, Pfizer Japan, Bristol-Myers Squibb, Eli Lilly Japan, Chugai Pharmaceutical, Daiichi Sankyo, Merck Serono, Merck Biopharma, Takeda Pharmaceutical, Taiho Pharmaceutical, SymBio Pharmaceuticals, AbbVie, inVentiv Health Japan, ICON Japan, Gritstone Oncology, Parexel International, Kissei Pharmaceutical, EPS, Syneos Health, Pfizer R&D Japan, A2 Healthcare, Quintiles/IQVIA Services Japan, EP-CRSU, Linical, Eisai, CMIC Shift Zero, Kyowa Hakko Kirin, Bayer Yakuhin, EPS International and Otsuka Pharmaceutical; honoraria from Amgen, AstraZeneca, Boehringer Ingelheim Japan, Bristol-Myers Squibb, Chugai Pharmaceutical, Daiichi Sankyo, Eli Lilly Japan, Janssen Pharmaceutical, Kyorin Pharmaceutical, Merck Biopharma, MSD, Novartis Pharmaceuticals, Ono Pharmaceutical, Taiho Pharmaceutical and Takeda Pharmaceutical; consulting fees from AstraZeneca, Boehringer Ingelheim Japan, Bristol-Myers Squibb, Chugai Pharmaceutical, Eli Lilly Japan, Guardant Health, Pfizer Japan, Shanghai Haihe Biopharma, Takeda Pharmaceutical and Merck Biopharma outside this study. Y. Togashi received research grants from KOTAI Biotechnologies, Daiichi-Sankyo, Ono Pharmaceutical, Bristol-Myers Squibb and KORTUC, and honoraria from Ono Pharmaceutical, Bristol-Myers Squibb, AstraZeneca, Chugai Pharmaceutical and MSD outside this study. All other authors declare that they have no competing financial interests.

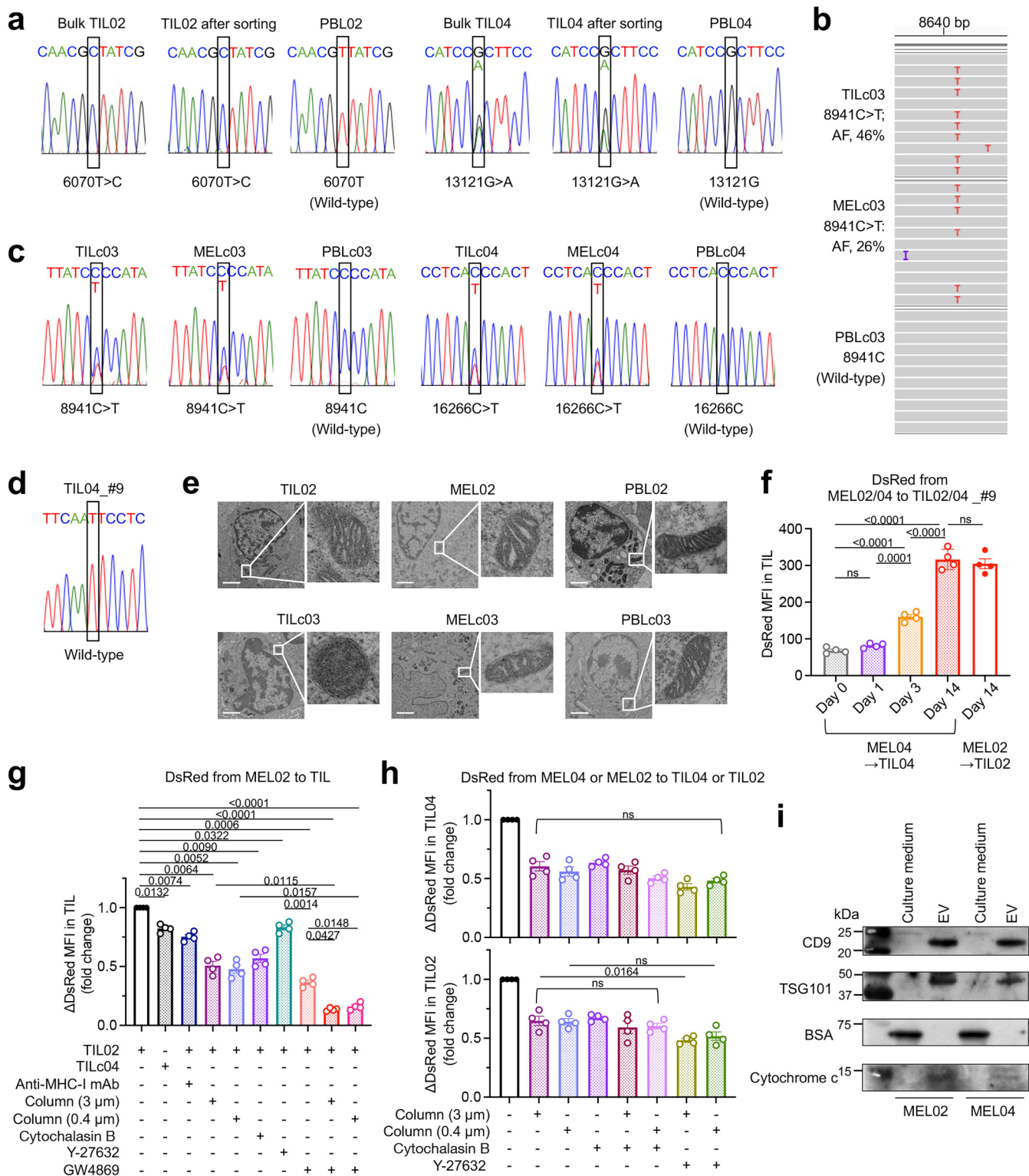
Additional information

Supplementary information The online version contains supplementary material available at <https://doi.org/10.1038/s41586-024-08439-0>.

Correspondence and requests for materials should be addressed to Yosuke Togashi.

Peer review information *Nature* thanks Jonathan Brestoff, Nicola Vannini and the other, anonymous, reviewer(s) for their contribution to the peer review of this work. Peer review reports are available.

Reprints and permissions information is available at <http://www.nature.com/reprints>.

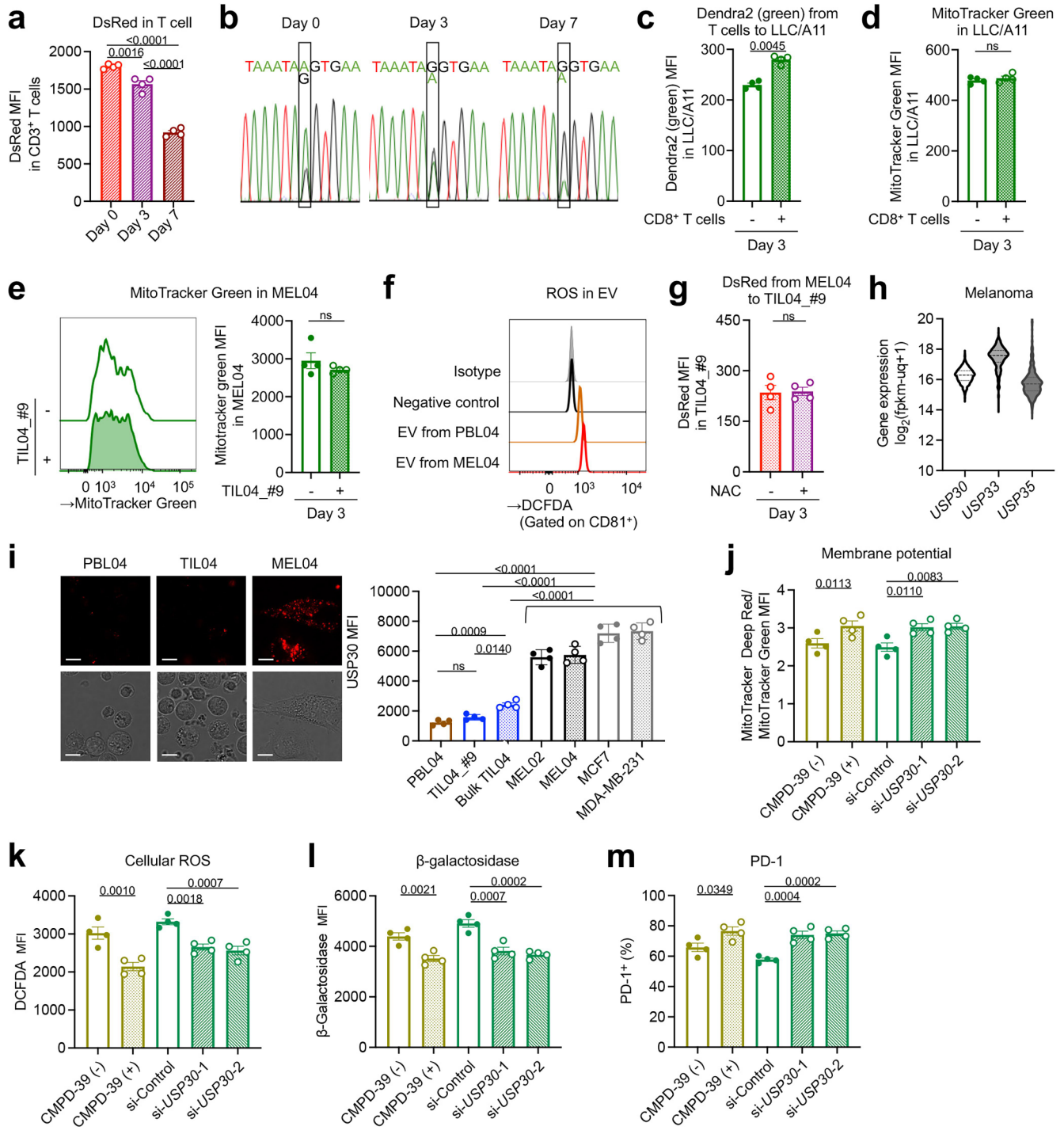


Extended Data Fig. 1 | See next page for caption.

Article

Extended Data Fig. 1 | Additional mtDNA sequencing, mitochondrial transfer, and EV-detection data. **a**, mtDNA sequencing in patients #02 and #04. mtDNA of bulk TILs, sorted CD45⁺CD3⁺ T cells from bulk TILs, and PBLs were sequenced. Representative capillary sequencing chromatograms in patients #2 (left) and #04 (right) are shown. **b**, IGV of TILs and cancer cells. We sequenced the whole mtDNA of paired TILs and cancer cells from the same melanoma patient (#c03) using a next-generation sequencing. PBLs from the same patients were used as germline controls. Track IGV data in patients #c03 are shown. **c**, mtDNA sequencing in patients #c03 and #c04. Paired TILs, cancer cells, and PBLs from the same patient were sequenced. Representative capillary sequencing chromatograms in patients #c03 (left) and #c04 (right) are shown. **d**, mtDNA sequencing of TILO4_#9 cells. A single clones established from TILO4 cells (#9) were sequenced. Representative capillary sequencing chromatogram is shown. **e**, Transmission electronic microscope images in patients #02 and c03. The sections of TILO2 (wild-type), MELO2 (wild-type), PBL02 (wild-type), TILc03 (mutated), MELc03 (mutated), and PBLC03 (wild-type) cells were observed using transmission electron microscopy. Representative images are shown. Scale bar, 2 μ m. **f**, Mitochondrial quantification of TILs transferred from paired cancer cells. TILO2 or TILO4 cells were cocultured with MELO2-MitoDsRed or MELO4-MitoDsRed cells, respectively for 1, 2, 3, or 14 days and then DsRed expression in TILs were analysed using flow cytometry. MFI

summary is shown ($n = 4$ per group). **g**, Mitochondrial quantification of TILs transferred from MELO2 cells under various conditions. Coculture experiments and analyses were performed as described in Fig. 2c. Summary of fold changes of Δ DsRed MFI (DsRed MFI of TILs with coculture – that without coculture) relative to the control conditions (TILO2 and MELO2-MitoDsRed coculture without any drugs or columns) is shown ($n = 4$ per group). **h**, Mitochondrial quantification of TILO4 or TILO2 cells transferred from MELO4 or MELO2 cells under various conditions. Coculture experiments and analyses were performed as described in Fig. 2c. Summaries of fold changes of Δ DsRed MFI (DsRed MFI of TILs with coculture – that without coculture) relative to the control conditions (TIL and MEL-MitoDsRed coculture without any drugs or columns) (top, TILO4 from MELO4; bottom, TILO2 from MELO2) are shown ($n = 4$ per group). **i**, Western blotting for EV-related molecules from three independent experiments. Extracted and purified EVs were used for western blotting experiments following the MISEV2018 guideline. Briefly, culture mediums or EV lysates were subjected to immunoblot analysis with antibodies. We used CD9 (category 1) and TSG101 (category 2) as EV markers. To evaluate purity of FBS containing medium-derived EVs, we checked BSA like category 3. In addition, we evaluated cytochrome as a mitochondrial protein (category 4). For gel source data, see Supplementary Fig. 1. One-way ANOVA with Bonferroni correction were used in (f)-(h).

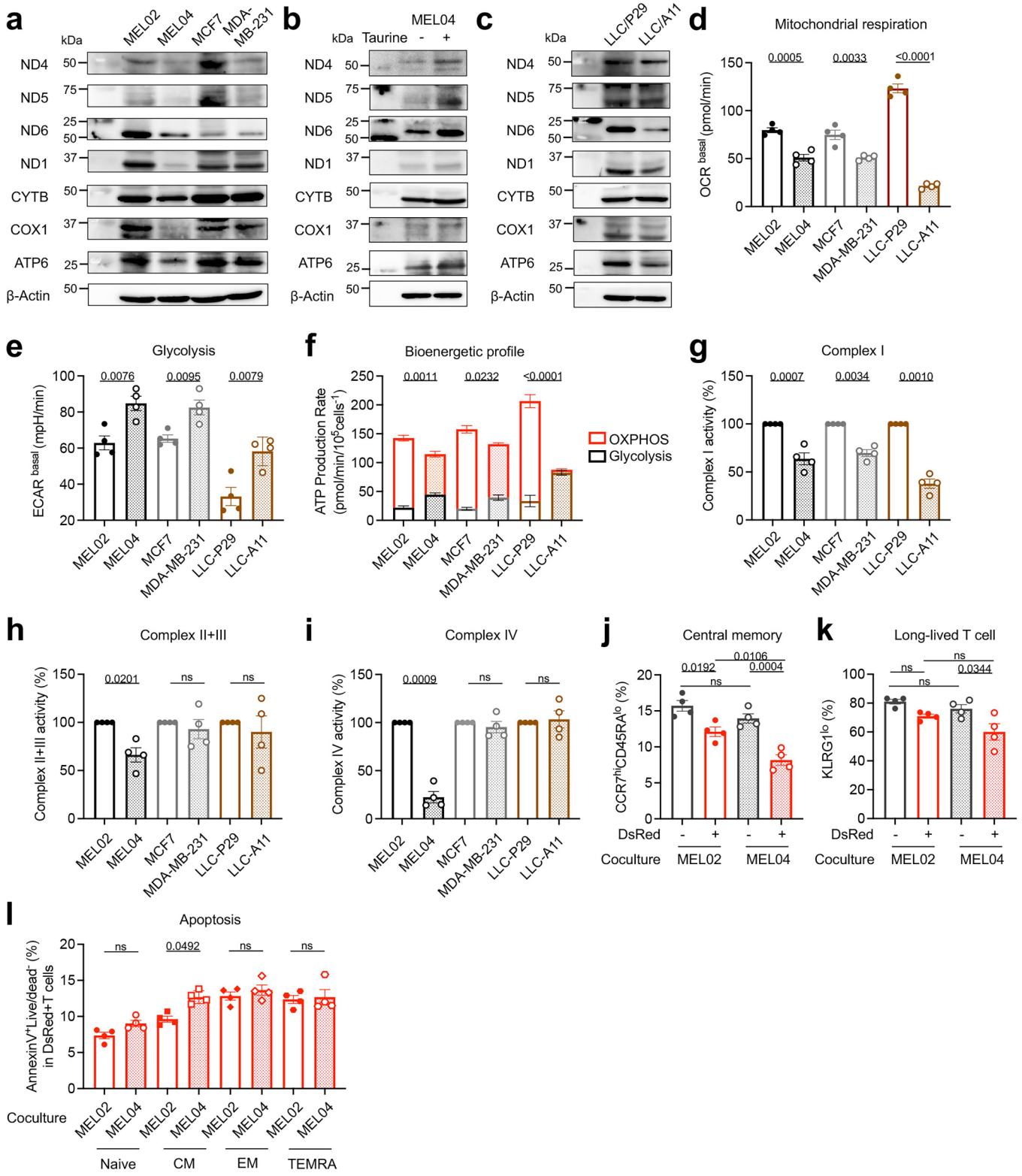


Extended Data Fig. 2 | See next page for caption.

Article

Extended Data Fig. 2 | Additional homoplasmy replacement data. **a** and **b**, DsRed expression and mtDNA mutations in sorted T cells from mouse TILs in vitro. We sorted mitochondria-transferred DsRed⁺ T cells from LLC/A11-MitoDsRed tumours as described in Supplementary Fig. 3, which were subsequently cultured further in vitro for 7 days. We analysed DsRed expression and mtDNA in bulk T cells at each time point and summary of DsRed expression (**a**) and representative capillary sequencing chromatograms (**b**) are shown. **c**, Mitochondrial quantification of LLC/A11 cells transferred from mouse T cells. OVA-overexpressing LLC/A11 cells were cocultured with or without CD8⁺ T cells from *PhaM*^{excised} OT-I mice for 3 days. Then, Dendra2 (green) expression in OVA-overexpressing LLC/A11 cells were analysed using flow cytometry. MFI summary is shown ($n = 4$ per group). **d** and **e**, Original mitochondrial quantification of LLC/A11 (**d**) and MELO4 (**e**) cells after coculture with mouse T cells and TIL04_#9 cells, respectively. MitoTracker Green-labelled OVA-overexpressing LLC/A11 or MELO4 cells were cocultured with or without CD8⁺ T cells from OT-I mice or TIL04_#9 cells for 3 days, respectively. Then, OVA-overexpressing LLC/A11 or MELO4 cells were subsequently analysed using flow cytometry. Representative flow cytometric staining (**e**, left) and MFI summaries (**d** and **e**, right) are shown ($n = 4$ per group). **f**, ROS in EVs. After staining with DCFDA, EVs were extracted and purified from the supernatants, from which EV-conjugated beads were

created. The beads were analysed using flow cytometry. EV-free medium without any cells was used as a negative control. Representative flow cytometric staining is shown. **g**, Mitochondrial quantification of TIL04_#9 cells transferred from MELO4 cells with NAC. TIL04_#9 cells were cocultured with MELO4-MitoDsRed cells and/or NAC for 3 days and then DsRed expression in TILs were analysed using flow cytometry. MFI summary is shown ($n = 4$ per group). **h**, Gene expression of USP30, USP33, and USP35 from TCGA datasets in patients with melanoma. **i**, USP30 expression. Cells were stained with AF546-conjugated anti-USP30 mAb and analysed using a confocal laser microscope or flow cytometry. Representative confocal microscopic images (left) and MFI summary (right) are shown ($n = 4$ per group). Scale bar, 10 μ m. **j-m**, Membrane potential evaluated by MitoTracker Deep Red and Green (**j**), cellular ROS production evaluated by DCFDA (**k**), β -galactosidase activity (**l**), and PD-1 expression (**m**) in TILs treated with a USP30 inhibitor (CMPD-39) or siRNAs for USP30. TIL04_#9 cells were cocultured with MELO4 cells with or without CMPD-39 or siRNA transfection for 14 days and then analysed using flow cytometry. To analyse PD-1 expression, TILs were stimulated with anti-CD3 and anti-CD28 mAbs. Summaries are shown ($n = 4$ per group). Two-sided t-tests were used in (c)-(e), and (g) and one-way ANOVA with Bonferroni correction were used in (a) and (i)-(m).

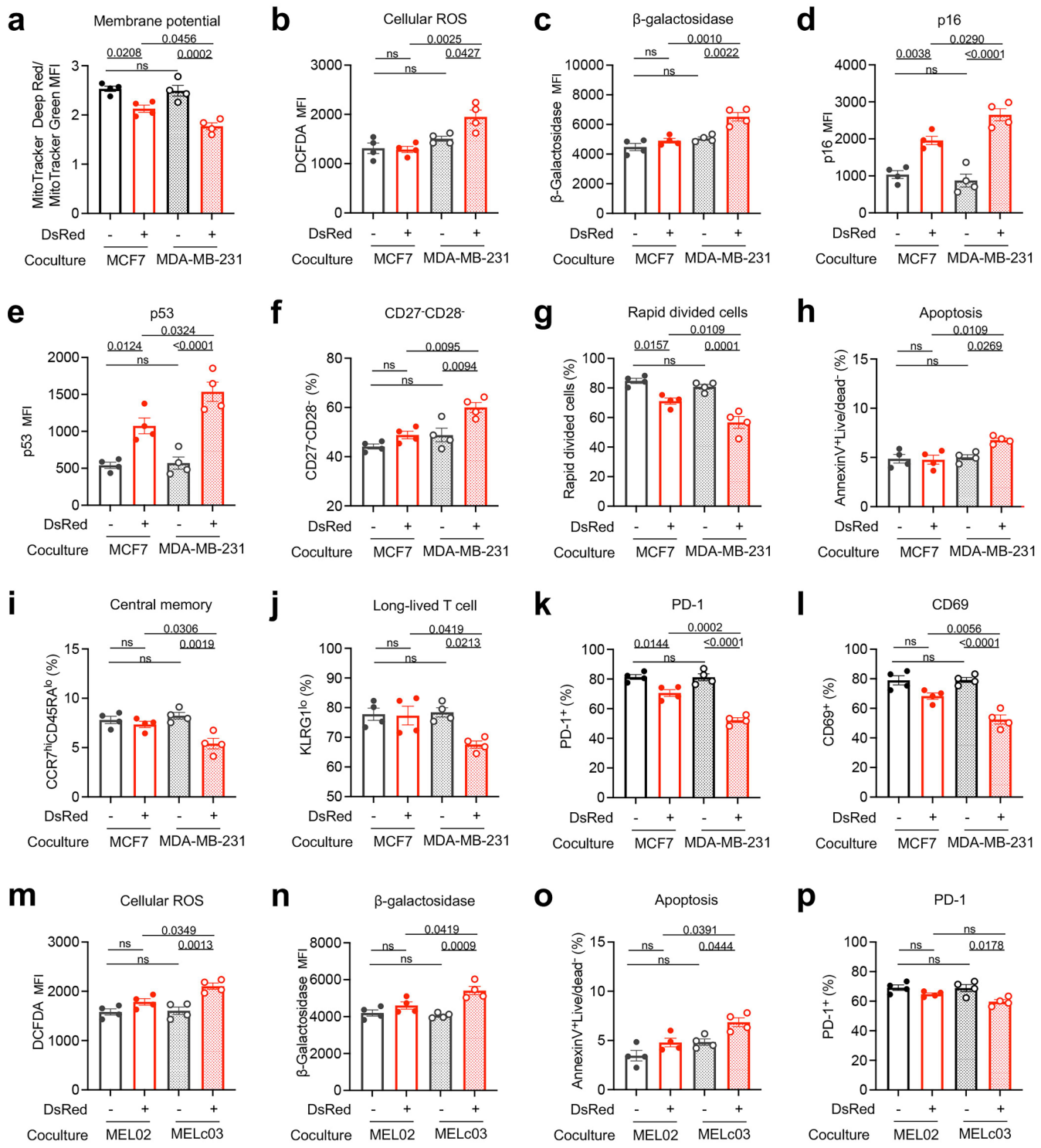


Extended Data Fig. 3 | See next page for caption.

Article

Extended Data Fig. 3 | Additional in vitro cell line and PBL data. **a-c**, Western blotting for mitochondrial proteins from three independent experiments (human cell lines, **a** and **b**; mouse cell lines, **c**). Cell lysates were subjected to immunoblot analysis with antibodies to mitochondrial proteins (ND4, ND5, ND6, NDI, CYTB, COX1, and ATP6). MELO4 cells were treated with taurine before extraction in **b**. β -actin was used as a loading control. For gel source data, see Supplementary Fig. 1. **d-f**, Metabolic evaluation using a flux analyser. The oxygen consumption rate (OCR; **d**) and extracellular acidification rate (ECAR; **e**) were measured under basal conditions, and the bioenergetic profile captured the major ATP-producing pathways of each cell line by calculating the ATP production rate (**f**). Summaries are shown ($n = 4$ per group). **g-i**, Electron transport chain activity assays. We used activity buffer with the isolated mitochondrial protein in place of the supplied mitochondria in the MitoCheck Activity Assay Kits, following the manufacturer's instructions. Reactions were conducted at 25 °C using a microplate reader with readings taken every 30 s for 15 min and the absorbance changes from the base line were evaluated.

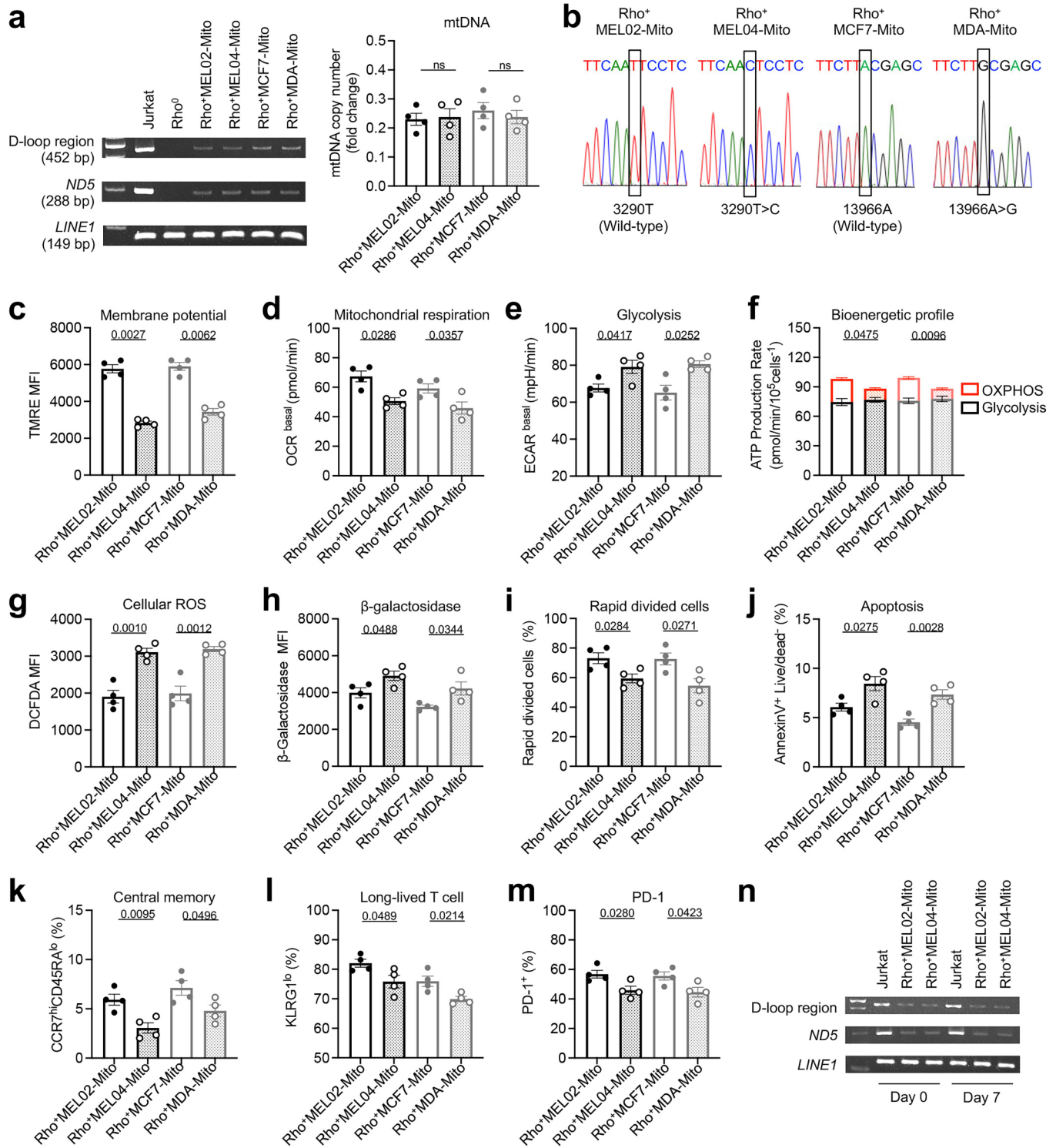
Summaries of fold changes to wild-type cells (**g**, complex I; **h**, II + III; **i**, IV) are shown ($n = 4$ per group). **j** and **k**, Frequencies of CCR7^{hi}CD45RA^{lo} central memory (**j**) and KLRG1^{lo} long-lived (**k**) fractions in PBLs. Sorted CCR7^{hi}CD45RA^{hi}CD8⁺ naïve T cells from PBLs of healthy donors were cocultured with MELO2-MitoDsRed or MELO4-MitoDsRed cells for 7 days while being stimulated with anti-CD3 mAb in the presence of IL-7, IL-15, and IL-2. Subsequently, PBLs were analysed using flow cytometry. Summaries are shown ($n = 4$ per group). **l**, Apoptosis evaluated by Annexin V in each T cell fraction. Each CD8⁺ T cell fraction (naïve, CCR7^{hi}CD45RA^{hi}; central memory [CM], CCR7^{hi}CD45RA^{lo}; effector memory [EM], CCR7^{lo}CD45RA^{lo}; terminally differentiated effector memory [TEMRA], CCR7^{lo}CD45RA^{hi}) sorted from PBLs of healthy donors was cocultured with MELO2-MitoDsRed or MELO4-MitoDsRed cells for 4 days, and apoptosis in DsRed⁺CD8⁺ T cells was analysed using flow cytometry. Summary is shown ($n = 4$ per group). Two-sided t-tests were used in (d)-(i) and (l) and one-way ANOVA with Bonferroni correction were used in (j)-(k).



Extended Data Fig. 4 | Additional in vitro mitochondria transferred TIL data. We established DsRed⁺TIL04#9/MCF7 (wild-type), DsRed⁺TIL04#9/MCF7 (wild-type), DsRed⁺TIL04#9/MDA (wild-type), DsRed⁺TIL04#9/MDA (mutated), DsRed⁺TILc03#5/02 (wild-type), DsRed⁺TILc03#5/02 (wild-type), DsRed⁺TILc03#5/c03 (wild-type), DsRed⁺TILc03#5/c03 cells (mutated), as described in Supplementary Fig. 4. **a-l**, Membrane potential evaluated by MitoTracker Deep Red and Green (**a**), cellular ROS production evaluated by DCFDA (**b**), β -galactosidase activity (**c**), p16 (**d**) and p53 (**e**) expression, frequency of CD27⁻CD28⁻ senescent fraction (**f**), rapidly dividing cells evaluated by CFSE dilution (**g**), apoptosis evaluated by Annexin V (**h**), frequencies of CCR7^{hi}CD45RA^{lo} central memory (**i**) and KLRG1^{lo} long-lived (**j**)

fractions, and PD-1 (**k**) and CD69 (**l**) expression in TIL04 #9 cells. To analyse cell division, PD-1, and CD69 expression, TILs were stimulated with anti-CD3 and anti-CD28 mAbs. Rapidly dividing cells were counted after the third division on day 3. TILs were analysed using flow cytometry, and summaries are shown ($n = 4$ per group). **m-p**, Cellular ROS production evaluated by DCFDA (**m**), β -galactosidase activity (**n**), apoptosis evaluated by Annexin V (**o**), and PD-1 expression (**p**) in TILc03_#5 cells. To analyse PD-1 expression, TILs were stimulated with anti-CD3 and anti-CD28 mAbs. TILs were analysed using flow cytometry, and summaries are shown ($n = 4$ per group). One-way ANOVA with Bonferroni correction were used in (a)-(p).

Article

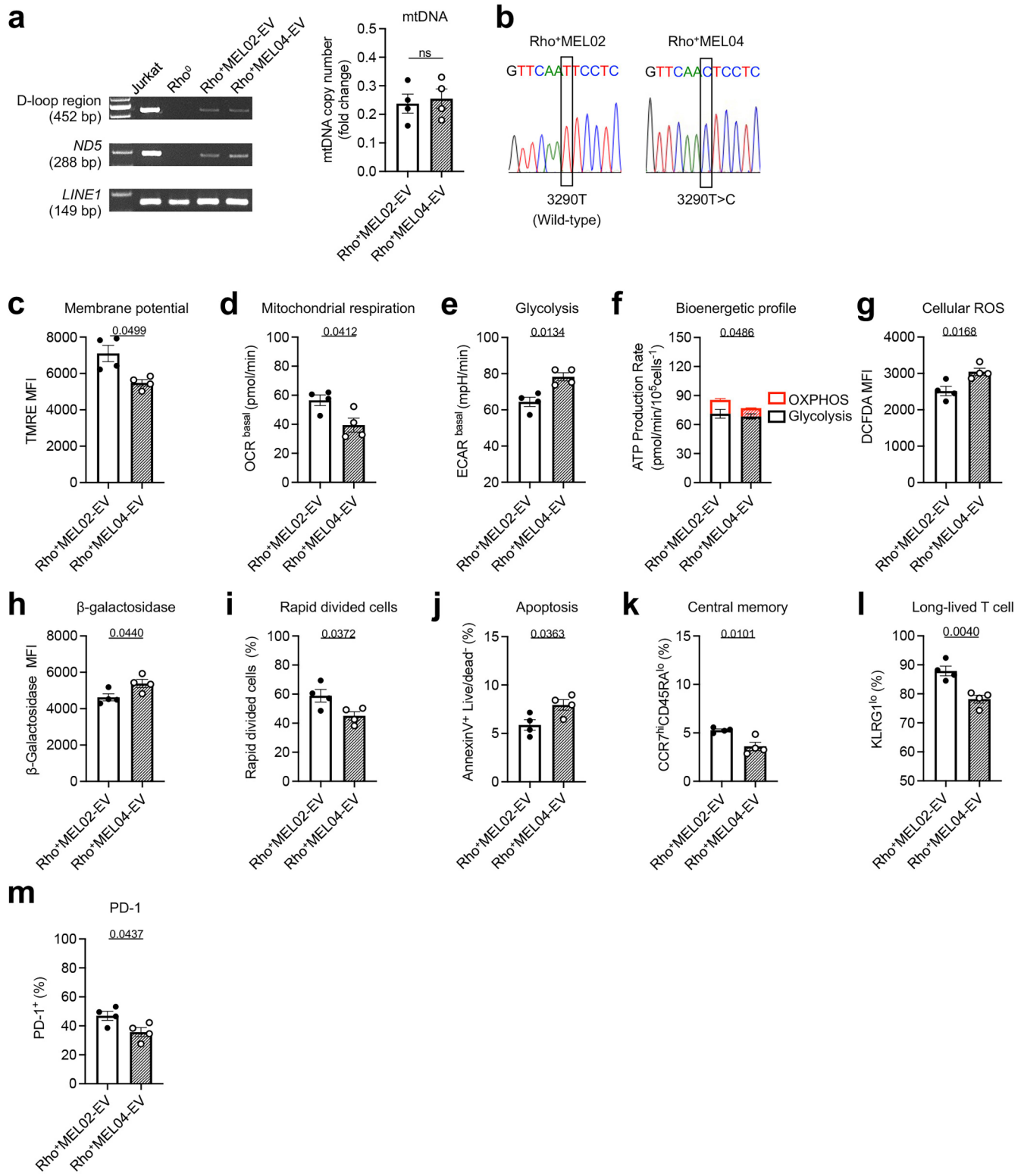


Extended Data Fig. 5 | See next page for caption.

Extended Data Fig. 5 | In vitro mitochondria-transferred Jurkat cell data using a MitoCeption protocol. We established mtDNA-deficient Jurkat/Rho⁰, Rho⁺MEL02-Mito (wild-type), Rho⁺MEL04-Mito (mutated), Rho⁺MCF7-Mito (wild-type), and Rho⁺MDA-Mito cells (mutated), as described in Supplementary Fig. 4. **a**, mtDNA amounts and the quantification in Jurkat cells. DNA from parental Jurkat, Jurkat/Rho⁰, Rho⁺MEL02-Mito, Rho⁺MEL04-Mito, Rho⁺MCF7-Mito, and Rho⁺MDA-Mito cells were extracted and amplified by PCR using primers specific for the D-loop region and *NDS*. *LINE1* was used as an internal control for nuclear DNA. The quantification was performed by real-time PCR and the fold changes to parental Jurkat cells were calculated. The representative PCR bands (left) and summary of the fold changes (right) are shown ($n = 4$ per group). For gel source data, see Supplementary Fig. 1. **b**, mtDNA sequencing of the established Jurkat cells. Representative capillary sequencing chromatograms are shown. **c**, Membrane potential of Jurkat cells. The Jurkat cells were analysed using flow cytometry with TMRE, and MFI summary is shown ($n = 4$ per group). **d-f**, Metabolic evaluation of the established Jurkat cells using a flux analyser. The oxygen consumption rate (OCR; **d**) and extracellular acidification rate (ECAR; **e**) were measured under basal conditions,

and the bioenergetic profile captured the major ATP-producing pathways of each Jurkat cell line by calculating the ATP production rate (**f**). Summaries are shown ($n = 4$ per group). **g-m**, Cellular ROS production evaluated by DCFDA (**g**), β -galactosidase activity (**h**), rapidly dividing cells evaluated by CFSE dilution (**i**), apoptosis evaluated by Annexin V (**j**), frequencies of CCR7^{hi}CD45RA^{lo} central memory (**k**) and KLRC1^{lo} long-lived (**l**) fractions, and PD-1 expression (**m**) in the established Jurkat cells. To analyse cell division and PD-1 expression, Jurkat cells were stimulated with anti-CD3 and anti-CD28 mAbs. Rapidly dividing cells were counted after the third division on day 3. The Jurkat cells were analysed using flow cytometry, and summaries are shown ($n = 4$ per group). **n**, mtDNA amounts in the Rho⁺ cells during the culture. Rho⁺MEL02-Mito and Rho⁺MEL04-Mito cells were cultured in normal medium without sodium pyruvate and uridine. DNA from the cells was extracted at each time point and amplified by PCR using primers specific for the D-loop region and *NDS*. *LINE1* was used as an internal control for nuclear DNA. The representative PCR bands are shown. For gel source data, see Supplementary Fig. 1. Two-sided t-tests were used in (a) and (c)-(m) for statistical analyses.

Article

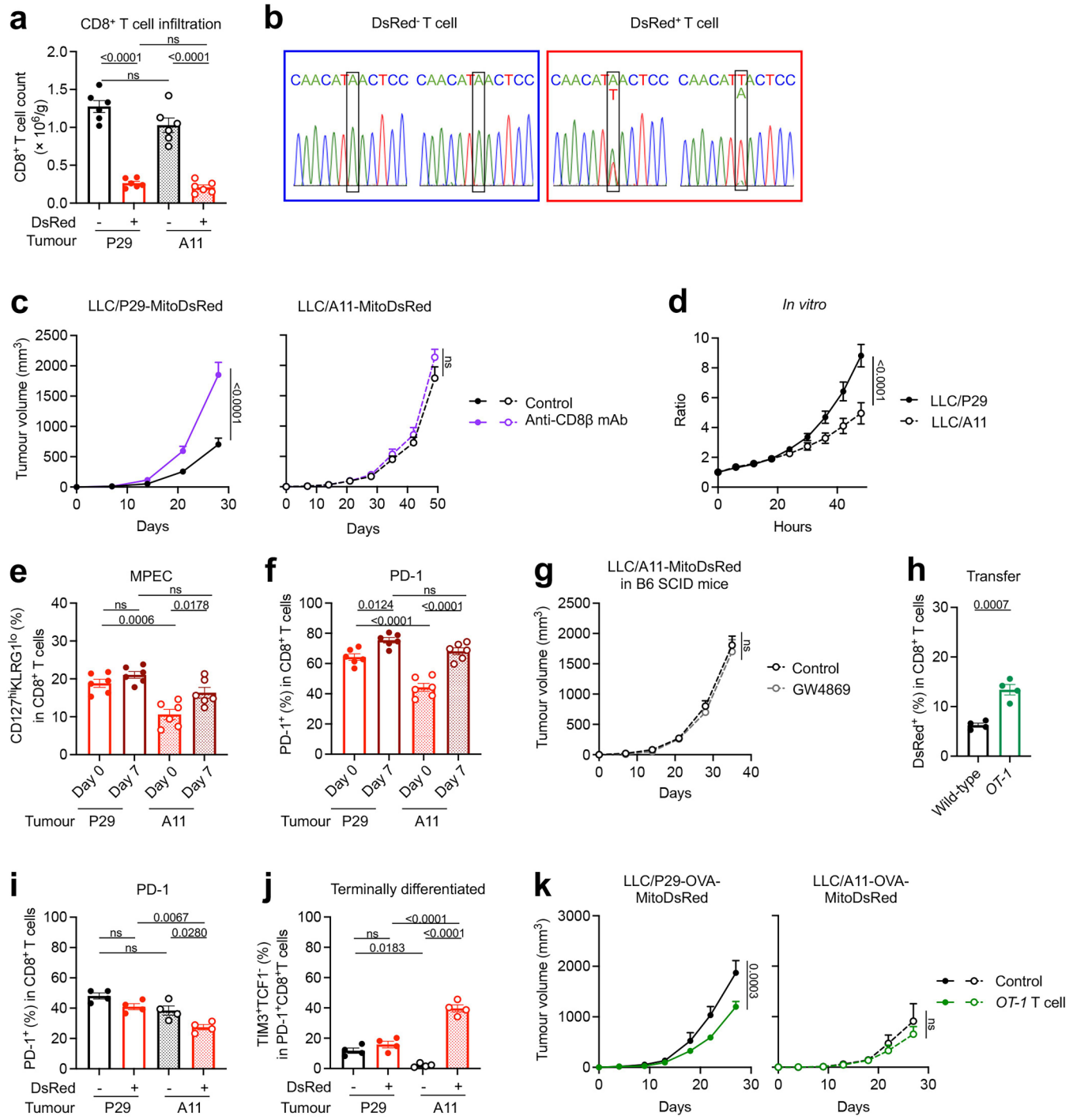


Extended Data Fig. 6 | See next page for caption.

Extended Data Fig. 6 | In vitro mitochondria-transferred Jurkat cell data using an EV protocol. We established mtDNA-deficient Jurkat/Rho⁰, Rho⁺MEL02-EV (wild-type), and Rho⁺MEL04-EV cells (mutated), as described in Supplementary Fig. 4. **a**, mtDNA amounts and the quantification in Jurkat cells. DNA from parental Jurkat, mtDNA-deficient Jurkat/Rho⁰, Rho⁺MEL02-EV, and Rho⁺MEL04-EV cells was extracted and amplified by PCR using primers specific for the D-loop region and *ND5*. *LINE1* was used as an internal control for nuclear DNA. The quantification was performed by real-time PCR and the fold changes to parental Jurkat cells were calculated. The representative PCR bands (left) and summary of the fold changes (right) are shown (n = 4 per group). **b**, mtDNA sequencing of Jurkat cells. The mtDNA of Rho⁺MEL02-EV and Rho⁺MEL04-EV cells was sequenced. Representative capillary sequencing chromatograms are shown. **c**, Membrane potential of Jurkat cells. Rho⁺MEL02-EV and Rho⁺MEL04-EV cells were analysed using flow cytometry with TMRE. MFI summary is shown

(n = 4 per group). **d-f**, Metabolic evaluation of Jurkat cells using a flux analyser. The OCR (**d**) and ECAR (**e**) were measured under basal conditions, and the bioenergetic profile captured the major ATP-producing pathways of Jurkat cells by calculating the ATP production rate (**f**). Summaries are shown (n = 4 per group). **g-m**, Cellular ROS production evaluated by DCFDA (**g**), β-galactosidase activity (**h**), rapidly dividing cells evaluated by CFSE dilution (**i**), apoptosis evaluated by Annexin V (**j**), frequencies of CCR7^{hi}CD45RA^{lo} central memory (**k**) and KLRG1^{lo} long-lived (**l**) fractions, and PD-1 expression (**m**) in Jurkat cells. To analyse cell division and PD-1 expression, the Jurkat cells were stimulated with anti-CD3 and anti-CD28 mAbs. Rapidly dividing cells were counted after the third division on day 3. The Jurkat cells were analysed using flow cytometry, and summaries are shown (n = 4 per group). Two-sided t-tests were used in (a) and (c)-(m).

Article

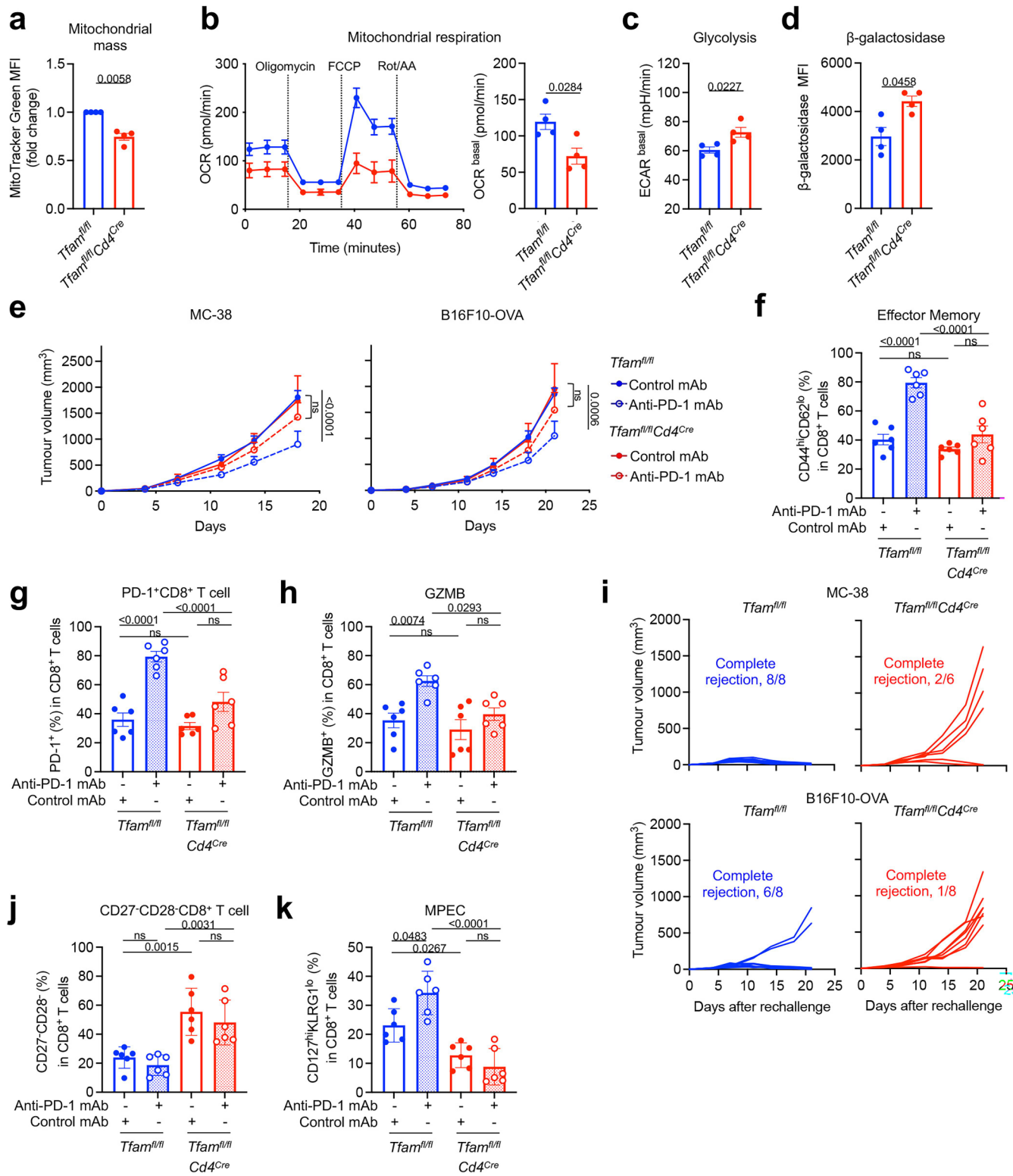


Extended Data Fig. 7 | See next page for caption.

Extended Data Fig. 7 | Additional in vivo mouse transfer data. **a**, CD8⁺ T cell infiltration. In vivo experiments were performed as described in Supplementary Fig. 3. Summary of CD8⁺ T cell counts per weight is shown (n = 6 per group). **b**, mtDNA sequencing in TILs. In vivo experiments were performed as described in Supplementary Fig. 3. Representative capillary sequencing chromatograms for DsRed⁻ (left, blue frame) or DsRed⁺ T cells (right, red frame) are shown. **c**, Tumour growth (left, LLC/P29; right, LLC/A11) in CD8⁺ T-cell depleted mice. In vivo experiments were performed as described in Supplementary Fig. 3, and anti-CD8 β mAb was administered intraperitoneally 1 day before tumour cell inoculation and then injected every 7 days (n = 6 per group). **d**, In vitro cellular proliferation. Cellular proliferation was evaluated every 6 h for 48 h. The ratios to the base line are shown (n = 4 per group). **e** and **f**, Frequency of CD127^{hi}KLRG1^{lo} MPECs (**e**) and PD-1 expression (**f**) in sorted T cells from mouse TILs in vitro. We sorted mitochondria-transferred DsRed⁺ T cells from LLC/P29-MitoDsRed or LLC/A11-MitoDsRed tumours, which were subsequently cultured further in vitro for 7 days. To analyse PD-1 expression, T cells were stimulated with anti-CD3 and anti-CD28 mAbs. Sorted bulk CD8⁺ T cells were analysed using flow cytometry

and summaries are shown (n = 6 per group). **g**, Tumour growth in B6 SCID mice treated with an EV release inhibitor (GW4869). In vivo experiments were performed as described in Supplementary Fig. 3 (n = 6 per group). **h**, DsRed expression in adoptive transferred tumour-infiltrating CD8⁺ T cells. In vivo experiments were performed as described in Supplementary Fig. 3. Summary is shown (n = 4 per group). **i**, PD-1 expression in adoptive transferred CD8⁺ TILs from LLC/P29-OVA-MitoDsRed or LLC/A11-OVA-MitoDsRed tumours according to DsRed expression. In vivo experiments were performed as described in Supplementary Fig. 3 using *OT-I* mice. Summaries are shown (n = 4 per group). **j**, Frequency of TIM3⁺TCF1⁻ terminally differentiated exhausted CD8⁺ T cells in adoptive transferred PD-1⁺CD8⁺ TILs from LLC/P29-OVA-MitoDsRed or LLC/A11-OVA-MitoDsRed tumours according to DsRed expression. In vivo experiments were performed as described in Supplementary Fig. 3 using *OT-I* mice. Summary is shown (n = 4 per group). **k**, Tumour growth (left, LLC/P29; right, LLC/A11) in the adoptive T-cell transfer models. In vivo experiments were performed as described in Supplementary Fig. 3 using *OT-I* mice.

Article

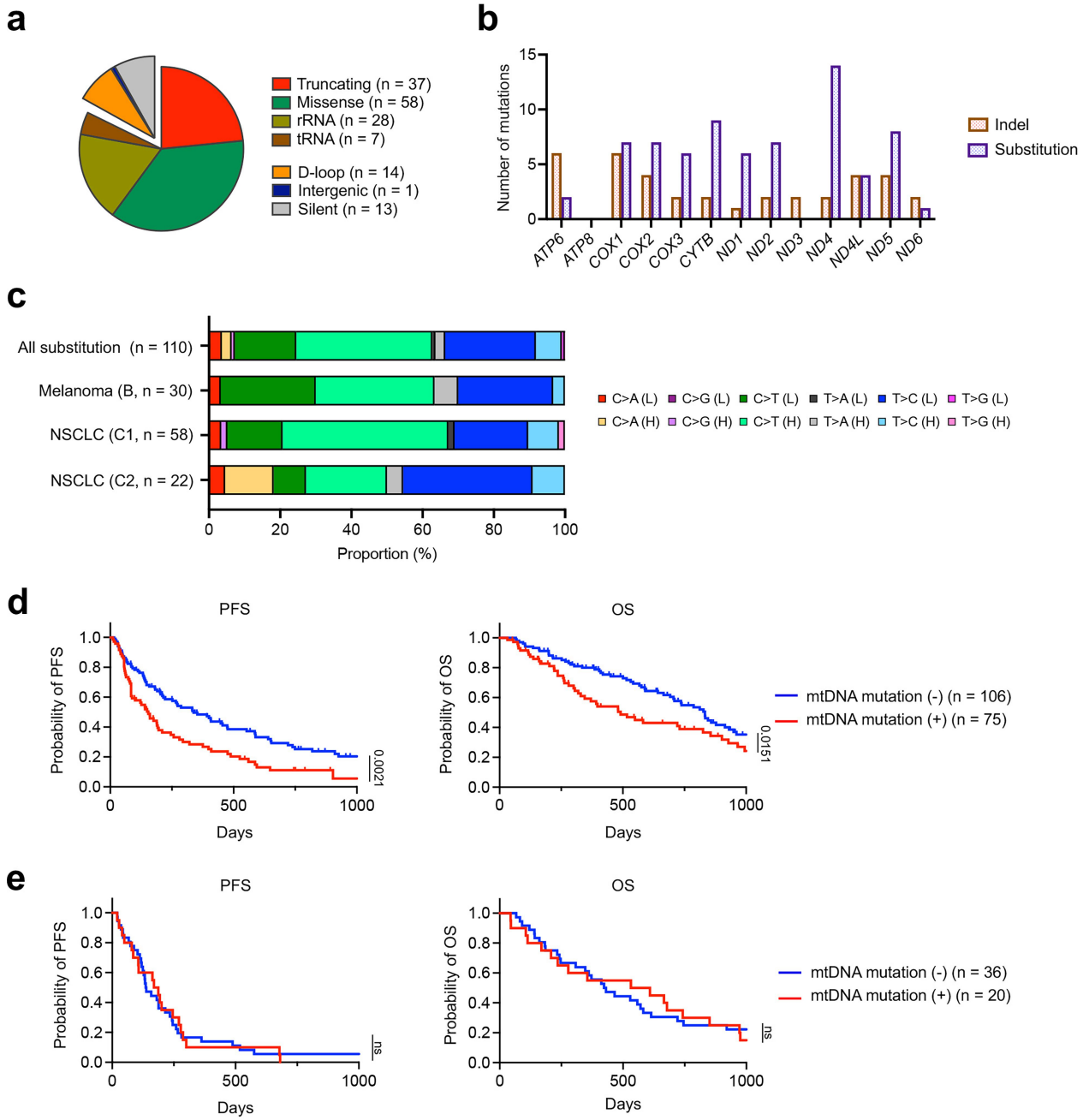


Extended Data Fig. 8 | In vivo mouse mitochondrial dysfunction data.

a, Mitochondrial mass. MitoTracker Green-labelled T cells from splenocytes in *Tfam*^{fl/fl} and *Tfam*^{fl/fl}*Cd4Cre* mice were analysed using flow cytometry. Summary of fold changes to *Tfam*^{fl/fl} mice is shown ($n = 4$ per group). **b** and **c**, Metabolic evaluation. T cells from splenocytes in *Tfam*^{fl/fl} and *Tfam*^{fl/fl}*Cd4Cre* mice were analysed using a flux analyser. The OCR (b, left) and ECAR (c) were measured under basal conditions. The OCR trace (b, left) and summaries (b, right; c) are shown ($n = 4$ per group). **d**, β -galactosidase activity. T cells from splenocytes in *Tfam*^{fl/fl} and *Tfam*^{fl/fl}*Cd4Cre* mice were analysed using flow cytometry. MFI summary is shown ($n = 4$ per group). **e**, MC-38 (left) or B16-OVA (right) tumour growth treated with anti-PD-1 or control mAb in *Tfam*^{fl/fl} or *Tfam*^{fl/fl}*Cd4Cre* mice. In vivo experiments were performed as described in Supplementary Fig. 3 (MC-38, $n = 6$ per group; B16-OVA, 4 per group). **f-h**, Frequencies of CD44^{hi}CD62L^{lo}CD8⁺ effector memory T cells (f), PD-1⁺CD8⁺ T cells (g), and granzyme B (GZMB)-producing CD8⁺ T cells (h) in TILs. In vivo experiments were performed as described in Supplementary Fig. 3. Summaries are shown ($n = 6$ per group).

i, Rechallenged tumour growth. In vivo experiments were performed as described in Supplementary Fig. 3. Each tumour volume (MC-38, top; B16-OVA, bottom) is shown. **j** and **k**, Frequencies of CD27^{hi}CD28^{hi}CD8⁺ senescent T cells (j) and CD127^{hi}KLRG-1^{lo}CD8⁺ MPECs (k) in TILs. In vivo experiments were performed as described in Supplementary Fig. 3. Summaries are shown ($n = 6$ per group).

experiments were performed as described in Supplementary Fig. 3 (MC-38, $n = 6$ per group; B16-OVA, 4 per group). **f-h**, Frequencies of CD44^{hi}CD62L^{lo}CD8⁺ effector memory T cells (f), PD-1⁺CD8⁺ T cells (g), and granzyme B (GZMB)-producing CD8⁺ T cells (h) in TILs. In vivo experiments were performed as described in Supplementary Fig. 3. Summaries are shown ($n = 6$ per group).



Extended Data Fig. 9 | mtDNA mutations in tumour tissues impaired efficacy of PD-1 blockade. **a-c.** The proportion of total 158 mtDNA variants (a), number and type of mtDNA variants (b), and 110 mtDNA variant spectra for substitutions on the light (L) or heavy (H) strand (c) in cohorts B and C1/2. Whole mtDNA sequencing for FFPE tumour tissues was conducted with a next-generation sequencing. **d and e.** Survival curves of patients who received PD-1 blockade therapy (d, melanoma, 95; NSCLC, 86) and those with NSCLC who received platinum-doublet chemotherapies without any ICIs as first-line

therapy (n = 56) according to mtDNA status. mtDNA mutations were defined as truncating and missense, and tRNA/rRNA variants. PFS (left) and OS (right) were defined as the time intervals from the initiation of treatment until the first observation of disease progression or death from any cause, and until death from any cause, respectively. Survival curves were analysed using the Kaplan-Meier method and compared among groups using the two-sided log-rank test in (d) and (e).

Article

Extended Data Table 1 | Characteristics of patients for mtDNA sequencing from FFPE samples

| Features | Cohort B (melanoma) | | | Cohort C1 (NSCLC) | | |
|---|----------------------|----------------------|---------|----------------------|----------------------|--------|
| | mtDNA mutation | | P | mtDNA mutation | | |
| | Negative (n = 64) | Positive (n = 31) | | Negative (n = 42) | Positive (n = 44) | |
| Age, years [median] (range) | 67 (21–89) | 71 (25–87) | 0.200 | 70 (29–93) | 73 (43–86) | 0.215 |
| Sex (male/female) | 33/31 | 20/11 | 0.275 | 37/5 | 33/11 | 0.167 |
| PS (0 or 1/2 or 3) | 63/1 | 29/2 | 0.248 | 34/8 | 40/4 | 0.223 |
| Type (acral or mucosal/others) | 34/30 | 14/17 | 0.516 | | | |
| Primary site (the head, neck or dorsal surfaces of the distal extremities/others) | 5/59 | 8/23 | 0.025 | | | |
| Histology (ad/sq/others/NE ¶) | | | | 29/11/0/2 | 24/13/1/6 | 0.623 |
| Smoking status (pack years \geq 40/< 40) | | | | 30/12 | 25/19 | 0.183 |
| Driver mutation ¶¶ (yes/no/NE) | 16/42/6 | 8/19/4 | > 0.999 | 1/41/0 | 4/40/0 | 0.361 |
| ICI (anti-PD-1 mAb monotherapy/anti-CTLA-4 mAb monotherapy/anti-PD-1 and CTLA-4 mAbs/others ¶¶¶) | 53/2/9/0 | 27/1/3/0 | 0.745 | 42/0/0/0 | 44/0/0/0 | >0.999 |
| PD-L1 status (\geq 50%/ $<$ 50%) | | | | 39/3 | 40/4 | >0.999 |
| Previous systemic therapy (yes/no) | 8/56 | 4/27 | > 0.999 | 3/39 | 7/37 | 0.315 |
| Best response (CR/PR/SD/PD/NE ¶¶¶¶) | 5/15/19/23/2 | 1/10/5/12/3 | 0.645 | 2/15/13/9/3 | 2/20/13/6/3 | 0.398 |

NSCLC, non-small-cell lung cancer; PS, Eastern Cooperative Oncology Group Performance Status; NE, not evaluated. Ad, adenocarcinoma; sq, squamous cell carcinoma. ¶ad vs. sq; ¶¶Driver mutation, BRAF mutation in cohort B and EGFR, ALK, ROS1, BRAF, MET exon 14 skipping, or KRAS mutation in cohorts C1 and C2; ¶¶¶¶anti-PD-1 mAb or anti-CTLA-4 mAb vs. anti-PD-1 and CTLA-4 mAbs in cohort B; ¶¶¶¶¶CR or PR or SD vs. PD. The relationships between groups were compared using Fisher's exact tests or two-sided t-tests.

Reporting Summary

Nature Portfolio wishes to improve the reproducibility of the work that we publish. This form provides structure for consistency and transparency in reporting. For further information on Nature Portfolio policies, see our [Editorial Policies](#) and the [Editorial Policy Checklist](#).

Statistics

For all statistical analyses, confirm that the following items are present in the figure legend, table legend, main text, or Methods section.

n/a Confirmed

- The exact sample size (n) for each experimental group/condition, given as a discrete number and unit of measurement
- A statement on whether measurements were taken from distinct samples or whether the same sample was measured repeatedly
- The statistical test(s) used AND whether they are one- or two-sided
Only common tests should be described solely by name; describe more complex techniques in the Methods section.
- A description of all covariates tested
- A description of any assumptions or corrections, such as tests of normality and adjustment for multiple comparisons
- A full description of the statistical parameters including central tendency (e.g. means) or other basic estimates (e.g. regression coefficient) AND variation (e.g. standard deviation) or associated estimates of uncertainty (e.g. confidence intervals)
- For null hypothesis testing, the test statistic (e.g. F , t , r) with confidence intervals, effect sizes, degrees of freedom and P value noted
Give P values as exact values whenever suitable.
- For Bayesian analysis, information on the choice of priors and Markov chain Monte Carlo settings
- For hierarchical and complex designs, identification of the appropriate level for tests and full reporting of outcomes
- Estimates of effect sizes (e.g. Cohen's d , Pearson's r), indicating how they were calculated

Our web collection on [statistics for biologists](#) contains articles on many of the points above.

Software and code

Policy information about [availability of computer code](#)

| | |
|-----------------|--|
| Data collection | FACSVerse, FACSFortessa, FACSLyrics, Seahorse XF HS mini, Ion Torrent Proton. Shell and R scripts for variant calling and subsequent mitochondrial DNA mutation calls are available at https://github.com/jlincbio/mito_somatic_mutect2/tree/v0.3 and https://doi.org/10.5281/zenodo.12216418 . |
| Data analysis | FlowJo software(version 10.8.1), GraphPad Prism version 9, Agilent Seahorse analytics(https://www.agilent.com), TMAP (ver 5.12.3), Mutect2 in the Genome Analysis Toolkit (GATK, version 4.1.8), SnpEff (version 5.1d), EAGLE (version 1.1.1), Haplogrep (version 2.4.0), |

For manuscripts utilizing custom algorithms or software that are central to the research but not yet described in published literature, software must be made available to editors and reviewers. We strongly encourage code deposition in a community repository (e.g. GitHub). See the Nature Portfolio [guidelines for submitting code & software](#) for further information.

Data

Policy information about [availability of data](#)

All manuscripts must include a [data availability statement](#). This statement should provide the following information, where applicable:

- Accession codes, unique identifiers, or web links for publicly available datasets
- A description of any restrictions on data availability
- For clinical datasets or third party data, please ensure that the statement adheres to our [policy](#)

The data that support the findings of this study are available from the corresponding authors upon reasonable request. The data of total mitochondrial DNA

sequencing is deposited on JGA (accession number: JGAS000285). We obtained RNA-seq expression data from The Cancer Genome Atlas Program (TCGA) in the Genomic Data Commons (GDC) Data Portal of patients with melanoma from the USCS Xena database (<https://xenabrowser.net>). USP30, USP33, and USP35 gene expression data in tumour tissues were used.

Human research participants

Policy information about [studies involving human research participants and Sex and Gender in Research](#).

Reporting on sex and gender

Patients and samples were collected without regard to specific sex and gender. The number of patients by each gender is summarised in Extended Data Table 1 and Supplementary Data 2.

Population characteristics

Population characteristics is summarised in Extended Data Table 1 and Supplementary Data 2.

Recruitment

In cohort A, patients who underwent surgical resection were recruited prospectively in this study. In cohort B and C, patients were recruited retrospectively in a series of consecutive cases. Cohort A consisted of patients with various cancer types who had undergone surgical resection, whereas cohorts B and C comprised patients with advanced stage melanoma and non-small-cell lung cancer (NSCLC) who had received systemic therapies, respectively. Since patients with NSCLC harbouring driver gene mutations generally receive molecular-targeted therapies prior to other therapies, few such patients were included in the cohort C, which can lead to potential selection bias, limiting the generalisability of the findings to the broader patient population.

Ethics oversight

The protocol for this study was approved by the appropriate institutional review board and ethics committees at Yamanashi University Hospital, Chiba University Hospital, Shinshu University Hospital, Saitama Medical University International Medical Centre, Okayama University Hospital, and Kindai University Hospital. This study was conducted in accordance with the Declaration of Helsinki.

Note that full information on the approval of the study protocol must also be provided in the manuscript.

Field-specific reporting

Please select the one below that is the best fit for your research. If you are not sure, read the appropriate sections before making your selection.

Life sciences

Behavioural & social sciences

Ecological, evolutionary & environmental sciences

For a reference copy of the document with all sections, see nature.com/documents/nr-reporting-summary-flat.pdf

Life sciences study design

All studies must disclose on these points even when the disclosure is negative.

Sample size

The sample size was determined by the availability of feasible samples during the research period. As this was an exploratory analysis, no statistical calculations were conducted. However, preliminary findings indicated that approximately 40% of patients exhibited mitochondrial DNA mutations. On this basis, we deemed the sample size sufficient, as a adequate number of mutated and wild-type cases were collected for analyses.

Data exclusions

No data exclusions were needed

Replication

All experiments were performed in replicates of three or four with similar results.

Randomization

We observed only minor differences in the characteristics between the groups within each cohort, which are unlikely to have a substantial impact on the overall findings. Additionally, given the retrospective nature of the analyses, we determined that it would be difficult to adjust covariates appropriately.

Blinding

All studies involving human samples were exploratory and retrospective , and no blinding was applied during the analyses.

Reporting for specific materials, systems and methods

We require information from authors about some types of materials, experimental systems and methods used in many studies. Here, indicate whether each material, system or method listed is relevant to your study. If you are not sure if a list item applies to your research, read the appropriate section before selecting a response.

Materials & experimental systems

| | |
|-------------------------------------|---|
| n/a | Involved in the study |
| <input type="checkbox"/> | <input checked="" type="checkbox"/> Antibodies |
| <input type="checkbox"/> | <input checked="" type="checkbox"/> Eukaryotic cell lines |
| <input checked="" type="checkbox"/> | <input type="checkbox"/> Palaeontology and archaeology |
| <input type="checkbox"/> | <input checked="" type="checkbox"/> Animals and other organisms |
| <input type="checkbox"/> | <input checked="" type="checkbox"/> Clinical data |
| <input checked="" type="checkbox"/> | <input type="checkbox"/> Dual use research of concern |

Methods

| | |
|-----|---|
| n/a | Involved in the study |
| | <input checked="" type="checkbox"/> <input type="checkbox"/> ChIP-seq |
| | <input type="checkbox"/> <input checked="" type="checkbox"/> Flow cytometry |
| | <input checked="" type="checkbox"/> <input type="checkbox"/> MRI-based neuroimaging |

Antibodies

Antibodies used

Mouse CD3 (clone 17A2, #100218, 1:50), Biolegend
 Mouse CD8 (clone 53-6.7, #550281, 1:50), BD Biosciences
 Mouse CD4 (clone RM4-5, #563933, 1:50), BD Biosciences
 Mouse CD45 (clone 30-F11, #103106, 1:50), Biolegend
 Mouse CD44 (clone IM7, #103012, 1:50), Biolegend
 Mouse CD62L (clone MEL-14, #104408, 1:50), Biolegend
 Mouse CD28 (clone 37.51, #102106, 1:50), Biolegend
 Mouse CD27 (clone 3A10, #124212, 1:50), Biolegend
 Mouse CD127 (clone A7R34, #135014, 1:50), Biolegend
 Mouse/Human KLRG1 (clone 2F1/KLRG1, #138414, 1:50), Biolegend
 Mouse PD-1 (clone 29F.1A12, #135221, 1:50), Biolegend
 Mouse TCF1 (clone S33-966, #564217, 1:50), BD Biosciences
 Mouse TIM3 (clone B8.2C12, #134010, 1:50), Biolegend
 Mouse GranzymeB (clone GB11, #515403, 1:50), Biolegend
 Human CD3 (clone HIT3a, #550367, 1:50), BD Biosciences
 Human CD45 (clone HI100, #304148, 1:50), Biolegend
 Human CD63 (clone H5C6, #353006, 1:50), Biolegend
 Human CD81 (clone 5A6, #349506, 1:50), Biolegend
 Human PD-1 (clone EH12.2H7, #329920, 1:50), Biolegend
 Human CD69 (clone FN50, #562884, 1:50), BD Biosciences
 Human CD27 (clone LG.3A10, #124212, 1:50), Biolegend
 Human CD28 (clone CD28.2, #302906, 1:50), Biolegend
 Human CD45RA (clone HI100, #304122, 1:50), Biolegend
 Human CCR7 (clone 2-L1-A, #566762, 1:50), BD Biosciences
 Human p16 (clone D7C1M, #80772, 1:3200), Cell Signaling
 Human p53 (clone 1C12/12D1 #2015, 1:50), Cell Signaling
 Human USP30(clone B-6, #sc-515235, 1:50), Santa Cruz Biotechnology
 Fixable Viability Dye (Live/dead staining, #L34962, 1:250), Invitrogen
 7-AAD, (#559925, 1:50)BD Biosciences
 Human/mouse ND4 (# 26736-1-AP, 1:1000), Proteintech
 Human/mouse ND5 (#55410-1-A, 1:1000), Proteintech
 Human/mouse ND6 (#NBP2-94464, 1:1000), Novus Biologicals
 Human/mouse ATP6 (# 55313-1-AP, 1:1000), Proteintech
 Human/mouse ND1 (#19703-1-AP, 1:1000), Proteintech
 Human/mouse MT-CO1 (#62101, 1:1000), Cell Signaling Technology
 Human/mouse CYTB (#55090-1-AP, 1:1000), Proteintech
 Human/mouse β-actin (#4970, Clone 13E5, 1:1000), Cell Signaling Technology
 Human CD9 (#20597-1-AP, 1:1000), Proteintech
 Human TSG101 (#67381-1-Ig, 1:5000) Proteintech
 Human Cytochrome C (#4272, Clone D14E12, 1:1000), Cell Signaling Technology
 Bovine serum albumin (#66201-1-Ig, 1:5000), Proteintech

Validation

The manufacturers validated the commercially available antibodies, which were then utilized in accordance with those manufacturers' instructions. The following provides information on the validation of antibodies for flow cytometry and western blotting.

Biolegend antibodies: <https://www.biolegend.com/en-us/quality/quality-control>

- Specificity testing of 1-3 target cell types with either single- or multi-color analysis (including positive and negative cell types).
- Once specificity is confirmed, each new lot must perform with similar intensity to the in-date reference lot. Brightness (MFI) is evaluated from both positive and negative populations.
- Each lot product is validated by QC testing with a series of titration dilutions.

BD Biosciences antibodies: <https://www.bdbiosciences.com/en-eu/products/reagents/flow-cytometry-reagents/research-reagents/quality-and-reproducibility>

The specificity is confirmed by using multiple applications that may include a combination of flow cytometry, immunofluorescence, immunohistochemistry or western blot to test a combination of primary cells, cell lines or transfectant models. All flow cytometry reagents are titrated on the relevant positive or negative cells. To save time and cell samples for researchers, pre-titrated test size reagents are bottled at an optimal concentration, with the best signal-to-noise ratio on relevant models.

Cell signalling antibodies: <https://www.cellsignal.com/about-us/our-approach-process/antibody-validation-flow-cytometry>

Cell signalling products undergo rigorous testing in biologically relevant models, ensuring specificity and an optimal signal-to-noise ratio (S/N) for both conjugated and unconjugated antibodies. Cross-platform validation further confirms antibody specificity. In addition, all antibodies have been tested for optimal dilution, specificity, stability and lot-to-lot reproducibility to ensure they work the first time, every time. Cell signalling tests includes:

- Use of positive and negative cell lines
- Comparison of signal to isotype control to estimate nonspecific binding of primary antibodies
- Treatment with pathway-specific inhibitors/activators
- Treatment with blocking peptides, siRNA, and/or expression vectors
- Phosphatase treatment to confirm phospho-specificity
- Extensive quality control testing to guarantee stability over time and to eliminate lot-to-lot variability
- Optimization of protocols and determination of optimal dilutions
- Validation across multiple applications to confirm antibody specificity

The performance of products is routinely validated across multiple platforms. Comparative analysis in flow cytometry and immunofluorescence confirms that the antibody detects the target specifically. The signal correctly localizes to the nuclear compartment of the cell, although the signal is less robust.

Thermo Fisher Scientific antibodies: <https://www.thermofisher.com/jp/ja/home/life-science/antibodies/invitrogen-antibody-validation.html>

Each antibody is tested by Thermo Fisher Scientific utilizing a variety of techniques, such as SNAP-ChIP Antibody Validation, Immunoprecipitation-Mass Spectrometry Antibody Validation, Knockout and Knockdown Antibody Validation, and Peptide Array Antibody Validation. Each antibody's specific validation procedure is described in the datasheet for that antibody.

Eukaryotic cell lines

Policy information about [cell lines and Sex and Gender in Research](#)

Cell line source(s)

The MC-38 was purchased from Kerafast (Boston, MA), and B16F10 and Jurkat cell and MCF7 and MDAMB-231 cell lines were purchased from ATCC (Manassas, VA), respectively. LLC/A11 and LLC/P29 were established from mouse Lewis Lung carcinoma by Keizo Takenaga.

Authentication

The STR was used for authentication.

Mycoplasma contamination

All cell lines were used after confirming that they were Mycoplasma (-) after Mycoplasma testing with the PCR Mycoplasma Detection Kit (TaKaRa, Shiga, Japan) according to the manufacturer's instructions.

Commonly misidentified lines
(See [ICLAC](#) register)

No commonly misidentified cell lines in the ICLAC database were used.

Animals and other research organisms

Policy information about [studies involving animals; ARRIVE guidelines](#) recommended for reporting animal research, and [Sex and Gender in Research](#)

Laboratory animals

C57BL/6J mice (6-8 weeks old) were purchased from SLC Japan (Shizuoka, Japan). OT-I, PhaMexcised, Cd4cre and Tfamfl/fl mice (Tfam; Mitochondrial transcription factor A) were purchased from The Jackson Laboratory (Bar Harbor, ME, USA). 12 hr on:12 hr off dark/light cycle. Ambient animal room temperature is 23° C, controlled within ±3° and humidity is 50%, controlled within ±5%.

Wild animals

No wild animals were used in the study.

Reporting on sex

Female mice were used in the study.

Field-collected samples

No field-collected samples were used in the study.

Ethics oversight

Mouse experiments were approved by the Animal Committee for Animal Experimentation of Chiba Cancer Center and Okayama University. All experiments met the U.S. Public Health Service Policy on Humane Care and Use of Laboratory Animals.

Note that full information on the approval of the study protocol must also be provided in the manuscript.

Clinical data

Policy information about [clinical studies](#)

All manuscripts should comply with the ICMJE [guidelines for publication of clinical research](#) and a completed [CONSORT checklist](#) must be included with all submissions.

Clinical trial registration

This study is an observational study, not a clinical trial.

Study protocol

No study protocol.

Data collection

Clinical data were collected from medical records.

Outcomes

Progression free survival (PFS) and overall survival (OS) were defined as the time from the initiation of anti-PD-1 mAb until the first observation of disease progression or death from any cause and until death from any cause, respectively.

Flow Cytometry

Plots

Confirm that:

- The axis labels state the marker and fluorochrome used (e.g. CD4-FITC).
- The axis scales are clearly visible. Include numbers along axes only for bottom left plot of group (a 'group' is an analysis of identical markers).
- All plots are contour plots with outliers or pseudocolor plots.
- A numerical value for number of cells or percentage (with statistics) is provided.

Methodology

Sample preparation

To prepare cancer cell lines from patients, surgically resected samples were enzymatically digested with 0.1% collagenase, 0.01% hyaluronidase, and 30 U/mL deoxyribonuclease (Sigma-Aldrich, St. Louis, MO) in RPMI1640 (Thermo Fisher Scientific, Waltham, MA) at room temperature. After filtration and separation according to density gradient, the digested tumour cells were used. 1×10⁷ digested tumour cells were cultured in RPMI1640, containing 10% fetal bovine serum (FBS; Cytiva, Tokyo, Japan), 1% penicillin/streptomycin, and amphotericin B (Thermo Fisher Scientific). Tumour cells were passaged at approximately 80%–90% confluence and used when free of fibroblasts and proliferating beyond the 10th passage. To prepare cultured TILs, tumour digests were initiated in RPMI1640 supplemented with 10% human AB serum, 1% PS, and recombinant human interleukin 2 (rhIL-2: 6000 IU/mL, PепroTech, Cranbury, NJ) in a humidified 37°C incubator with 5% CO₂. Half of the media was aspirated from the wells and replaced with fresh complete medium and rhIL-2 every 2–3 days. To establish LCLs, PBMCs infected with Epstein-Barr virus were cultured in RPMI1640, containing 10% FBS, 0.1 % Cyclosporin-A, and 1% penicillin/streptomycin. PBMCs were obtained by Ficoll/Uropoline gradient centrifugation after blood donation.

Instrument

FACSMelody, FACSFortessa, FACSLyrics and FACSVerse were used.

Software

FACSFortessa, FACSLyrics and FACSVerse were used for data collection, and FlowJo (version 10) was used for analysis.

Cell population abundance

Purity confirmed by FACSMelody was >90% after sorting.

Gating strategy

Cells were gated on physical parameters in FSC-A vs SSC-A, singlets in FSC-H vs FSC-W and SSC-H vs SSC-W. On the singlets, live cells were selected by Fixable Viability Dye negative. And then, CD45+ T cells were selected by CD3 and CD45 positive. CD8+ T cells were selected by CD3 and CD8 positive. On CD8+ T cells, DsRed+ T cells were selected by DsRed positive.

- Tick this box to confirm that a figure exemplifying the gating strategy is provided in the Supplementary Information.